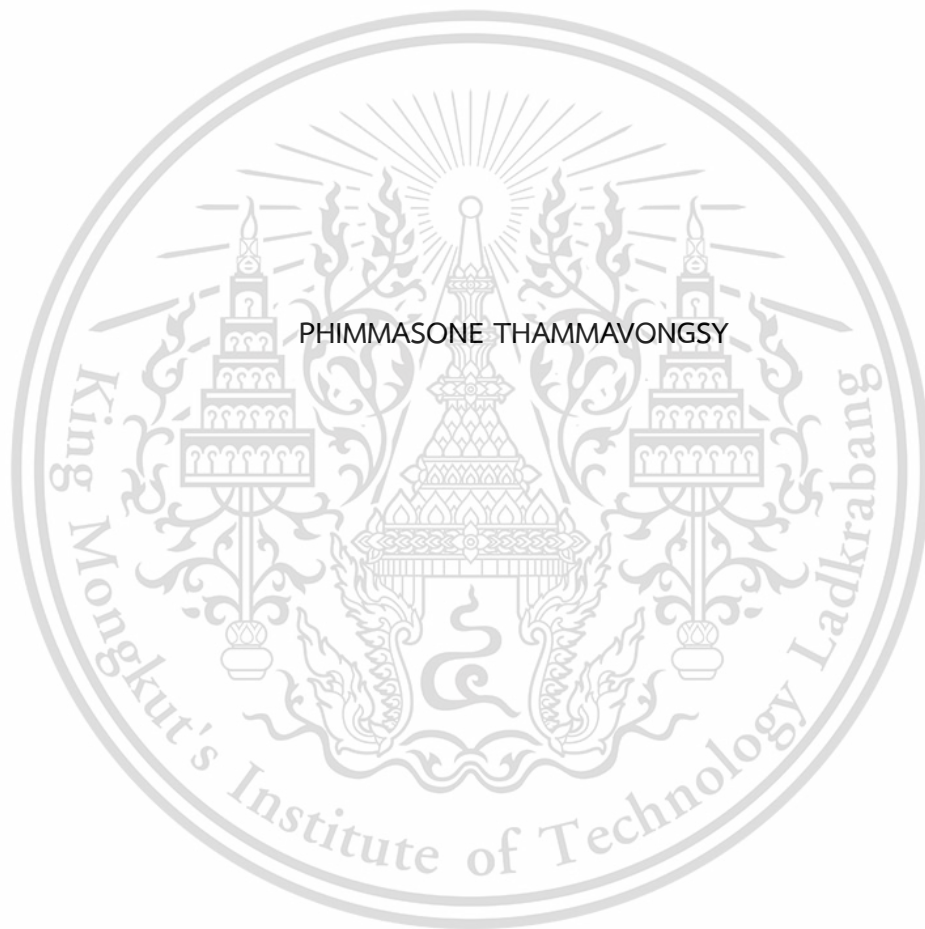


EQUATORIAL SPREAD-F CHARACTERISTICS AND LSTM FORECASTING  
MODEL AT CHUMPHON STATION, THAILAND



A THESIS SUBMITTED IN PARTIAL FULFILLMENT  
OF THE REQUIREMENT FOR THE DEGREE OF  
DOCTOR OF ENGINEERING IN ELECTRICAL ENGINEERING  
SCHOOL OF ENGINEERING  
KING MONGKUT'S INSTITUTE OF TECHNOLOGY LADKRABANG  
2023

KMITL-2023-EN-D- 018-177

This material is reserved for educational use only, not allowed for commercial use.

Forbidden to modify the content, and cite the document when use.



**COPYRIGHT 2023**

**SCHOOL OF ENGINEERING**

**KING MONGKUT'S INSTITUTE OF TECHNOLOGY LADKRABANG**

This material is reserved for educational use only, not allowed for commercial use.

Forbidden to modify the content, and cite the document when use.

หัวข้อวิทยานิพนธ์	คุณลักษณะค่าสเปกตรัมของเส้นศูนย์สูตรและแบบจำลองการพยากรณ์ ชนิด LSTM ที่สถานีชุมพร ประเทศไทย
นักศึกษา	พิมพ์สอน ท่ามะวงสี
รหัสประจำตัว	61601189
ปริญญา	วิศวกรรมศาสตรดุษฎีบัณฑิต
สาขาวิชา	วิศวกรรมไฟฟ้า
พ.ศ.	2566
อาจารย์ที่ปรึกษาวิทยานิพนธ์	ศ. ดร. พรชัย ทรัพย์นิตี

### บทคัดย่อ

การแพร่กระจายชั้นเอฟในเขตเส้นศูนย์สูตร (Equatorial Spread-F: ESF) เป็นหนึ่งในพารามิเตอร์ไอโอโนสเฟียร์ที่สำคัญซึ่งบ่งชี้ความผิดปกติในชั้นกลางของบริเวณชั้นเอฟ.ปรากฏการณ์ ESF สามารถลดประสิทธิภาพของการแพร่กระจายคลื่นวิทยุ เช่น การสื่อสารความถี่สูง (High Frequency: HF) และระบบดาวเทียมนำทางทั่วโลก (Global Navigation Satellite Systems: GNSS) ในวิทยานิพนธ์นี้ ขึ้นแรกเราจะนำเสนอการศึกษาเปรียบเทียบสถิติ ESF ระหว่าง สถานีชุมพร (Chumphon: CPN) ( $10.7^{\circ}\text{N}$ ,  $99.4^{\circ}\text{E}$ ; ละติจูดภูมิศาสตร์แม่เหล็ก:  $3.0^{\circ}\text{N}$ ), ประเทศไทย และ สถานีติรุเนลเวลี (Tirunelveli: TIR) ( $8.73^{\circ}\text{N}$ ,  $77.7^{\circ}\text{E}$ ; ละติจูดธรณีแม่เหล็ก:  $0.32^{\circ}\text{N}$ ), ประเทศอินเดีย ประการที่สอง เรานำเสนอโครงข่ายหน่วยความจำระยะสั้นระยะยาว (Long Short-Term Memory: LSTM) เพื่อพัฒนาแบบจำลองการทำนายของ การเกิดของ ESF ที่สถานี CPN ในการศึกษาเปรียบเทียบ ESF ที่สถานี CPN และ TIR เราใช้ข้อมูล ESF ในเดือนที่เดียวกันในปี 2008 และ 2014 จากระบบไอโอโนซอนด์ที่แตกต่างกันซึ่งประกอบด้วย ไอโอโนซอนด์แบบคลื่นต่อเนื่องแบบปรับความถี่ (Frequency Modulated Continuous Wave: FMCW) ที่สถานี CPN และ ไอโอโนซอนด์ดิจิทัลขั้นสูงของแคนาดา (Canadian Advance Digital Ionosonde: CADI) ที่สถานี TIR คุณลักษณะของ ESF ได้รับการวิเคราะห์เกี่ยวกับการทำงานของการเปลี่ยนแปลงตาม รายวัน ความแปรผันในแต่ละวัน ความแปรผันตามฤดูกาล และการแปรผันรายปีที่สถานี CPN และ TIR คุณลักษณะ ESF จะถูกแสดงโดยใช้เปอร์เซ็นต์การเกิดรายเดือน เปอร์เซ็นต์การเกิดรายวัน การเกิดขึ้นรายวัน ระยะเวลาเกิดขึ้นของ ESF และเวลาเริ่มต้น. สำหรับการพัฒนาระบบจำลองการทำนาย ESF เราใช้ข้อมูล ESF ในเดือน วิษุวัต (Equinoctial months) ตั้งแต่ปี 2551 ถึง 2562 ที่สถานี CPN เท่านั้น. พารามิเตอร์อินพุตของแบบจำลองการคาดการณ์ ESF ได้รับการออกแบบโดยขึ้นอยู่กับ การเปลี่ยนแปลงรายวัน (หมายเลขชั่วโมง) ความแปรผันตามฤดูกาล (หมายเลขวัน) กิจกรรมสุริยะ (หมายเลขจุดดับดวงอาทิตย์ (Sunspot Number: SSN) และ ฟลักซ์แสงอาทิตย์ F10.7 ( $F_{10.7}$  solar flux:  $F_{10.7}$ )) กิจกรรมทางภูมิศาสตร์แม่เหล็ก (ดัชนีแม่เหล็ก ( $A_p/ap_3$  และ  $K_p/kp_3$ )) และสภาวะชั้นเอฟ โดยที่สภาวะชั้นเอฟ ที่นำเสนอใหม่เพื่อปรับปรุงแบบจำลองการทำนาย ESF ได้แก่ ความเร็วการยกตัวของชั้น F (Vertical drift velocity of F layer:  $V_d$ ) และ คลื่นแรงโน้มถ่วงชั้นบรรยากาศ (Atmospheric Gravity Wave: AGW). นอกจากนี้ ผลลัพธ์ของแบบจำลองการคาดการณ์ ESF ยังถูกนำมาเปรียบเทียบกับแบบจำลองไอโอโนสเฟียร์อ้างอิงระหว่างประเทศ (International Reference Ionosphere: IRI) ปี 2016. ประสิทธิภาพของ โมเดล LSTM สามารถบรรลุความแม่นยำมากกว่า 85% ในการทำนายเหตุการณ์ ESF ด้วยพารามิเตอร์  $V_d$  และ AGW แบบจำลอง LSTM สามารถสร้างความแข็งแกร่งได้ต่ำกว่า ANN และ IRI 2016.

<b>Thesis</b>	EQUATORIAL SPREAD-F CHARACTERISTICS AND LSTM FORECASTING MODEL AT CHUMPHON STATION, THAILAND
<b>Student</b>	Mr. Phimmasone Thammavongsy
<b>Student ID.</b>	61601189
<b>Degree</b>	Doctor of Engineering
<b>Program</b>	Electrical Engineering
<b>Year</b>	2023
<b>Thesis Advisor</b>	Prof. Dr. Pornchai Supnithi

## ABSTRACT

The equatorial spread-F (ESF) is a one of the significant ionospheric parameters which indicate irregularities at the bottom part of the ionospheric F region. The ESF phenomena can degrade the performance of radio wave propagations such as high frequency (HF) communication and global navigation satellite systems (GNSS). In this doctoral thesis, we first present the comparative study of the ESF statistics over two longitudinally separated stations between the Chumphon (CPN) station (10.7°N, 99.4°E; geomagnetic latitude: 3.0°N), Thailand and Tirunelveli (TIR) station (8.73°N, 77.7°E; geomagnetic latitude: 0.32°N), India. Secondly, we propose the Long Short-Term Memory (LSTM) network as an ESF prediction model at the CPN station. In the comparative study of the ESF at CPN and TIR stations, we utilize the ESF data in equinoctial months in 2008 and 2014 from two different ionosonde systems: Frequency Modulated Continuous Wave (FMCW) ionosonde at the CPN station and Canadian Advanced Digital Ionosonde (CADI) ionosonde at the TIR station. The ESF characteristics are analyzed regarding the function of diurnal variations, day-to-day variations, seasonal variations, and annual variations at both CPN and TIR stations. The ESF characteristics are exhibited using monthly percentage occurrence, daily percentage occurrence, daily occurrence, existing durations, and onset time. For the ESF prediction model, we use the ESF data in equinoctial months from 2008 to 2019 at the CPN station. The input parameters are diurnal variations (hour number), seasonal variations (day number), solar activity (Sunspot number and F10.7 solar flux), geomagnetic activity (Ap/ap3 and Kp/kp3 indices), and F layer conditions. The new F layer conditions are proposed for improving the ESF prediction model such as vertical drift velocity of the virtual height of F layer (Vd) and atmospheric gravity wave (AGW). From the results, the designed LSTM model can produce lower deviations than the artificial neural network (ANN) and international reference ionosphere (IRI) 2016 models.

## ACKNOWLEDGEMENTS

This doctoral thesis is financially supported by King Mongkut's Institute of Technology Ladkrabang under the doctoral scholarship number KDS2019/016. The door of my long study life has opened under significant supports from the Electronics and Telecommunication Engineering Department, Faculty of Engineering, National University of Laos (NUOL). Importantly, the accomplishments of this doctoral thesis are always assisted by excellent guidance from my supervisor as Prof. Dr. Pornchai Supnithi. He is the main energetic power in driving and pushing me on this meaningful journey of my doctoral study at King Mongkut's Institute of Technology Ladkrabang (KMITL). In addition, I would like to appreciate and thank all teachers at the Electronics and Telecommunication Engineering (NUOL) for giving the trust in myself.

Without questions, there are no answers, questions repeatedly popped up while approaching the finish line of my doctoral study. One of those questions was what I studied for? My best answer is that I intentionally did it for my parents' happiness and the future of my life as my country. These important things were always in my heart all the time. They were called my personal medicines that saved me whenever I was facing darkness and issues. This lesson told me that my life must go on. Therefore, I would like to grant this achievement of mine to the benefactors. Firstly, I would like to give this success as a gift to my parents; without them, I would not exist today. Secondly, this reward would be my pride in being a student under my supervisors. Thirdly, I could not really forget to express gratefulness to my colleagues. Furthermore, I am going to keep contributing all of what I gained from the doctoral study to wherever I am. This is always one of my supervisor's teachings.

I would like to thank the GNSS and Thai Space Weather Information Center, Thailand, for providing research facilities, the SouthEast Asia Low-latitude Ionospheric Network (SEALION) project under administration of the National Institute of Communications Technology (NICT), Japan, for providing the ionogram data and technical support, the World Data Center for Geomagnetism, Kyoto, Japan, for supporting the global magnetic data, and the OMNIWeb Data Explorer under National Aeronautics and Space Administration (NASA), America for contributing the data of solar indices.

Finally, I would like to express my gratitude to all the committees of my doctoral thesis defense for your valuable questions and comments as important jigsaw components that ensure high technical and scientific aspects of this doctoral thesis.

Phimmasone Thammavongsy

## Table of Contents

Chapter 1 Introduction .....	1
1.1 Statement of the problems .....	1
1.2 Objectives .....	2
1.3 Hypothesis .....	2
1.4 Scope of the study .....	3
1.5 Process of the study .....	3
Chapter 2 Literature reviews and background theories .....	5
2.1 Characteristics of the equatorial spread-F (ESF) .....	5
2.1.1 Earth's atmosphere .....	5
2.1.2 Generation and variation of the ESF phenomenon .....	7
2.2 Neural Network Models .....	20
2.2.1 Artificial Neural Network (ANN) .....	21
2.2.2 Recurrent Neural Network (RNN) .....	23
2.2.3 Long Short-Term Memory (LSTM) .....	23
2.2.4 Performance metrics in classification .....	29
2.2.5 Role of AI on ionospheric forecasting models .....	30
Chapter 3 The designed and proposed methods .....	31
3.1 Study of the ESF characteristics at longitudinal stations .....	31
3.1.1 Characterizing the ESF monthly occurrence rate .....	31
3.1.2 ESF onset and duration .....	32
3.2 ESF forecasting models .....	33
3.2.1 Data selection and preparation .....	33
3.2.2 Input design for ESF forecasting models .....	35
3.2.3 Deployment of the ESF models .....	36
Chapter 4 Results and Discussions .....	37
4.1 Comparison of ESF characteristics at CPN and TIR stations .....	38
4.1.1 Day-to-day variability in the ESF occurrences .....	39
4.1.2 Comparison of simultaneous ESF onsets at CPN station and TIR station .....	41
4.1.3 Monthly occurrence rates and durations of the ESF events at CPN and TIR stations .....	43
4.1.4 Comparison of the ESF occurrence rate between observations and IRI 2016 model .....	46
4.2 The performance and results of the ESF forecasting models .....	47
4.2.1 Characteristics of the F layer height, vertical drift velocity, and ESF events .....	48
4.2.2 ESF model performance with different architecture designs .....	52
4.2.3 ESF model performance with input combinations .....	53
4.2.4 Comparison between observations against ANN, LSTM, and IRI 2016 models .....	55

This material is reserved for educational use only, not allowed for commercial use.

Forbidden to modify the content, and cite the document when use.

4.2.5 Prediction results of the ESF daily occurrence rate.....	58
4.2.6 Prediction of the short-time occurrences of the ESF events.....	59
4.2.7 Performance of the ESF model on ahead predictability analysis.....	60
Chapter 5 Conclusions.....	63



## LIST OF FIGURES

Figure 1.1: The degradation of the radio propagation signals caused by the ESF.....	2
Figure 2.1: Earth's atmosphere profiles [14].....	6
Figure 2.2: The webpage of the IRI model [16]. .....	7
Figure 2.3: An example of the plasma density irregularities on RTI maps by the backscatter power at 3m wavelengths measured at Jicamarca, Peru [17].....	8
Figure 2.4: Simulated structure of the EPB/ESF occurrence using the HIRB model [23].....	8
Figure 2.5: The installed FMCW ionosonde at CPN station [24]. .....	9
Figure 2.6: FMCW radar system with frequency and time relations [24]. .....	10
Figure 2.7: Block diagram of the FMCW ionosonde system at CPN station [24]. .....	10
Figure 2.8: The sequence of observed Spread-F at CPN station [24]. .....	11
Figure 2.9: The ionogram image from the FMCW ionosonde. ....	12
Figure 2.10: An example of ionogram traces with ionospheric parameters and their scaling point [25].....	12
Figure 2.11: The ionogram images with and without ESF. (a) Ionogram trace without ESF. (b) Ionogram trace with the frequency-type spread-F (FSF). (c) Ionogram trace with the range-type spread-F (RSF). (d) Ionogram trace with mixed-type spread-F (MSF). (e) Ionogram trace with strong-type spread-F (SSF).....	13
Figure 12: Examples of ionospheric parameters on 4 April, 2013 including (a). Variations of h'F and PRE against ESF and (b) Variations of Vd and ESF. ....	14
Figure 2.13: Plot of Morlet wavelet components including real and imaginary parts in time domain (left). The corresponding wavelets in the frequency domain (right). The scale is defined as $s = 10\delta t$ . .....	16
Figure 2.14: Calculation of the averaged power spectrum of the AGW index through the wavelet analysis. ....	18
Figure 2.15: Analysis of the foF2 signal using the Morlet wavelet transform. The top panel shows the foF2 signal (black line with dot) and Spread-F (blue line) at each time. The middle panel represents the power spectrum of the wavelet analysis with 0.5 – 1.5 hours periodicities. The bottom panel shows the averaged value of the power spectrum of the wavelet analysis during 10:00 to 22:00 UTC. ....	19
Figure 2.16: Distribution of the plasma density depletions on magnetic equator planes at different time resolution [22]. .....	20
Figure 2.17: Statistics of publications in using the AI technology from the web of science publication database: DL, deep learning; CNN, convolutional neural network; DBN, deep belief network; LSTM, long shorth-term memory; AEN, autoencoder; and MLP, multilayer perceptron. [71]. .....	21

Figure 2.18: Demonstration of the Sigmoid and hyperbolic tangent functions. ....	22
Figure 2.19: The ANN network structure and its neuron unit. ....	23
Figure 2.20: The inside LSTM cell structure. ....	24
Figure 2.21: The LSTM network structure with many inputs and single output. ....	25
Figure 2.22: Analysis of the Model performance using confusion matrix. ....	29
Figure 3.1: Geographical locations of CPN and TIR stations. ....	31
Figure 3.2: Geographical map of the TIR and CPN stations on assumption of estimating the ESF events. ....	32
Figure 3.3: Flowchart of the research process. ....	33
Figure 3.4: Diagram of the ESF model by the ANN and LSTM network. ....	36
Figure 4.1: Sunspot number (SSN) of the 24 <sup>th</sup> solar cycle [81]. ....	37
Figure 4.2: The availability of the ionogram data at CPN station. ....	37
Figure 4.3: The amount of available data in each month from 2008 to 2019 at CPN station. ....	38
Figure 4.4: Day-to-day variability of the ESF occurrence in LSA at CPN and TIR stations. ....	40
Figure 4.5: Same as above figure for HSA. ....	41
Figure 4.6: Statistics of the ESF onsets at CPN and TIR stations (TIR+ is meant that an ESF onset occurs at TIR station after at CPN station and TIR- represents otherwise). (a). 2008 and (b). 2014. ....	42
Figure 4.7: The monthly percent statistics and frequency of the ESF occurrences at CPN and TIR stations. (a) 2008 and (b) 2014. ....	45
Figure 4.8: Comparative results of the ESF occurrence rate against with the IRI 2016 model at CPN and TIR stations. (a). 2008 and (b). 2014. ....	47
Figure 4.9: Day-to-day variability in the h'F and ESF occurrence in 2013, 2014, and 2016 at CPN station. ....	49
Figure 4.10: Day-to-day variability in the vertical drift velocity of the h'F and ESF occurrence in 2013, 2014, and 2016 at CPN station. ....	51
Figure 4.11: Results of determining the network architecture for (a) ANN and (b) LSTM. ....	53
Figure 4.12: The performance of the LSTM with different loopbacks. ....	53
Figure 4.13: The ESF models' performance with each input combination for (a) ANN and (b) LSTM. ....	55
Figure 4.14: The best performance of the ANN and LSTM models with the input D and E. respectively. ....	55
Figure 4.15: Comparison of the ESF occurrence percentage between observations, ANN, LSTM, and IRI 2016 model at CPN station. ....	57
Figure 4.16: Comparison of each model against the observed ESF values. ....	57
Figure 4.17: The residual errors between the observations and the ESF models for the daily ESF percentage. ....	59

This material is reserved for educational use only, not allowed for commercial use.

Forbidden to modify the content, and cite the document when use.

Figure 4.18: The performance of the ANN and LSTM models for the ESF daily prediction..... 59

Figure 4.19: The performance of the ANN and LSTM models on the ESF short-time prediction.... 60

Figure 4.20: The performance of the LSTM model on 1h to 24h prediction ahead. .... 61



## LIST OF TABLES

Table 1: Details of FMCW and CADI ionosonde systems.....	9
Table 2: Designs of the input combinations for the ANN and LSTM models.....	35
Table 3: Data portion of the training and testing sets. ....	38
Table 4: The averaged values of Ap and F10.7 indices in each month during 2008 (LSA) and 2014 (HSA).....	38
Table 5: Determination of the solar index as an input of the ESF model. ....	54
Table 6: Determination of the Ap/ap3 and Kp/kp3 indices as an input of the ESF model. ....	54
Table 7: The LSTM model's performance with and without the AGW index. ....	58



## ABBREVIATIONS

ANN	Artificial Neural Network
AI	Artificial Intelligence
Ap	Daily value of Earth's global magnetic activity
Ap3	3 hourly values of Earth's global magnetic activity
AGW	Atmospheric Gravity Wave
BP	Back propagation
DFT	Discrete Fourier Transform
Dn	Day number
Dc	Day number in cosine function
DOY	Day of year
Ds	Day number in sine function
EEJ	Equatorial electrojets
ESF	Equatorial Spread-F
EPB	Equatorial Plasma Bubble
F10.7	solar flux emission with 10.7 cm of the radio wavelength
Fortran	Formula translation
FP	False positive class
FN	False negative class
foF2	Critical frequency of F2 layer
Hn	Hour number
HAS	High solar activity
HIRB	High resolution bubble model
h'F	Virtual height of F layer
HF	High frequency
GD	Gradient Descent
GNSS	Global Navigation Satellite System
GPS	Global Positioning System
Kp	Daily value of Earth's global geomagnetic activity
kp3	3 hourly values of Earth's global geomagnetic activity
LAN	Local area network
LSA	Low solar activity
LSTM	Long Short-Term Memory
LSWS	Large scale wave structure
LF	Low frequency
LT	Local time
MATLAB	Matrix laboratory

This material is reserved for educational use only, not allowed for commercial use.

Forbidden to modify the content, and cite the document when use.

ML	Machine learning
MF	Medium frequency
MSE	Mean square error
MSID	Medium scale ionospheric disturbance
NASA	National Aeronautics and Space Administration
NICT	National Institute of Communications Technology
PRE	Pre-reversal enhancement
$P_t$	Monthly probability
RTI	Range time intensity
R-T	Rayleigh Taylor instability theory
RMSE	Root mean squared error
RNN	Recurrent Neural Network
SEALION	SouthEast Asia Low-latitude Ionospheric Network
$T_s$	Hour number in sine function
$T_c$	Hour number in cosine function
TID	Travelling ionospheric disturbance
TP	True positive class
TN	True negative class
UHF	Ultra high frequency
UT	Universal time
VHF	Very high frequency
Vd	Vertical drift velocity of F layer
SSN	Sunspot Number
S.F.U	Solar flux unit
IRI	International Reference Ionosphere
WAN	Wide area network

## Chapter 1 Introduction

### 1.1 Statement of the problems

The equatorial spread-F (ESF) is an ionospheric factor indicating a natural irregular phenomenon after sunset in the equatorial ionospheric region. The ESF is related to the plasma irregularity at the bottom side of the ionospheric region, which occurs on time scales ranging from seconds to hours and length scales from centimeters to tens of kilometers [1]. The ESF is first detected in the 1930's using the ionosonde at Huancayo, Peru [2]. The diffusion echoes of the ionospheric trace on ionogram image are broadened in altitude over tens of kilometers. Therefore, the ESF is known as ionospheric irregularity. The ionospheric irregularity or depletions of the ionospheric plasma density can be basically described by the instability mechanism through theory of the Rayleigh-Taylor instability [3] and [4]. The initialization of the ionospheric irregularities is often seen after sunset and near the magnetic equatorial areas. In contrast, they can possibly generate after post-midnight during the solstice months. Hence, the ionospheric irregularities can be measured by numerous instruments such as swarm satellite, GNSS satellite, in situ instrument, VHF radar, ionosonde radar, all sky imager, and COSMIC satellites [5], [6], [7], [8] and [9]. The ESF events can affect the performance and reliability of ground based electronic systems, space borne, and radio wave propagation when their signals passed through the ESF region as shown in Figure 1.1. For example, the signal outage of UHF communications during sunset is caused by strong spread-F events, scintillation of the satellite signals by plasma bubbles resulting the reduction of available satellites, and degraded positioning accuracy [10], [11], [12] and [13]. Many researchers have been working to understand physical mechanisms of the ESF events in both local and global aspects. The local ionospheric irregularities are a complicated problem which is not clearly understood. In particular, the day-to-day variability in the ionospheric irregularities cannot be clearly discovered. Furthermore, the study of the longitudinal differences of ESF characteristics on the same latitude is needed. Understanding the ESF events and development of the ESF prediction model is crucial and necessary for warning and prediction capabilities.

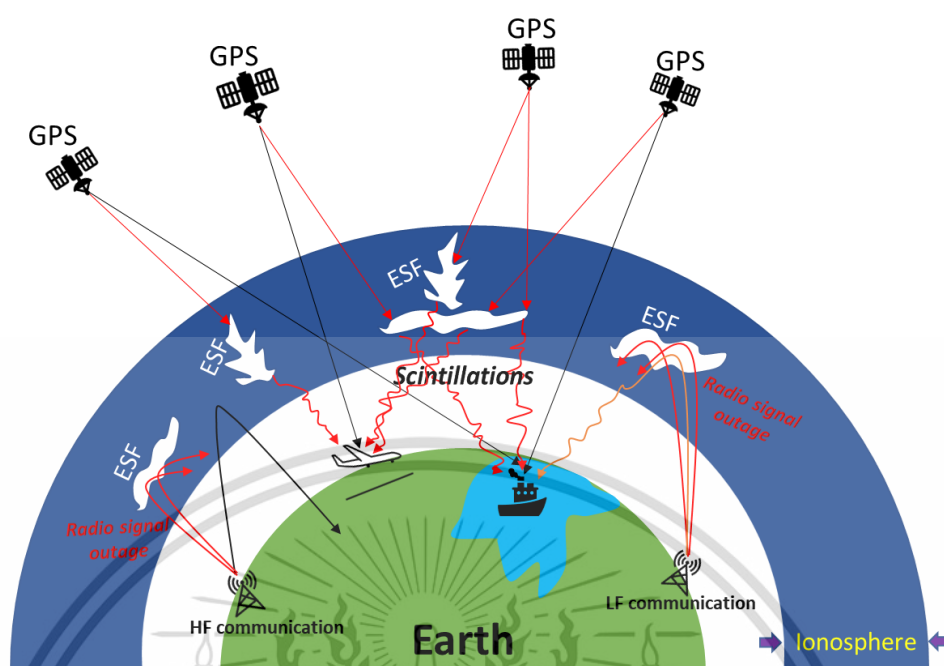


Figure 1.1: The degradation of the radio propagation signals caused by the ESF.

## 1.2 Objectives

In this thesis, there are two main objectives as follows

- To study ESF characteristics over two longitudinal stations at Chumphon station (CPN), Thailand and Tirunelveli (TIR) station, India
- To develop the ESF prediction model at CPN station using the long short-term memory network

## 1.3 Hypothesis

Firstly, this thesis is intended to investigate and understand global and local characteristics over longitudinal CPN and TIR stations in equinoctial months during low and high solar activities. Local dependent conditions of the ESF events are unique and important to clearly understand more about day-to-day variabilities. Therefore, it is very clear expectation in interpreting the longitudinal ESF characteristics through their onset time, durations, day-to-day variations, and monthly occurrence rate. Furthermore, estimates of the ESF onsets at CPN station are supposed to be controlled by the ESF onsets at TIR station. As a result of monthly occurrence rate, the observations are compared to the ESF global model in the International Reference Ionosphere (IRI) model for both CPN and TIR stations. This is an important task in the international arena in reporting and validating the global model.

Secondly, development of the ESF forecasting model by Long Short- Term Memory (LSTM) network is also emphasized only at CPN station. For understanding in the ESF characteristics, This material is reserved for educational use only, not allowed for commercial use.

Forbidden to modify the content, and cite the document when use.

complexities of the ESF developed and developing processes have been widely known depending on both global and local conditions. In this thesis, we determine the predictability scale of the ESF model on diurnal, daily, and monthly variations. In addition, the global conditions of the ESF forecasting model relies on solar and magnetic activities. Importantly, we present a local parameter of the ionospheric F layer conditions as input for the ESF forecasting model. In time series forecasting tasks, the LSTM network can achieve high accuracy based on its Long Short-term recognizability and robustness against vanishing/exploding gradient. Therefore, the purpose of this thesis is clearly seen to fulfill the ESF development at CPN station.

#### 1.4 Scope of the study

The first study of thesis is focused on study of the Equatorial Spread-F (ESF) characteristics over Chumphon (CPN) station, Thailand, and Tirunelveli (TIR) station, India in low and high solar activities. part is interpreted about the longitudinal characteristics of the ESF events and the investigation of the forecasting model with coordinated ESF events over CPN station in Thailand and TIR station in India. Secondly, we develop the forecasting model of the ESF events using Long Short-Term Memory (LSTM) network. The second part discusses the analysis of the ESF characteristics and the development of the ESF forecasting models at CPN station. We utilized the ESF data with 10-minute, 15-minute, and 30-minute interval times in equinoctial months from 2008 to 2019 from the CPN and TIR stations. The ESF forecasting models are designed with capability of predicting the ESF events within 0.5 to 24 hours ahead. The new local input parameters consist of the virtual height of F layer, the vertical drift velocity, and the atmospheric gravity wave. These three parameters are respectively obtained by ionogram manual scaling, differentiation of F layer height with respect to time, and Wavelet transform on the F2 peak frequency. The performance of the ESF forecasting models is evaluated in three dimensions including monthly probability, daily probability, and short-time predictions. In addition, the observed ESF events at TIR station are considered in investigating predictability of the ESF events at CPN station. The commencement, durations, monthly percentage, and day-to-day of the ESF events are studied between the CPN and TIR stations.

#### 1.5 Process of the study

Implementation of research experiments is carried out systematically on processes. We first investigate the understandings in the ESF characteristics leading to our next work. Therefore, the study procedures can be expressed as follows.

- (a) Study of the ESF characteristics between CPN and TIR stations
  - 1) Data selection by considering the solar and season
  - 2) Data preparation to filtering the outlier values, matching days of the data between CPN and TIR stations, and converting the universal time to local time

This material is reserved for educational use only, not allowed for commercial use.

Forbidden to modify the content, and cite the document when use.

- 3) Data processing for finding the monthly occurrence rate, day-to-day occurrence, onset time, and durations
  - 4) Data visualization for comparing the ESF characteristics between these two stations
  - 5) Demonstration of the ESF characteristics
  - 6) Summary of the investigations
- (b) Development of the ESF prediction model at CPN station
- 1) Data selection is based on the solar activity
  - 2) Data cleaning to ignore outlier values and scanty data
  - 3) Data generation for creating the space input parameter, importing the solar and magnetic indices, and calculating the F layer parameters
  - 4) Data formatting to aligning the data sample on time series variations
  - 5) Data pre-processing is used to scale the input signals into given range between 0 and 1 or -1 and 1
  - 6) Design of the structures of the neural network and input features
  - 7) Creation of the neural network model
  - 8) Determination of the hyper-parameters for the created model and training and testing data sets
  - 9) Training and testing of the models
  - 10) Model selection to find the best network structure
  - 11) Retraining and retesting of the best model with new input combinations
  - 12) Model performance analyses
  - 13) Comparison of the final output against the real observed data and the global model

## Chapter 2 Literature reviews and background theories

### 2.1 Characteristics of the equatorial spread-F (ESF)

#### 2.1.1 Earth's atmosphere

The ionospheric physics rises as a discipline of a need to understand the origin and effects of the ionized upper atmosphere on radio wave propagation system. The ionosphere is discovered from radio wave observations that reflect layer composed of electrons and positive ions [14]. This could interpret the characteristics of the data. The structure of Earth's atmosphere can be organized by a temperature profile, while the ionosphere is sensibly organized by the plasma density as shown Figure 2.1. The earth's atmosphere changes in composition and density as the altitude enhances above the surface. The earth's atmosphere can be mainly divided into five layers including Troposphere, Stratosphere, Mesosphere, and Thermosphere as shown in Figure 2.1(left-hand side). The atmospheric temperature initially reduces with altitude from the surface temperature in troposphere layer. The reversion of this temperature trend takes place around 10km altitude at tropopause. The enhancement in the temperature trend is primarily caused by the absorption and ozone as part of the ultraviolet portion of the solar radiation. This effect peaks at 50 km, later, the temperature trend reverses again at stratopause. The beginning of the stratosphere layer is above 10 km. The minimum temperature is measured around 90km in the stratosphere (the mesopause). The temperature increases dramatically at height above the altitude of the minimum temperature due to the absorption of high energy solar protons. This region is called thermosphere. The incremental temperature in the thermosphere can be furthermore explained by absorption of UV and EUV radiation from the sun, namely the EUV radiation is responsible for the production of plasma in the sunlit hemisphere because these solar protons have sufficient energy to ionize the neutral atmosphere. Thus, the positive ions and electrons are produced in this ionization process.

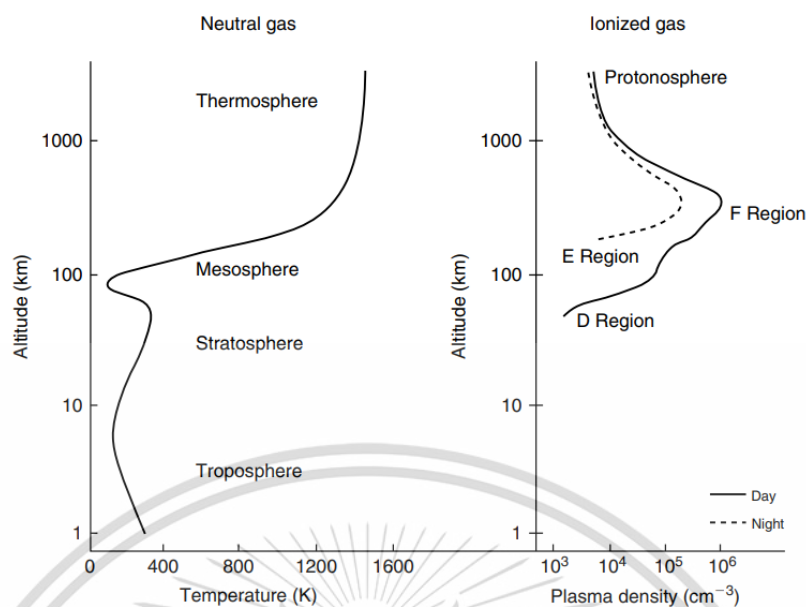


Figure 2.1: Earth's atmosphere profiles [14].

As mentioned above, the ionization process produces two plasma density profiles as daytime midlatitude conditions and nighttime. This is well-known as an ionospheric layer. In daytime, the plasma density profile is composed of D and F regions. The incidence of the solar spectrum on a neutral atmosphere causes exponential increases in density with decreasing altitude. The photoionization process absorbs the photons resulting in the beam reduction in intensity as it penetrates. The maximum plasma density occurs in the F layer (The F region is frequently separated into F1 and F2 regions during daytime due to the role of molecular ions.) and attains high values near noontime. The peak plasma density value is limited by the combination rate at ions and electrons combine to form a neutral molecule or atom. In nighttime, the plasma density profile near the F peak is decreased in magnitude as shown in Figure 2.1 (right-hand side). The appearance of the E region can be seen based on the assumption that plasma is absent between the layers. This is herewith a disappearance of the D region by dropping to levels of  $100\text{-}100\text{ cm}^{-3}$  to all the way to the base of the F region. Thus, the E region is named from electric field in the radio wave reflected by the "Heavyside" layer (the first name for the ionosphere). Importantly, there are many phenomena occur in the ionosphere during the nighttime such as depletions of the plasma density which is well-known as equatorial plasma bubble (EPB) or ESF [15].

The first development of the ESF probability model is initiated using a B-spline method [15] as shown in Eq. 2.1. The ESF probability is obtained depending on function of diurnal variations, month, solar index, and location as  $P(t, m, F, \phi)$ . The ESF probability has been added into the global model as the International Reference Ionosphere (IRI) model since 2003. The IRI model is a standard global model of the earth's atmosphere in producing atmospheric and space data sources based on empirical model (data-based) to users around the world. The most recent model is the IRI model [15]. The ESF probability is one of IRI model parameters, derived on function of time for

This material is reserved for educational use only, not allowed for commercial use.

Forbidden to modify the content, and cite the document when use.

all latitudinal and longitudinal locations [16]. The users can access the ESF probability data in the IRI model using the website service and MATLAB/Fortran compiler. The webpage of the IRI model is shown in Figure 2.2.

$$P(t, m, F, \phi) = \sum_{i=1}^{24} \sum_{j=1}^{12} \sum_{k=1}^3 \sum_{l=1}^2 a_{i,j,k,l} N_{i,4}(t) N_{j,2}(m) N_{k,2}(F) N_{l,2}(\phi) \quad 2.1$$

where  $a_{i,j,k,l}$  represents the monthly means of the ESF occurrence for local time, month, solar flux, and latitude.  $N_{i,4}(t)$  is the basic function of B-spline with order four applied to the local time dependence,  $N_{j,2}(m)N_{k,2}(F)N_{l,2}(\phi)$  are the basic functions with order two applied to month, solar flux, and latitudinal dependence.

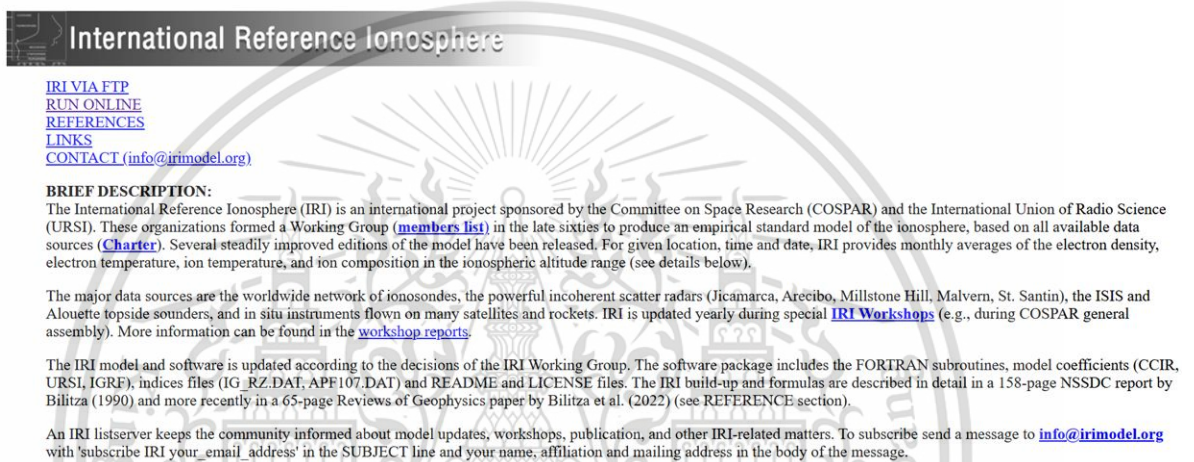


Figure 2.2: The webpage of the IRI model [16].

### 2.1.2 Generation and variation of the ESF phenomenon

The instability in plasma density is a major cause leading to the generation of the ESF phenomena. Some aspects of the investigated results through the vertical drift near the equatorial region can be explained as the highest eastward drift at night is twice as great as the peak westward drift during the day. In addition, the vertical drift is often strongly increased just after sunset but shows no comparable feature near sunrise. This is called the pre-reversal enhancement (PRE) of the vertical drift or of the eastward electric field component [14]. In the early 1970s, the plasma density irregularities can be captured by range-time-intensity (RTI) radar maps [17] as shown in Figure 2.3. The generation of the ESF events is influenced by natural factors such as equatorial electrojet (EEJ),  $E \times B$  drift, upward drift of F layer height, PRE and atmospheric gravity wave [18], [19], [20], and [21]. The instability process in plasmasphere is well known through a Rayleigh-Taylor (R-T) instability [3] and [4]. That is, the EPBs occur in the lower part of the F region after sunset and extend to higher altitudes and latitudes as shown in Figure 2.4. The high resolution 2D simulation of the ESF phenomenon is demonstrated using the High-Resolution Bubble (HIRB) model [22] and [23].

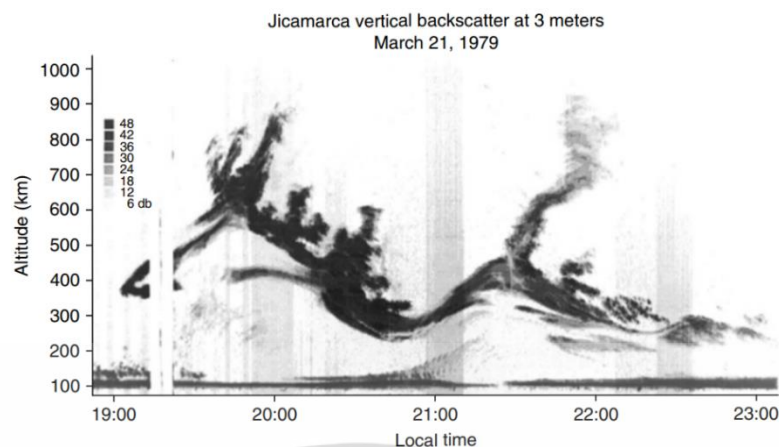


Figure 2.3: An example of the plasma density irregularities on RTI maps by the backscatter power at 3m wavelengths measured at Jicamarca, Peru [17].

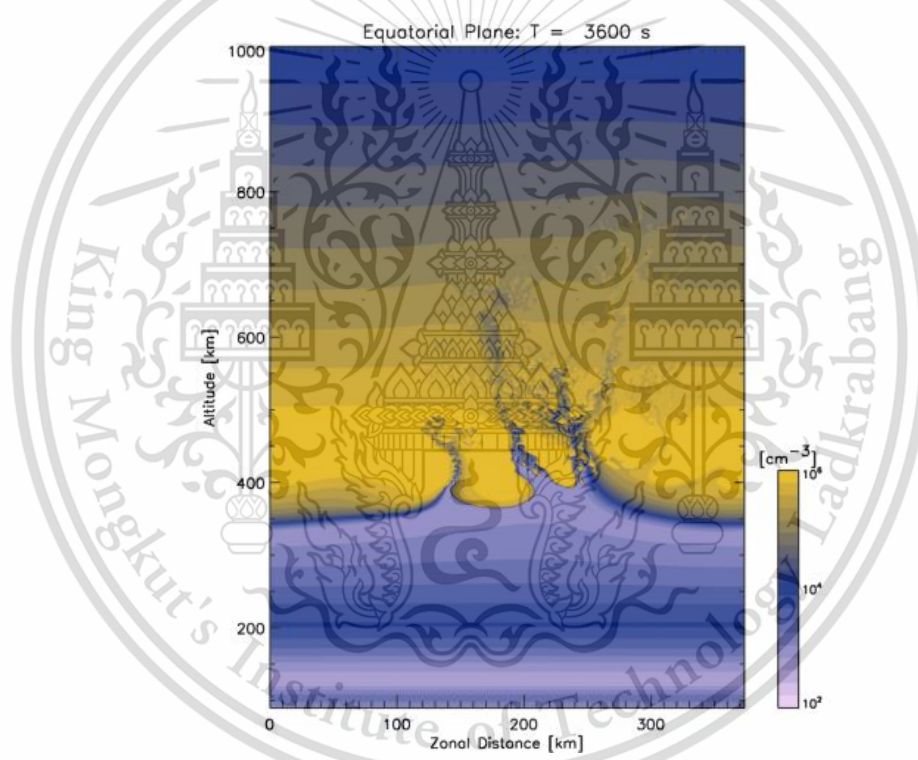


Figure 2.4: Simulated structure of the EPB/ESF occurrence using the HIRB model [23].

### 2.1.2.1 Ionospheric monitoring by an FMCW ionosonde

The principle of both FMCW and CADI ionosondes works in the same way as the radar system. The FMCW system is operated on the analog system, while the CADI system is based on the digital system as shown in Table 1. The operational frequency ranges of the FMCW ionosonde are in the Medium Frequency (MF) – High Frequency (HF) band. The FMCW ionosonde provides a distinctive characteristic utility in bi-static observation by the sufficient locations of the transmitting and receiving antennas installed apart from each other as shown in Figure 2.7. The FMCW ionosonde observation is controlled with linearly varying frequencies (2MHz – 30 MHz by sweep). This material is reserved for educational use only, not allowed for commercial use.

Forbidden to modify the content, and cite the document when use.

rate at 100kHz/s) and time on a moving target. The FMCW antenna and system at CPN station are depicted in Figure 2.5. As shown in Figure 2.8, the observation of the FMCW ionosonde shows the sequence of ionogram images with spread-F phenomena which is drawn every 20 minutes for 3MHz – 9MHz. It is clearly seen that the uplift of F region due to the E x B drift after sunset and developed into the spread-F near the apex.

**Table 1:** Details of FMCW and CADI ionosonde systems.

	Specifications	
	FMCW ionosonde (CPN station)	CADI (TIR station)
Observation mode	Linear FMCW/FMICW	-
Frequency Range	2 MHz ~ 30 MHz	1 MHz – 20 MHz
Transmitting Power	20 W (peak)	600 W
Frequency Sweep Rate	100, 200, 500 kHz/s	100, 200, 400 linear or logarithmic steps
Transmit/receive switching channel	Square wave/M-sequence pseudorandom code	DDS-based synthesiser



**Figure 2.5:** The FMCW ionosonde at CPN station [24].

As shown in Figure 2.6, the frequency and time relation are performed against transmitted and received signals. The different frequency  $f_b$  is derived between the transmitting and receiving signals under range of each moving target  $r$  and line of sight velocity  $v$  as Eq. 2.2. The FMCW is a part of the spread spectrum methods. The frequency scan width  $F$  and the sampling duration  $\tau$  are major parameters of the pulse compression ratio  $G$  in increasing the signal amplitude after pass through the match filter.

This material is reserved for educational use only, not allowed for commercial use.

Forbidden to modify the content, and cite the document when use.

$$f_b(r, v) = \frac{2}{c} (r \cdot \dot{f} - v \cdot f_0) \quad 2.2$$

$$r = r_0 + v \cdot t \quad 2.3$$

$$G = F \cdot \tau \quad 2.4$$

where  $c$  is velocity of light,  $\dot{f}$  and  $f_0$  are frequency sweep rate ( $100 \text{ kHz/s}$ ) and initial frequency, respectively. The two terms in parenthesis of Eq. 2.2 denote the frequency shift due to the range and the doppler shift. This equation is under condition of  $v \ll c$ . The reflected time by a moving target is represented by  $t$ . The initial range at moving target is denoted by  $r_0$ .

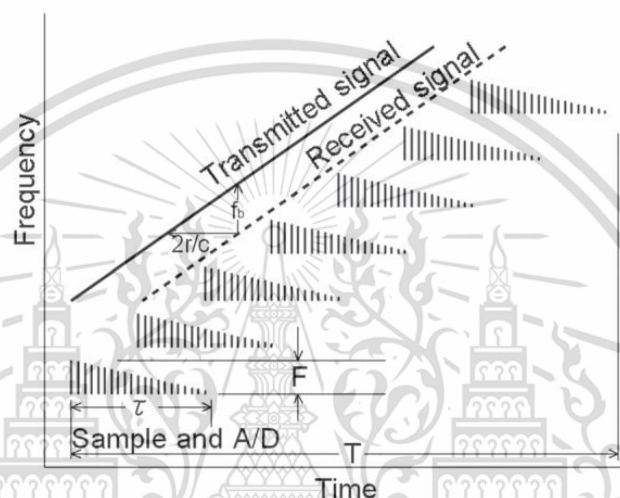


Figure 2.6: FMCW radar system with frequency and time relations [24].

As shown in Figure 2.7, the block diagram of the FMCW ionosonde installed at CPN station. The observation system is composed of a main FMCW ionosonde and peripherals as a pair of transmit/receive antennas, an antenna switch/attenuator, an RW wattmeter, coaxial arresters, a control PC, a network PC, LAN/WAN network, and others.

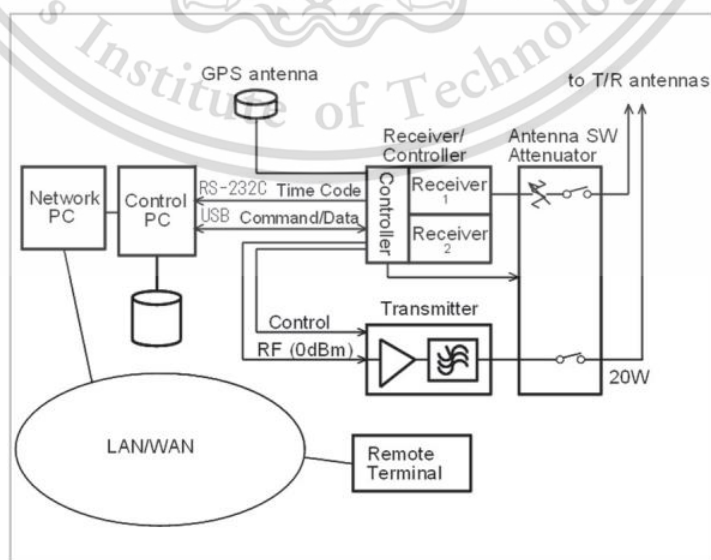
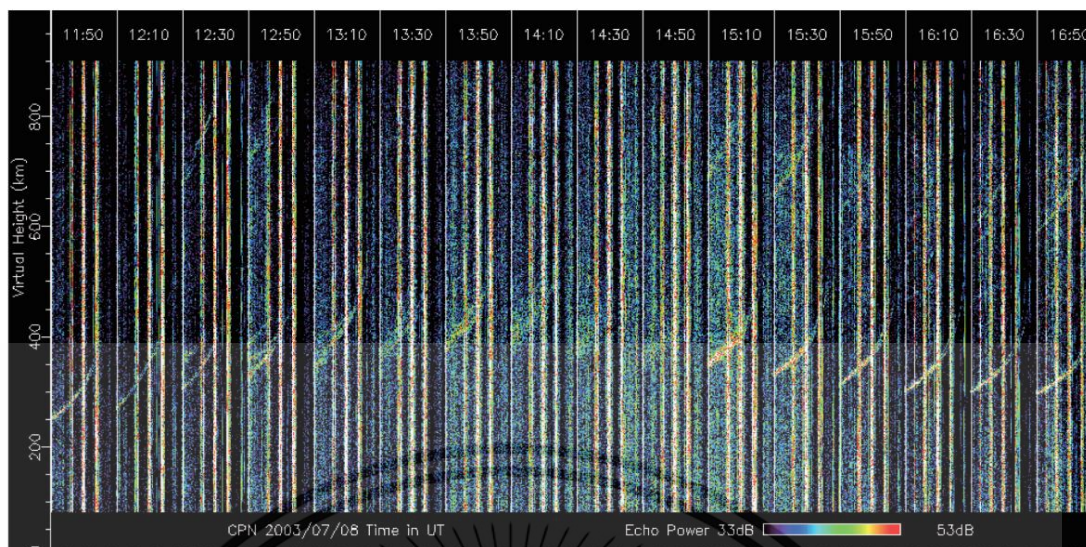


Figure 2.7: Block diagram of the FMCW ionosonde system at CPN station [24].

This material is reserved for educational use only, not allowed for commercial use.

Forbidden to modify the content, and cite the document when use.



**Figure 2.8:** The sequence of observed Spread-F at CPN station [24].

One significance is the principles of the FWCW ionosondes is a manual scale of ionospheric parameters. The ionogram image is a major data obtained from the FMCW ionosonde as shown in Figure 2.9. Thus, the ionospheric parameters can be manually obtained by scaling the ionogram image using the special software. How to do an ionogram scaling is detailed in the manual of ionogram scaling [25]. As shown in Figure 2.10, the example of the ionogram trace with some ionospheric parameters and their scaling points. For examples, the value of the critical frequency of F2 layer ( $f_oF_2$ ) can be derived on at a point on top of the ordinary trace of the ionogram, and the values of virtual height of F layer ( $h'F$ ) is obtained at a point at bottom of the ordinary ionogram trace. Importantly, these  $f_oF_2$  and  $h'F$  parameters are used to compute the power spectrum of atmospheric gravity waves and the upward drift velocity in F layer height as explained in the next two sections. Furthermore, scaled values of the ESF parameter are different from appeared parameters. The ESF is a special type so-called a Type-F parameter in the ionogram scaling. The values of the ESF consist of three types as frequency-type spread-F (FSF), range-type spread-F (RSF), mixed-type spread-F (MSF), and strong-type spread-F (SSF) as shown in Figure 2.11 [26]. Note the correct scaling of all parameters must be carefully considered under given technical conditions in the manual guidebook [25].

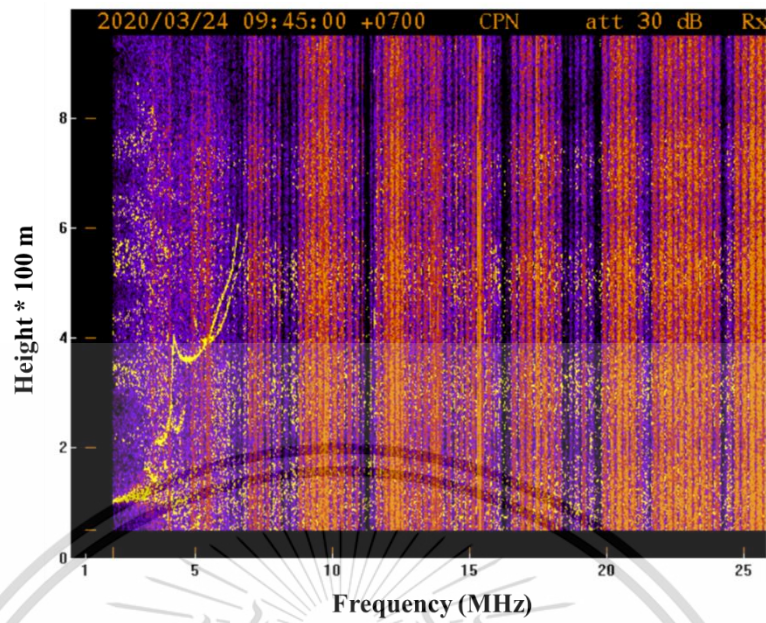


Figure 2.9: The ionogram image from the FMCW ionosonde.

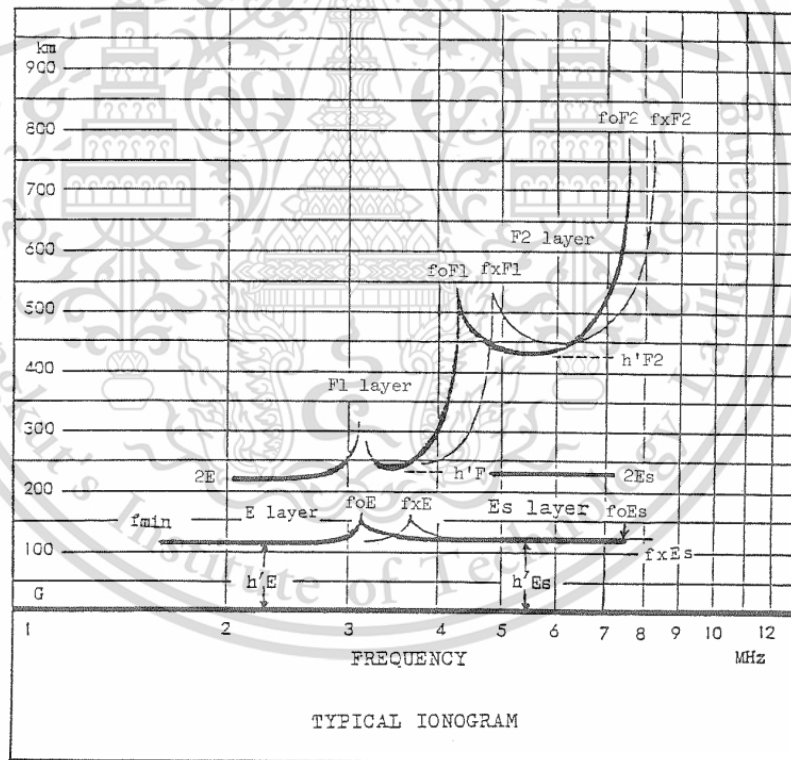
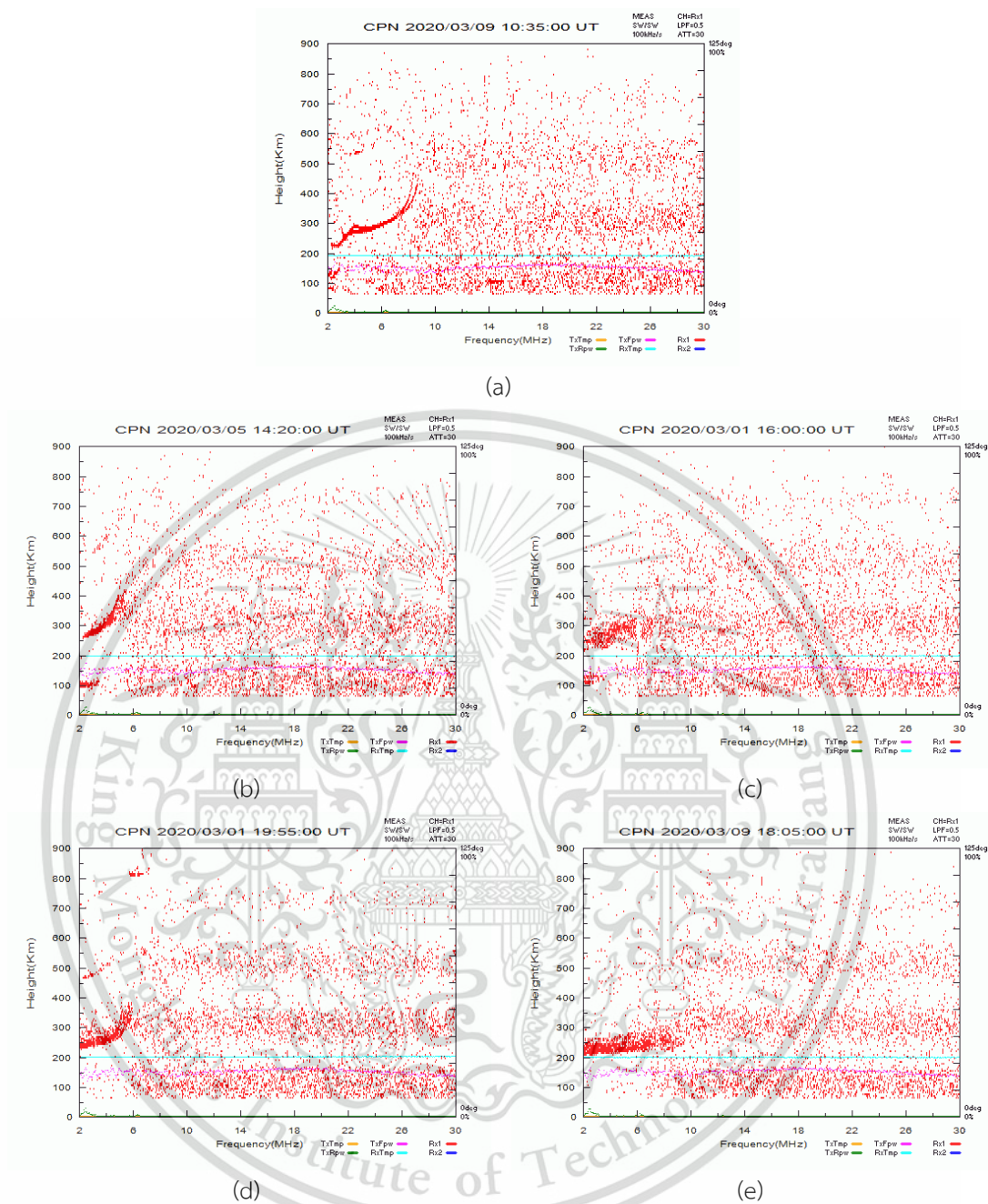


Figure 2.10: An example of ionogram traces with ionospheric parameters and their scaling point [25].



**Figure 2.11:** Types of ionogram images including (a) lonogram trace without ESF, (b) lonogram trace with the frequency-type spread-F (FSF), (c) lonogram trace with the range-type spread-F (RSF). (d) lonogram trace with mixed-type spread-F (MSF), and (e) lonogram trace with strong-type spread-F (SSF).

### 2.1.2.2 Upward drift velocity of the F layer height ( $V_d$ )

Numerous reports have shown that the generation of the ESF can be significantly influenced by both atmospheric gravity waves (GW), pre-reversal enhancement (PRE), and upward drift velocity ( $V_d$ ) [27], [28]. These two precursors are also the important components in the R-T instability function, which play an important role in development and generation of the ionospheric

This material is reserved for educational use only, not allowed for commercial use.

Forbidden to modify the content, and cite the document when use.

plasma irregularities leading to the equatorial plasma bubble (EPB). The EPB is known to be related to the ESF, particularly, the range type of the ESF [15]. In Southeast Asia, [27] presents that the initial phase of the ESF is influenced by the magnitude of PRE and peak values of the h'F resulting in the latitudinal extension of the ESF. The ESF generation is controlled by increased height of the equatorial F layer due to the PRE of the post-sunset vertical plasma drift [29]. Some evidence is shown that the maximum vertical drift velocity and the post-sunset base height of the F-layer influence the time of commencement of the ESF [30]. Thus, the F layer height changes are significantly considered in this study. In particular, the upward drift velocity of the F layer bottom side ( $V_{drift}$  or  $Vd$ ) is obtained by differentiating the h'F with respect to time as shown in Eq. 2.5. This precursor is one of the important post-sunset behavior indications for the ESF events as shown in Figure 12. The figures show that the rise of the h'F variations and its drift velocity is above 20 m/s influence the generation of the ESF.

$$V_{drift} = \frac{\Delta h'F}{\Delta t} \quad 2.5$$

where  $\Delta h'F$  and  $\Delta t$  represents the change of the h'F and time, respectively [27].

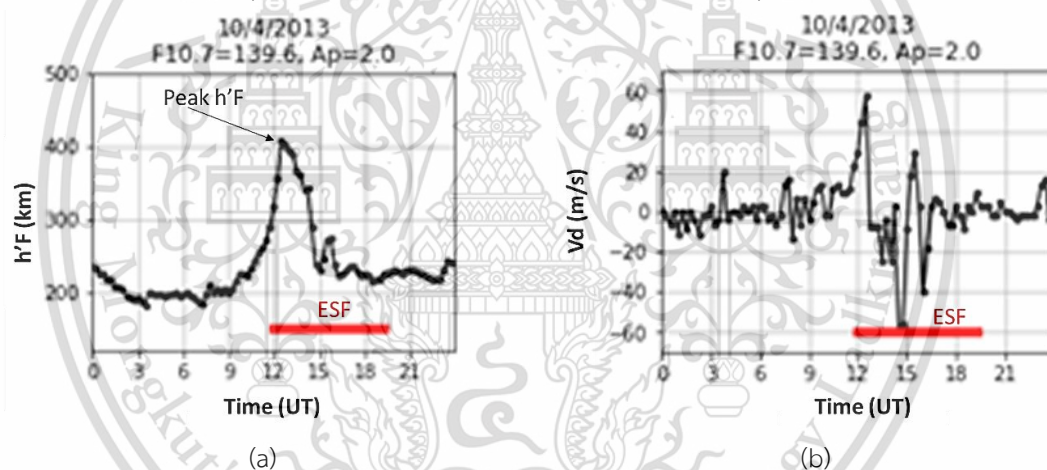


Figure 12: Examples of ionospheric parameters on 4 April, 2013 including (a). Variations of h'F and PRE against ESF and (b) Variations of Vd and ESF.

### 2.1.2.3 Atmospheric gravity wave (AGW) obtained through the wavelet analysis on the foF2 signals

One of the important causes of the ESF generation after midnight is the gravity waves. It is one factor of the R-T instability [3]. Variety of investigations show that the GW is an important source for the ESF generation and development [18], [31], [7], [28], [19]. Characteristics of the gravity waves can be represented in the temporal variations in the h'F [19], [32]. The ESF development is led by the height oscillations of the daytime bottom-side F-layer which are amplified towards post-sunset hours. [33] and [20] show that zonal scale sizes of the wave structures can be estimated from ~1 hour of their period range. The large-scale wave structures are reported with the order of 400 km. This is a spatially propagating gravity wave which gives rise to temporal fluctuations in the

This material is reserved for educational use only, not allowed for commercial use.

Forbidden to modify the content, and cite the document when use.

ionosphere. In previous studies, they indicate that the range of 30 minute to 1.5 hours can exhibit the presence of the gravity waves through temporal fluctuations in different ionospheric parameters both in E and F regions of ionosphere [34], [19], [32]. The gravity wave origin of the fluctuations has been proven by upward amplitude propagation and downward phase propagation characteristics. The 400km of the zonal wavelength is assumed and for detected ionospheric temporal fluctuations with periodicities of 30-60 minutes, the phase speeds are of the order of 100 – 200 m/s.

The existence of the atmospheric gravity waves is revealed by several detection methods based on 30 – 90 minutes periodicity [28]. In this work, the atmospheric gravity waves are represented by analyzing power spectrum of the Wavelet transformation on the foF2 signal [28] and [35]. Wavelet analysis is one of the most signal processing methods. The Wavelet analysis is used to analyze the localized variations of power within time series. Wavelet transformation can simultaneously decompose the time series signal in both frequency and time space, whereas the fast Fourier transformation can only determine the frequency components over the time series signal. The wavelet transform has been utilized for several studies in earth space and geophysics including atmospheric gravity waves [28], dispersion of ocean waves [36], and central England temperature [37]. Basically, the wavelet analysis is theoretically invented in 1992 [38]. The wavelet analysis is developed and consisted of numerous types such as Morlet wavelet, Paul wavelet, and Mexican hat. In this work, the main significant information of the wavelet analysis is based on the guidance of [35]. The Windowed Fourier transform (WFT) is used to extract the local-frequency information from a signal. The Fourier transform is performed on a sliding segment of length  $T$  from a time series of time step  $dt$  and total length  $N\delta t$ . The WFT provides an inaccurate and inefficient method of time frequency localization, as it imposes a scale or “response interval”  $T$  into the analysis [39]. The aliasing of high- and low-frequency components causes the raised inaccuracy, which those frequency components do not fall within the frequency range of the window. Therefore, several window lengths must be analyzed to determine the frequency choice. A method of time-frequency localization is scale independent as wavelet analysis should be employed.

The wavelet transform is used to analyze time series  $x_n$  that contain nonstationary power at many different frequencies, where  $n = 0, 1, \dots, N - 1$ . The time series has time interval space as  $\delta t$ . The wavelet function is performed by  $\Psi_0(\beta)$ , where  $\beta$  is a nondimensional “time” parameter. To gain “admissibility” in a wavelet, this function must have zero mean and be localized in both time and frequency space. The Morlet wavelet is expressed by a plane wave moderated by a Gaussian as the following.

$$\Psi_0(\beta) = \pi^{-1/4} e^{i\omega_0\beta} e^{-\beta^2/2} \quad 2.6$$

where  $\omega_0$  represents the nondimensional frequency, it is set to 6 for satisfying the admissibility condition [40].

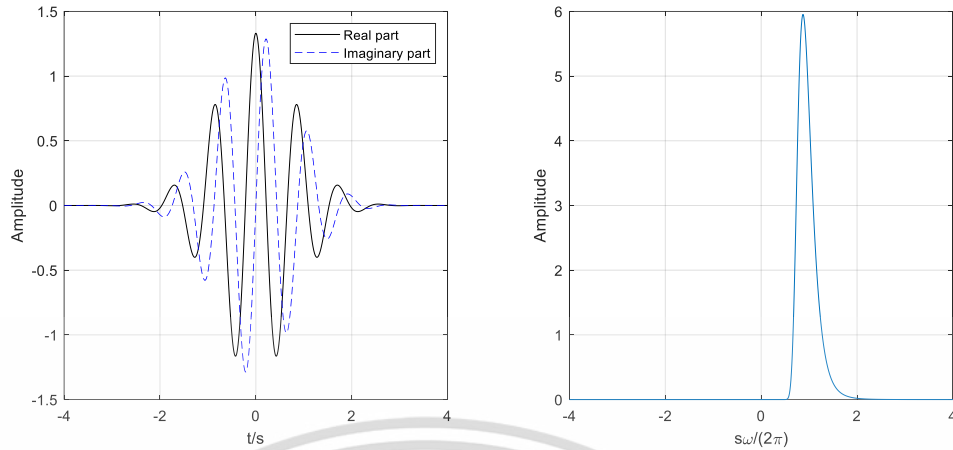


**Figure 2.13:** Plot of Morlet wavelet components including real and imaginary parts in time domain (left). The corresponding wavelets in the frequency domain (right). The scale is defined as

$$s = 10\delta t.$$

The wavelet function terms are generally referred to either orthogonal or nonorthogonal wavelets. The nonorthogonal wavelet function can work with either the discrete or the continuous wavelet transform [40]. Only continuous transform is used. The continuous wavelet transformation of the discrete sequence  $x_n$  can be defined by the convolution of  $x_n$  with a scale and translated version of  $\Psi_0(\beta)$  as the following equation.

$$W_n(s) = \sum_{n'=0}^{N-1} x_{n'} \Psi^* \left[ \frac{(n' - n)\delta t}{s} \right] \quad 2.7$$

where the asterisk (\*) denotes the complex conjugate. We can construct a picture showing both the amplitude of any features versus the scale and how this amplitude varies with time by varying the wavelet scale ( $s$ ) and translating along the localized time index  $n$ . Notice that  $\Psi$  is normalized causing the subscript 0 is disappeared. Approximation of the continuous wavelet transform is done  $N$  times for each scale. To speed up the wavelet transformation, the calculations in Fourier space are considered instead of Eq. 2.8. We can do all  $N$  convolutions simultaneously in Fourier space using a discrete Fourier transform (DFT). The DFT of  $x_n$  is computed as

$$\hat{x}_k = \frac{1}{N} \sum_{n=0}^{N-1} x_n e^{-2\pi i k n / N} \quad 2.8$$

where  $k$  is the frequency index ( $k = 0, 1, \dots, N - 1$ ). In the continuous limit, the Fourier transform of a function is given by  $\hat{\Psi}(s\omega)$ . The wavelet transform is the inverse Fourier transform of the product based on the convolutional theorem.

$$W_n(s) = \sum_{k=0}^{N-1} \hat{x}_k \hat{\Psi}^*(s\omega_k) e^{i\omega_k n \delta t} \quad 2.9$$

where  $\omega_k$  represents the angular frequency which is defined as

$$\omega_k = \begin{cases} \frac{2\pi k}{N\delta t}, & k \leq \frac{N}{2} \\ -\frac{2\pi k}{N\delta t}, & k > \frac{N}{2} \end{cases} \quad 2.10$$

Choice of scales is necessary after choosing the wavelet function for the wavelet transform. For nonorthogonal wavelet analysis, the arbitrary set of scales is used to build up a more complete picture. It is convenient to write the scales as fractional power of two as the following.

$$s_j = s_0 2^{j\delta j}, j = 0, 1, \dots, J \quad 2.11$$

$$J = \delta j^{-1} \log_2 \left( \frac{N\delta t}{s_0} \right) \quad 2.12$$

where  $s_0$  is the smallest resolvable scale and  $J$  is the largest scale. The value of  $s_0$  should be defined so that the equivalent Fourier period is approximately  $2\delta t$ . The relationship of the equivalent Fourier period and the wavelet scale is derived by substituting a cosine wave of a known frequency into Eq. 2.14 and computing the scale  $s$  at which the wavelet power spectrum reaches its maximum. For the Morlet wavelet, the wavelet scale is almost equal to the Fourier period with  $\omega_0 = 6$ , this gives a value of  $\lambda = 1.03s$ , where  $\lambda$  is the Fourier period.

We can calculate the continuous wavelet transform using Eq. 2.9 and a standard Fourier transform routine (for a given scale  $s$ ) at all  $n$  simultaneously and efficiently. Moreover, the wavelet function at each scale  $s$  is normalized to have unit energy for ensuring the wavelet transforms at each scale are directly comparable to each other and to the transforms of other time series.

$$\hat{\Psi}(s, \omega_k) = \left( \frac{2\pi s}{\delta t} \right)^{1/2} \hat{\Psi}_0(s, \omega_k) \quad 2.13$$

where  $\hat{\Psi}_0(s, \omega_k)$  is the unscaled wavelet function.

$$\hat{\Psi}_0(s, \omega_k) = \pi^{-1/4} H(\omega_k) e^{-(s\omega_k - \omega_0)^2/2} \quad 2.14$$

where  $H(\omega_k)$  is Heaviside step function.

$$H(\omega_k) = \begin{cases} 1, & \text{if } \omega > 0 \\ 0, & \text{otherwise} \end{cases} \quad 2.15$$

Wavelet power spectrum can be defined as  $|W_n(s)|^2$ . Thereby, the wavelet function  $\Psi(\beta)$  is generally in complex number, also, the wavelet transform  $W_n(s)$  is in complex number as well. Thus, the transform can be divided into real part  $\Re\{W_n(s)\}$ , and imaginary part  $\Im\{W_n(s)\}$ , or amplitude  $|W_n(s)|$ , and phase  $\tan^{-1}[\Im\{W_n(s)\}/\Re\{W_n(s)\}]$ .

To detect the power spectrum of the atmospheric gravity waves, the observable periodicities of the AGW are about 30 minutes to 60 minutes [28] and [41]. Thus, the periodicities are determined by the Fourier wavelength as the following.

$$\lambda = \frac{4\pi s}{\omega_0 + \sqrt{2 + \omega_0^2}} \quad 2.16$$

The Fourier transform deals with the finite-length time series, thereby errors will occur at the beginning and end of the wavelet power spectrum. One solution is to pad the end of the time series with zeroes before doing the wavelet transform and then remove them afterward. The time

series is padded with sufficient zeros to bring the total length  $N$  up to the next-higher power of two. This limits the edge effects and speeds up the Fourier transformation.

In short, the steps involved in using the wavelet analysis are demonstrated in the following flowchart.

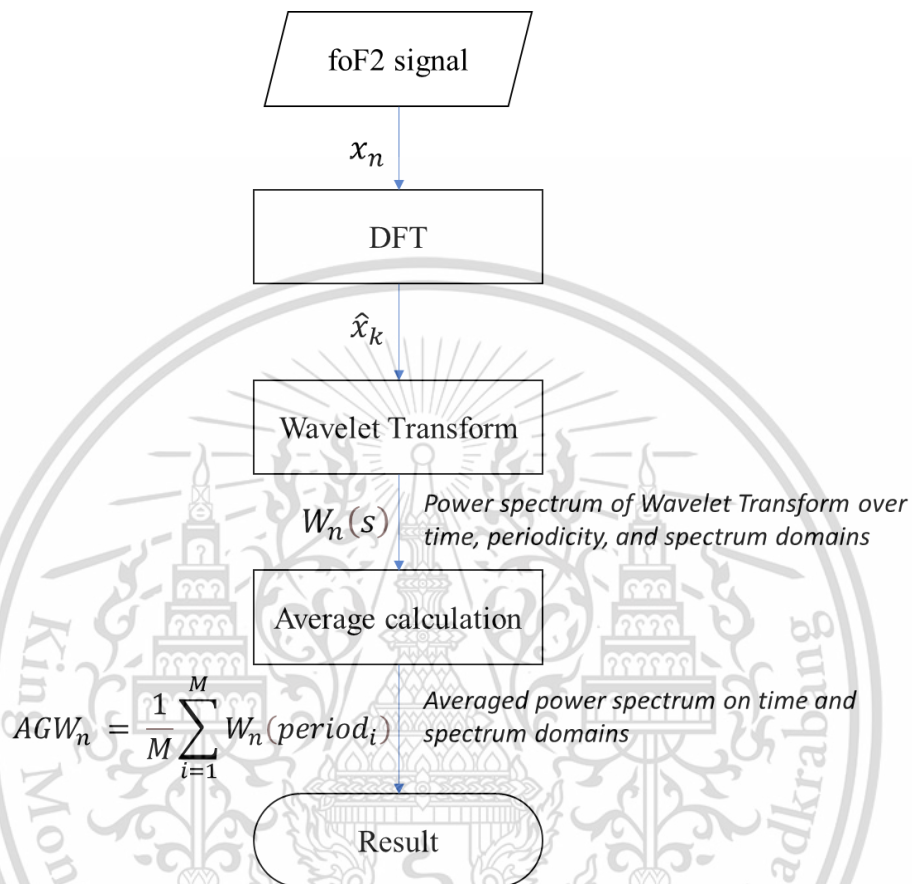
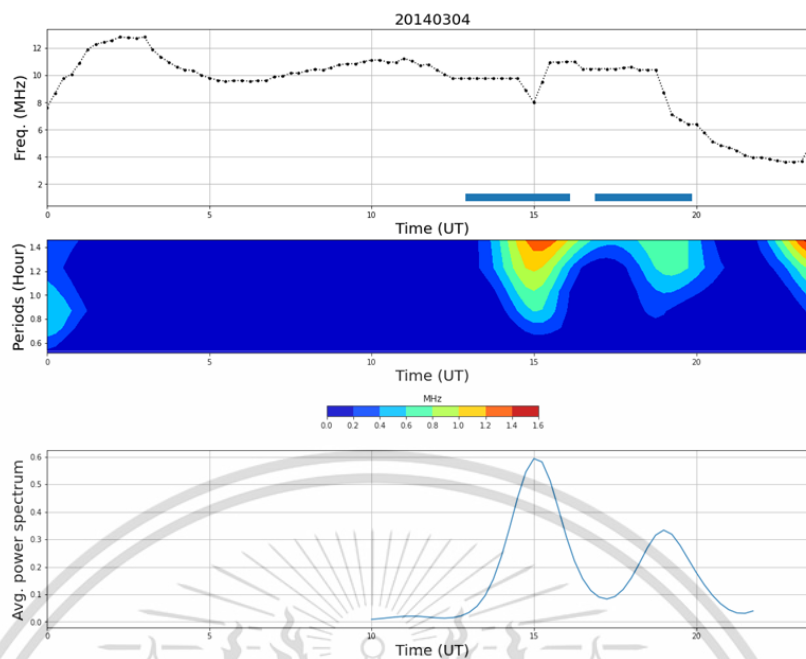


Figure 2.14: Calculation of the averaged power spectrum of the AGW index through the wavelet analysis.

An example of analyzing the foF2 signal using the wavelet transform is shown in Figure 2.15. It shows the foF2 signal and Spread-F against UTC time on the top panel. The power spectrum of the wavelet analysis is shown on the middle panel against UTC time. The averaged power spectrum is shown on the bottom panel. The averaged power spectrum is used as one of the input parameters for the ESF forecasting model.



**Figure 2.15:** Analysis of the foF2 signal using the Morlet wavelet transform. The top panel shows the foF2 signal (black line with dot) and Spread-F (blue line) at each time. The middle panel represents the power spectrum of the wavelet analysis with 0.5 – 1.5 hours periodicities. The bottom panel shows the averaged value of the power spectrum of the wavelet analysis during 10:00 to 22:00 UTC.

#### 2.1.2.4 The variability of ESF occurrences

There are many efforts in describing the ESF variations for both physical development and function of global influencing factors. One of the most recent simulations is of [22] in exhibiting the ESF generation and developed on function on time, latitude and longitude as shown in Figure 2.16. The reproduction of the simulated ESF is seen with east-west asymmetry and tilted structures when multiple seeding components and an eastward neutral wind are applied [23]. On the other hand, characteristics of the ESF occurrences can also be explained on the function of diurnal variations, seasonal variations, and annual variations. The quantity of the ESF occurrence rate are found to increase with the solar activity levels [41], [42], [43], [44]. Study of [42] show that the occurrence of the ESF events at the equatorial CPN station is observed higher than at the Chiangmai (CMU) station (18.76°N, 98.93°E, geomagnetic latitude: 12.7°N), Thailand and the Kototabang (KTB) stations (0.2°S, 100.32°E, dip -10.1°), Indonesia. Conversely, some case studies found that the ESF occurrence is anti-correlated to the solar activity [45] and [46]. The increased magnetic activity is observed to suppress the ESF occurrence [47] and [48]. The ESF occurrence can be observed during the geomagnetic disturbance [45] and [49]. Moreover, the variations of the ESF occurrence are different along latitudes and longitudes. Some evidential investigations are reported with distinctive characteristics of the ESF occurrence in Brazil, Argentina, Vietnam, and American sectors [50], [51].

[52], and [53]. The peak occurrence rate and longest persistence of the ESF events are often observed at stations close to the geomagnetic equator. In equatorial regions, the ESF occurrence in Southeast Asia is lower than in Brazil and American sectors. Along latitudinal variations, the ESF occurrence can be observed in both northern and southern hemispheres, that is, the shifting of the ESF events is supported by magnetic forces which are known as fountain effects. The northward movement of the ESF events is observed in study of [54], which is exhibited and explained in changes of the F layer bottom side altitude. It is realized that the variability of the ESF occurrences can be possibly global and local conditions. The local conditions are the significant key for gaining more understanding in the ESF events.

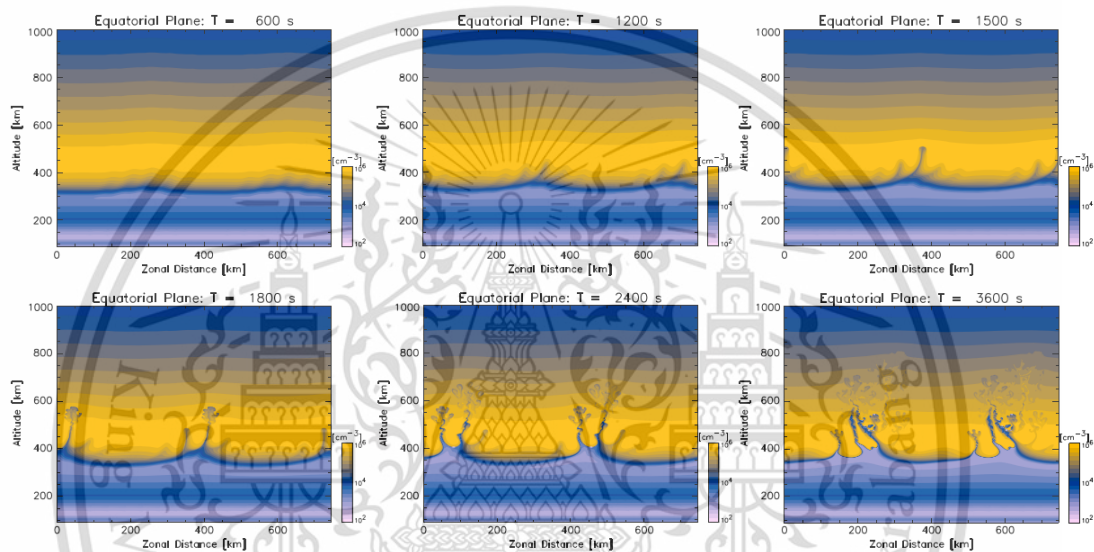


**Figure 2.16:** Distribution of the plasma density depletions on magnetic equatorial planes at different time resolution [22].

Climatological characteristics of the ESF occurrence are influenced by several factors as mentioned above. The day-to-day and short-term variabilities in the ESF occurrence are still not fully understood and accurately predicted using the long-term controlling factors [55]. According to the most recent observatory instruments can indicate that F layer conditions are more important in understanding the ESF characteristics.

## 2.2 Neural Network Models

The artificial intelligence (AI) role is widely increasingly seen in many research areas shown in Figure 2.17. For examples, it is successfully applied in computer vision, cyber-security protection, medical terminology, biology, automatic car self-driving, language models, handwriting recognition, financial analysis, marketing analysis, sport strategy planner, geographic information systems, space weather forecasting, and other fields. The highlights of AI can solve complex scientific problems. Particularly, the success of the deep neural network (DNN) is clearly seen. Computer scientists and related fields spotlight on DNN when [56] exhibits the completeness of the-state-of-the-art

performance on computer vision. In 2016, the smart AI technology is known as Alphago model that performs an incredibility by defeating the world champion professional player in the game of Go competition [57]. In 2023, the most powerful AI model is so-called ChatGPT which is publicly released with amazing responsibility in giving accurate answers to human's questions [58]. In addition, some powerful and useful tools are disclosed to contribute the facilities to language models such as BART and LaMDA [59], [59]. On the other hand, many researchers try to utilize AI technology in solving and modeling space weather. For examples, TEC model, foF2 prediction, hmF2 prediction, NmF2 prediction, Kp index prediction, Spread F prediction, SYM-H and AYM-H prediction, M3000F2 prediction, Disturbance storm time (Dst) index prediction, Equatorial ionospheric vertical plasma drifts model, and Ionospheric scintillation prediction. [60], [61], [62], [63], [64], [65], [66], [67], [68], [69] and [70]. Achievements of the ionospheric forecasting models using the AI technology are rapidly increasing. However, the physics scientists could not fully place their believability on these AI models as a gray box. We can have promising results from these AI models, but the physical mechanisms and dynamics of the target parameters against inputs are not clearly interpreted for several cases.

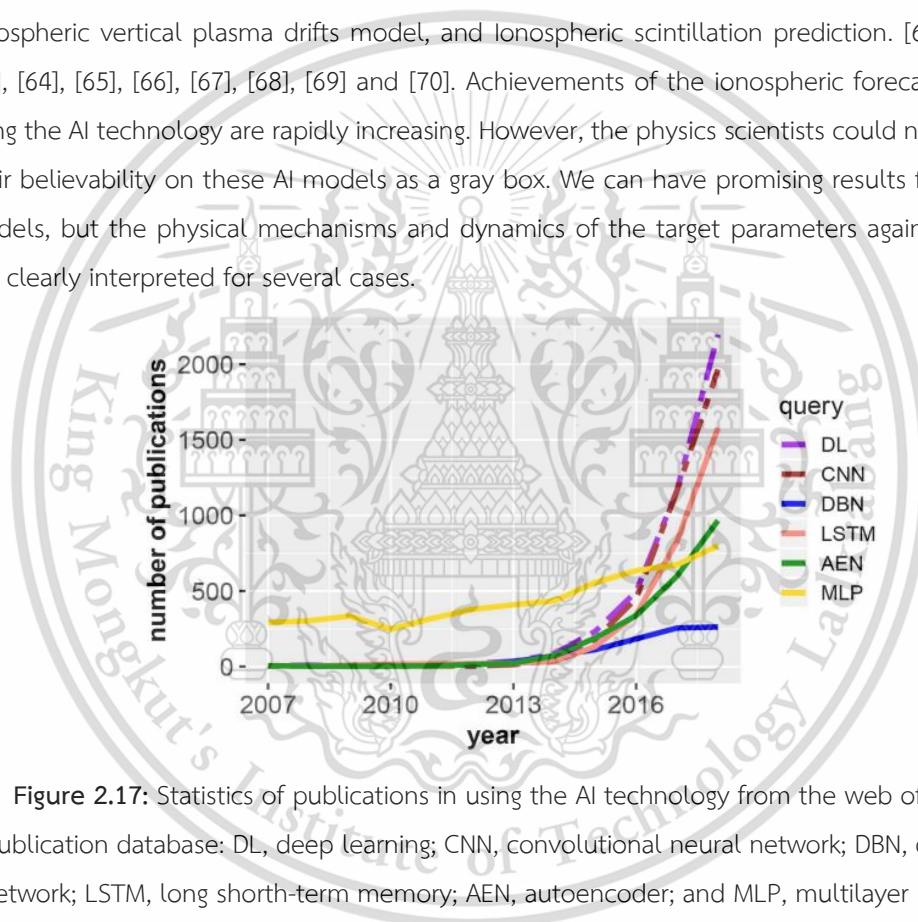


Figure 2.17: Statistics of publications in using the AI technology from the web of science publication database: DL, deep learning; CNN, convolutional neural network; DBN, deep belief network; LSTM, long shorth-term memory; AEN, autoencoder; and MLP, multilayer perceptron.

[71].

### 2.2.1 Artificial Neural Network (ANN)

The ANN is a simple one of the DNNs' family. It is conceptionally designed based on single time step learning, that is, the ANN learns to map the input  $\mathbf{x}$  to the output  $\mathbf{y}$  at the same time. The ANN learning is made on evaluating the deviate value between the actual output or target label and its predicted value. This typical learning is called supervised learning in machine learning. The ANN works on reducing the different values as much as possible, meaning that the actual value and predicted value are very close together when the different value is close to zero. This is a

cause of the ANN network's weight and bias corrections or adjustments. Weight and bias corrections are the result of the learning process with the backpropagation algorithm. The backpropagation algorithm is a backward propagation of the gradients from the output layer through all the network layers. Later, the gradients are major key parameters for adjusting or correcting the weights and biases. In general, the most popular method is the delta rule which is used for weight and bias corrections. Basically, the ANN network is composed of the input layer, hidden or middle layer, and output layer. At the input layer, this layer is automatically defined by the number of input features. At the hidden layer, this layer can contain many layers and neurons. At the output layer, this layer is to produce the final output of the network which can have more than one neuron. Therefore, the ANN network can be mathematically expressed as the following. The output signals at hidden and output layers can be computed by  $y_t^{[l]}$  and  $\hat{y}_t^{[l+1]}$  at given time, respectively.  $l$  is the number of hidden layers. The output layer is always at the last layer  $l$  of the network.

$$y_t^{[l]} = \theta \left( x_t \cdot W_{xh}^{[l]} + b_h^{[l]} \right) \quad 2.17$$

$$\hat{y}_t^{[l+1]} = \theta \left( y_t^{[l]} \cdot W_{hy}^{[l+1]} + b_y^{[l+1]} \right) \quad 2.18$$

where  $\theta(\cdot)$  is any activation function, i.e., "hyperbolic tangent", "softmax", "sigmoid", "ReLU", etc.  $x_t$  is the row input vector in  $R^{1 \times d}$ .  $W_{xh}^{[l]}$  is the weight matrix at layer  $l^{th}$  in  $R^{d \times h}$ .  $b_h^{[l]}$  is the row bias vector in  $R^{1 \times h}$ .  $d$  and  $h$  represents the input feature or number and neuron number.  $W_{hy}^{[l+1]}$  is the weight matrix of the final layer or output layer in  $R^{h \times q}$ .  $b_y^{[l+1]}$  is the row bias vector of the output layer in  $R^{1 \times q}$ . where  $q$  is the neuron number of the output layer. Note that " $\cdot$ " is the dot product operator. The ANN network's structure and neuron is shown in Figure 2.18.

$$\theta(x) = \frac{1}{1 + e^{-x}} \quad 2.19$$

$$\theta(x) = \tanh(x) \quad 2.20$$

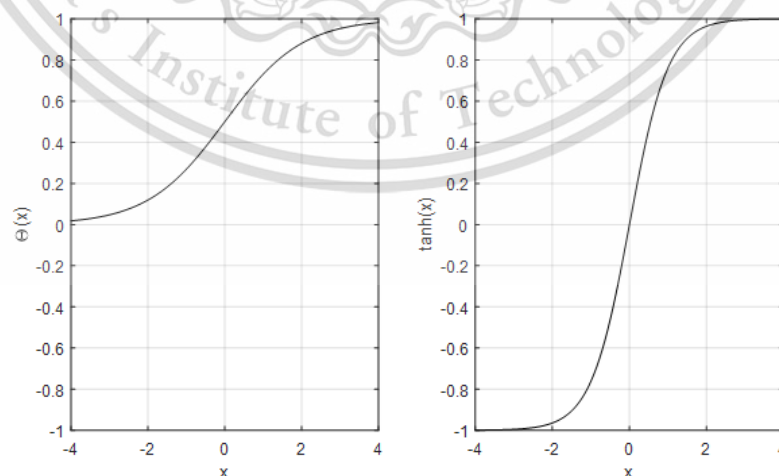


Figure 2.18: Demonstration of the Sigmoid and hyperbolic tangent functions.

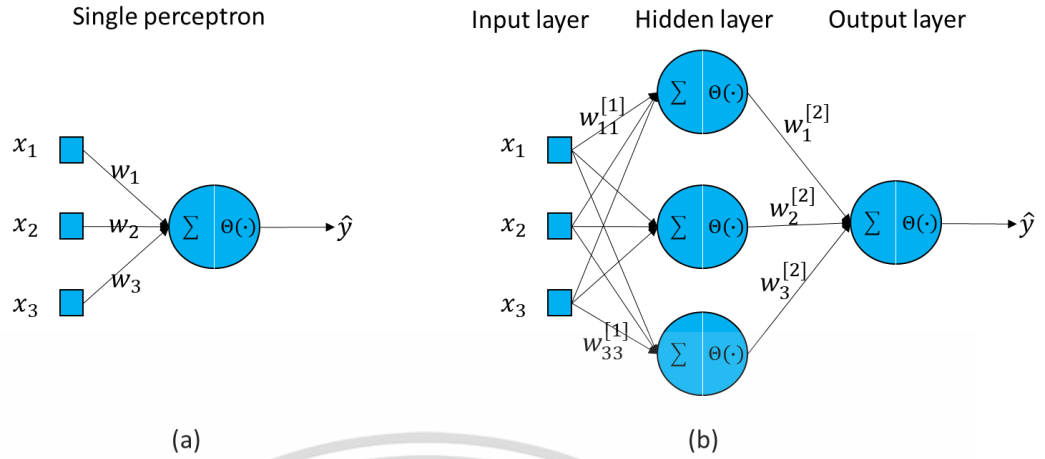


Figure 2.19: The ANN network structure and its neuron unit.

### 2.2.2 Recurrent Neural Network (RNN)

This RNN is an extensive development of the ANN. The single learning timestep of the ANN has learning restriction over the time series data. The ANN learning could not link significant information over multi previous timesteps. Thus, the RNN is designed for expanding the learning timestep capability [72], [73], and [71]. The RNN processes the input signals over multi timesteps. The RNN neuron calculation at the current time depends on the previous times. Thus, the RNN neuron structure is different from the ANN. Linking the RNN neuron over all the time steps is done by the new hidden state  $h_t^{[l]}$ . Calculation of the output signal is made as well as the ANN. Thus, the mathematical RNN model can be expressed as the following.

$$h_t^{[l]} = \tanh(x_t \cdot W_{xh}^{[l]} + h_{t-1}^{[l]} \cdot W_{hh}^{[l]} + b_h^{[l]}) \quad 2.21$$

$$\hat{y}_t^{[l+1]} = \theta(h_t^{[l]} \cdot W_{hy}^{[l+1]} + b_y^{[l+1]}) \quad 2.22$$

where  $h_{t-1}^{[l]}$  is the hidden state at previous timestep in layer  $l^{th}$  in  $R^{1 \times h}$ .  $W_{hh}^{[l]}$  is the weight matrix between the current state and previous state in  $R^{h \times h}$ . Note that this weight connection is shared across all the timesteps.  $h$  is the RNN neuron number.

### 2.2.3 Long Short-Term Memory (LSTM)

The LSMT is also a variant version of the RNN. It is mainly designed to prevent the vanishing gradient problem and expand the learning timestep capability [72] and [73]. The major network structure is still based on the traditional network including the input, hidden, and output layer. The significant development of the LSTM is to control the flow signals and the hidden state by introducing a new cell state ( $c_t^{[l]}$ ) and new four gates. The cell state responsibility is to decide to use or not use the coming signal of the cell state from previous timestep coordinating with the forget gate ( $f_t^{[l]}$ ) and additionally, the input ( $i_t^{[l]}$ ) and aggregated ( $g_t^{[l]}$ ) gates are also a

This material is reserved for educational use only, not allowed for commercial use.

determiner in the cell state for choosing or combing the input signal and the previous hidden state ( $h_{t-1}^{[l]}$ ) into this cell state functionality. For the LSTM hidden state ( $h_t^{[l]}$ ), the output signal of the current LSTM hidden state is controlled by two factors as the output gate ( $o_t^{[l]}$ ) and the cell state at the same time. Consequently, the hidden state signal is directly propagated to the output layer for calculating the output signal ( $\hat{y}_t^{[l+1]}$ ) as well as the RNN. All those LSTM components can be mathematically demonstrated as

$$i_t^{[l]} = \theta \left( x_t \cdot W_{xi}^{[l]} + h_{t-1}^{[l]} \cdot W_{hi}^{[l]} + b_i^{[l]} \right) \quad 2.23$$

$$f_t^{[l]} = \theta \left( x_t \cdot W_{xf}^{[l]} + h_{t-1}^{[l]} \cdot W_{hf}^{[l]} + b_f^{[l]} \right) \quad 2.24$$

$$g_t^{[l]} = \tanh \left( x_t \cdot W_{xg}^{[l]} + h_{t-1}^{[l]} \cdot W_{hg}^{[l]} + b_g^{[l]} \right) \quad 2.25$$

$$c_t^{[l]} = f_t^{[l]} \odot c_{t-1}^{[l]} + i_t^{[l]} \odot g_t^{[l]} \quad 2.26$$

$$o_t^{[l]} = \theta \left( x_t \cdot W_{xo}^{[l]} + h_{t-1}^{[l]} \cdot W_{ho}^{[l]} + b_o^{[l]} \right) \quad 2.27$$

$$h_t^{[l]} = o_t^{[l]} \odot \tanh \left( c_t^{[l]} \right) \quad 2.28$$

$$\hat{y}_t^{[l+1]} = \theta \left( h_t^{[l]} \cdot W_{hy}^{[l+1]} + b_y^{[l+1]} \right) \quad 2.29$$

where  $W_{xi}^{[l]}$  and  $W_{hi}^{[l]}$  are the weight connections of the input gate from the input and previous hidden state at layer  $l^{th}$ .  $W_{xf}^{[l]}$  and  $W_{hf}^{[l]}$  are the weight connections of the forget gate from the input and previous hidden state at layer  $l^{th}$ .  $W_{xg}^{[l]}$  and  $W_{hg}^{[l]}$  are the weight connections of the aggregated gate from the input and previous hidden state at layer  $l^{th}$ .  $W_{xo}^{[l]}$  and  $W_{ho}^{[l]}$  are the weight connections of the output gate from the input and previous hidden state at layer  $l^{th}$ .  $W_{hy}^{[l+1]}$  is the weight connections between the hidden state and output layer at layer  $l^{th} + 1$ .  $b_i^{[l]}$ ,  $b_f^{[l]}$ ,  $b_g^{[l]}$ ,  $b_o^{[l]}$ , and  $b_y^{[l+1]}$  are respectively the biases in input gate, forget gate, aggregated gate, output gate and final output.  $\odot$  is an element-wise product. The graphical structure of the LSTM can be shown in the following figure.

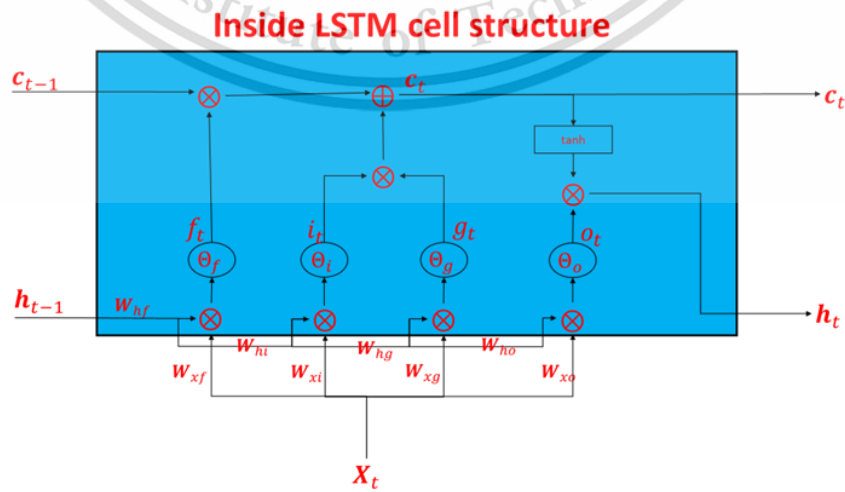


Figure 2.20: The inside LSTM cell structure.

This material is reserved for educational use only, not allowed for commercial use.

Forbidden to modify the content, and cite the document when use.

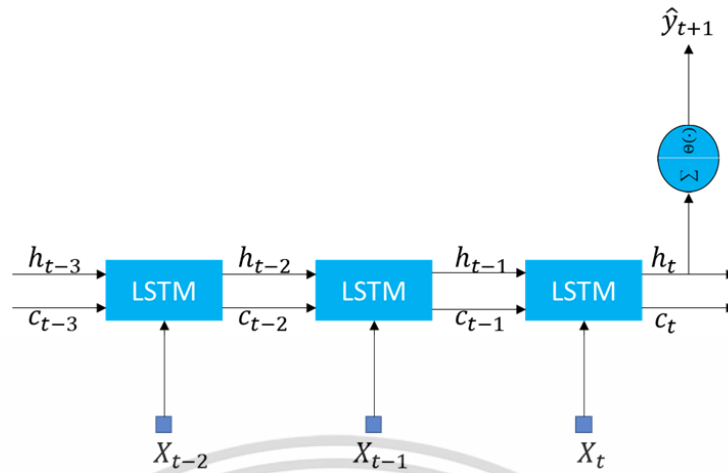


Figure 2.21: The LSTM network structure with many inputs and single output.

### 2.2.3.1 Training the model by backpropagation algorithm

Backpropagation algorithm is a major technique for training the ANN and LSTM networks. At the output layer, the final output is compared to the actual output for obtaining the error of them. The error can be evaluated by any error function. The mean square error (MSE) is used in this work. This error is used in the backpropagation algorithm for adjusting the network’s weights and biases.

$$E(\hat{y}_t, y_t^{target}) = \frac{1}{N} \sum_{i=1}^N (\hat{y}_i - y_i^{target})^2 \tag{2.30}$$

Thus, minimization of this error function is a major task for reaching the convergence of the network training. This can also be called as optimization algorithm by minimizing this error function. Minimization of the error function is dependent on correcting the weights and biases in the network. Correction of the weight and bias is made using the learning rule or so-called the delta rule. For simplicity, we suppose that  $\theta = \{W, b\}$ , where  $W$  and  $b$  represent those all weights and biases in ANN and LSTM networks. Thus, the new correction of the networks’ weights and biases ( $\theta^{new}$ ) can be expressed as the following.

$$\theta^{new} = \theta - \alpha \frac{\partial E}{\partial \theta} \tag{2.31}$$

where  $\alpha$  is the learning rate or learning step,  $\alpha = (0.001, 0.9)$ .  $\frac{\partial E}{\partial \theta}$  is the partial derivative of the error function with respect to weights and biases. Therefore, calculation of the  $\frac{\partial E}{\partial \theta}$  gives the gradients at entire points in the network between the error versus the network’s parameters leading to the final solution. This is also called the gradient descent method. This gradient descent method is mainly used to train both ANN and LSTM networks in this work. The most important rule of this gradient descent algorithm depends on the partial derivative rule so-called the Chain rule. This Chain rule helps us to find the gradients located in sub-functions of the sub-functions, respectively.

For example, we have function  $\hat{y}(x)$  as the followings.

This material is reserved for educational use only, not allowed for commercial use.

Forbidden to modify the content, and cite the document when use.

$$\hat{y}(x) = f(g(x)) \quad 2.32$$

$$\frac{\partial \hat{y}(x)}{\partial x} = \frac{\partial \hat{y}(x)}{\partial f(x)} \frac{\partial f(x)}{\partial g(x)} \frac{\partial g(x)}{\partial x} \quad 2.33$$

For the ANN network, it is simpler than LSTM network because it works on single time step of the pair inputs and target. In contrast, the LSTM network takes the inputs over multiple time steps, thereby the calculation of the gradients must be passed through those multiple time steps. The backpropagation through time (BPTT) algorithm is mainly used in the LSTM network. Now, let's exhibit the Chain rule on our ANN and LSTM networks. For the traditional ANN network, the gradients are derived backward from output layer, hidden layer, and input layer, respectively.

$$\frac{\partial E(\hat{y}_t, y_t^{target})}{\partial W_{hy}} = (\hat{y}_t - y_t^{target}) \left( \hat{y}_t^{[l+1]} (1 - \hat{y}_t^{[l+1]}) \right) y_t^{[l]} \quad 2.34$$

$$\frac{\partial E(\hat{y}_t, y_t^{target})}{\partial b_y} = (\hat{y}_t - y_t^{target}) \left( \hat{y}_t^{[l+1]} (1 - \hat{y}_t^{[l+1]}) \right) 1 \quad 2.35$$

$$\frac{\partial E(\hat{y}_t, y_t^{target})}{\partial W_{xh}} \quad 2.36$$

$$= (\hat{y}_t - y_t^{target}) \left( \hat{y}_t^{[l+1]} (1 - \hat{y}_t^{[l+1]}) \right) W_{hy}^{[l+1]} \left( y_t^{[l]} (1 - y_t^{[l]}) \right) x \quad 2.37$$

$$\frac{\partial E(\hat{y}_t, y_t^{target})}{\partial b_h} = (\hat{y}_t - y_t^{target}) \left( \hat{y}_t^{[l+1]} (1 - \hat{y}_t^{[l+1]}) \right) W_{hy}^{[l+1]} \left( y_t^{[l]} (1 - y_t^{[l]}) \right) 1$$

These gradients are plugged into the delta function for computing correction of the new weights and biases. Thus, this process is repeated until training epoch and the minimum error goal is reached. Optionally, it can be stopped early when the early stop criterion is reached as well.

Training the RNN and LSTM networks is based on the same algorithm, thereby, only the LSTM training is described in this work. For the LSTM network, training the LSTM network can be completed using the gradient descent as well as the ANN network. However, the LSTM learning is slightly different to the ANN depending on its network architecture. The LSTM network contains more activation functions in each LSTM unit/cell. Also, the output of the LSTM network is gained using the inputs over many feedback loops or learning timesteps. The gradients must be passed through the entire network and over the feedback loops. In more detail, it is expressed as the following.

Suppose that the LSTM network is based on many inputs and single output as shown in Figure 2.21. At the output layer, we need to find only a single gradient at the final timestep. The gradients are obtained with respect to both weight and bias as

$$\frac{\partial E(\hat{y}_t^{[l+1]}, y_t^{target})}{\partial W_{hy}} = (\hat{y}_t - y_t^{target}) \left( \hat{y}_t^{[l+1]} (1 - \hat{y}_t^{[l+1]}) \right) h_t^{[l]} \quad 2.38$$

$$\frac{\partial E(\hat{y}_t^{[l+1]}, y_t^{target})}{\partial b_y} = (\hat{y}_t - y_t^{target}) \left( \hat{y}_t^{[l+1]} (1 - \hat{y}_t^{[l+1]}) \right) 1 \quad 2.39$$

where  $(\hat{y}_t^{[l+1]}(1 - \hat{y}_t^{[l+1]}))$  is derived from taking partial derivative of the Sigmoid function. In this case, we have the gradient at the output layer for considering only the single output unit at time step  $t^{th}$ . Next step is to compute the gradients at the hidden layer which contains cells through loopbacks/timesteps.

$$\frac{\partial E(\hat{y}_t^{[l+1]}, y_t^{target})}{\partial h_t^{[l]}} = (\hat{y}_t^{[l+1]} - y_t^{target}) (\hat{y}_t^{[l+1]} (1 - \hat{y}_t^{[l+1]})) W_{hy} \quad 2.40$$

The gradient with respect to  $h_t^{[l]}$  at the last time step  $t$  is considered. Then it is backpropagated through the LSTM at the current time step  $t$

$$\frac{\partial E(\hat{y}_t^{[l+1]}, y_t^{target})}{\partial o_t^{[l]}} = \frac{\partial E(\hat{y}_t^{[l+1]}, y_t^{target})}{\partial h_t^{[l]}} \tanh(c_t^{[l]}) \quad 2.41$$

$$\frac{\partial E(\hat{y}_t^{[l+1]}, y_t^{target})}{\partial c_t^{[l]}} = \frac{\partial E(\hat{y}_t^{[l+1]}, y_t^{target})}{\partial h_t^{[l]}} W_{hy} (o_t^{[l]} (1 - \tanh(c_t^{[l]})^2)) \quad 2.42$$

$$\frac{\partial E(\hat{y}_t^{[l+1]}, y_t^{target})}{\partial i_t^{[l]}} = \frac{\partial E(\hat{y}_t^{[l+1]}, y_t^{target})}{\partial c_t^{[l]}} g_t^{[l]} \quad 2.43$$

$$\frac{\partial E(\hat{y}_t^{[l+1]}, y_t^{target})}{\partial f_t^{[l]}} = \frac{\partial E(\hat{y}_t^{[l+1]}, y_t^{target})}{\partial c_t^{[l]}} c_{t-1}^{[l]} \quad 2.44$$

$$\frac{\partial E(\hat{y}_t^{[l+1]}, y_t^{target})}{\partial g_t^{[l]}} = \frac{\partial E(\hat{y}_t^{[l+1]}, y_t^{target})}{\partial c_t^{[l]}} i_t^{[l]} \quad 2.45$$

We now have the gradient with respect to all gates in the LSTM. Further, the gradients with respect to weights over the whole sequence can be derived as

$$\frac{\partial E(\hat{y}_t^{[l+1]}, y_t^{target})}{\partial W_{xo}^{[l]}} = \sum_t \frac{\partial E(\hat{y}_t^{[l+1]}, y_t^{target})}{\partial o_t^{[l]}} o_t^{[l]} (1 - o_t^{[l]}) x_t \quad 2.46$$

$$\frac{\partial E(\hat{y}_t^{[l+1]}, y_t^{target})}{\partial W_{xi}^{[l]}} = \sum_t \frac{\partial E(\hat{y}_t^{[l+1]}, y_t^{target})}{\partial i_t^{[l]}} i_t^{[l]} (1 - i_t^{[l]}) x_t \quad 2.47$$

$$\frac{\partial E(\hat{y}_t^{[l+1]}, y_t^{target})}{\partial W_{xf}^{[l]}} = \sum_t \frac{\partial E(\hat{y}_t^{[l+1]}, y_t^{target})}{\partial f_t^{[l]}} f_t^{[l]} (1 - f_t^{[l]}) x_t \quad 2.48$$

$$\frac{\partial E(\hat{y}_t^{[l+1]}, y_t^{target})}{\partial W_{xg}^{[l]}} = \sum_t \frac{\partial E(\hat{y}_t^{[l+1]}, y_t^{target})}{\partial g_t^{[l]}} (1 - g_t^{[l]}) x_t \quad 2.49$$

We notice that the weights  $W_{xo}^{[l]}$ ,  $W_{xi}^{[l]}$ ,  $W_{xf}^{[l]}$ , and  $W_{xg}^{[l]}$  are shared through the whole sequence. Thus, those all gradients are summed up together over  $t$  as the followings.

$$\frac{\partial E(\hat{y}_t^{[l+1]}, y_t^{target})}{\partial W_{ho}^{[l]}} = \sum_t \frac{\partial E(\hat{y}_t^{[l+1]}, y_t^{target})}{\partial o_t^{[l]}} o_t^{[l]} (1 - o_t^{[l]}) h_{t-1}^{[l]} \quad 2.50$$

$$\frac{\partial E(\hat{y}_t^{[l+1]}, y_t^{target})}{\partial W_{hi}^{[l]}} = \sum_t \frac{\partial E(\hat{y}_t^{[l+1]}, y_t^{target})}{\partial i_t^{[l]}} i_t^{[l]} (1 - i_t^{[l]}) h_{t-1}^{[l]} \quad 2.51$$

$$\frac{\partial E(\hat{y}_t^{[l+1]}, y_t^{target})}{\partial W_{hf}^{[l]}} = \sum_t \frac{\partial E(\hat{y}_t^{[l+1]}, y_t^{target})}{\partial f_t^{[l]}} f_t^{[l]} (1 - f_t^{[l]}) h_{t-1}^{[l]} \quad 2.52$$

$$\frac{\partial E(\hat{y}_t^{[l+1]}, y_t^{target})}{\partial W_{hg}^{[l]}} = \sum_t \frac{\partial E(\hat{y}_t^{[l+1]}, y_t^{target})}{\partial g_t^{[l]}} (1 - g_t^{[l]}) h_{t-1}^{[l]} \quad 2.53$$

In terms of the hidden and cell states, the gradients pass through these states ( $h_{t-1}^{[l]}$  and  $c_{t-1}^{[l]}$ ) are also considered at time  $(t-1)^{th}$ . For the hidden state, the two sources of the gradients come from the activation and the cost or error functions as

$$\begin{aligned} & \frac{\partial E(\hat{y}_t^{[l+1]}, y_t^{target})}{\partial h_{t-1}^{[l]}} \\ &= \frac{\partial E(\hat{y}_t^{[l+1]}, y_t^{target})}{\partial o_t^{[l]}} o_t^{[l]} (1 - o_t^{[l]}) W_{ho}^{[l]} \\ &+ \frac{\partial E(\hat{y}_t^{[l+1]}, y_t^{target})}{\partial i_t^{[l]}} i_t^{[l]} (1 - i_t^{[l]}) W_{hi}^{[l]} \\ &+ \frac{\partial E(\hat{y}_t^{[l+1]}, y_t^{target})}{\partial f_t^{[l]}} f_t^{[l]} (1 - f_t^{[l]}) W_{hf}^{[l]} \\ &+ \frac{\partial E(\hat{y}_t^{[l+1]}, y_t^{target})}{\partial g_t^{[l]}} (1 - g_t^{[l]}) W_{hg}^{[l]} \end{aligned} \quad 2.54$$

$$\frac{\partial E(\hat{y}_t^{[l+1]}, y_t^{target})}{\partial h_{t-1}^{[l]}} = \frac{\partial E(\hat{y}_t^{[l+1]}, y_t^{target})}{\partial h_{t-1}^{[l]}} + \frac{\partial E(\hat{y}_t^{[l+1]}, y_t^{target})}{\partial \hat{y}_{t-1}^{[l]}} W_{hy} \quad 2.55$$

In terms of  $\frac{\partial E(\hat{y}_t^{[l+1]}, y_t^{target})}{\partial \hat{y}_{t-1}^{[l]}} W_{hy}$ , it is considered when the LSTM model with multiple output units is used. In the cell state, the gradients are associated with previous time step  $(t-1)^{th}$  as well, hence, it can be derived as

$$\frac{\partial E(\hat{y}_t^{[l+1]}, y_t^{target})}{\partial c_{t-1}^{[l]}} \quad 2.56$$

$$\begin{aligned} &= \frac{\partial E(\hat{y}_t^{[l+1]}, y_t^{target})}{\partial h_t^{[l]}} \frac{\partial h_t^{[l]}}{\partial c_t^{[l]}} \frac{\partial c_t^{[l]}}{\partial c_{t-1}^{[l]}} + \frac{\partial E(\hat{y}_{t-1}^{[l+1]}, y_{t-1}^{target})}{\partial h_{t-1}^{[l]}} \frac{\partial h_{t-1}^{[l]}}{\partial c_{t-1}^{[l]}} \\ &\frac{\partial E(\hat{y}_t^{[l+1]}, y_t^{target})}{\partial c_{t-1}^{[l]}} = \frac{\partial E(\hat{y}_t^{[l+1]}, y_t^{target})}{\partial c_{t-1}^{[l]}} + \frac{\partial E(\hat{y}_t^{[l+1]}, y_t^{target})}{\partial c_t^{[l]}} f_t^{[l]} \end{aligned} \quad 2.57$$

In Eq. 2.56 and 2.57, the right terms are added when the multiple output units are considered.

Finally, the backpropagation through time can be briefly summarized as the following steps.

- 1) Compute the output signal from the model.
- 2) Compute the cost or error function between the actual output and predicted output at the output layer.

- 3) Find the gradients of the error function with respect to all the parameters passed through all loopbacks or timesteps of the network.
- 4) Correct or adjust the network's parameters over loopbacks using learning rule or so-called delta rule for all parameters.
- 5) Check the error value in 2), if error is not satisfied or converged, then repeat 2) – 5). If the error is satisfied or converged, then stop the program.

## 2.2.4 Performance metrics in classification

In this part, we evaluate the model performance depending on the confusion matrix as shown in Figure 2.22. The confusion matrix is designed to interpret the model performance for the classification problems [74] and [75]. The confusion matrix exhibits summary of the model prediction against the real values. For example, the classification of two classes of 1 and 0 is represented by false/incorrect (F) and true/correct (T) of both classes. As shown in the confusion matrix, the class 0 and 1 are indicated by letter “N” and “P”, respectively. Thus, TN and TP represent correct prediction by matching the predicted values with the real values for both classes 0 and 1. In contrast, FN and FP denote the incorrect prediction. In addition, the correct prediction rate of the model is also exhibited for two classes as seen in the total box.

		Model		
		Class 0	Class 1	total
Actual	Class 0	TN	FN	$TN/(TN+FN)$
	Class 1	FP	TP	$TP/(TP+FP)$
total		$TN/(TN+FP)$	$TP/(TP+FN)$	$(TN+TP)/(TN+FN+TP+FP)$

Figure 2.22: Analysis of the Model performance using confusion matrix.

In the confusion matrix, we also utilize four factors as recall, precise, F1 score and accuracy for exhibiting the model performance. In the accuracy index, it is insufficiently used when the data classes are imbalanced. The recall, precise and F1 score parameters are used to exhibit the model performance besides the accuracy. These three indicators are robust with the imbalanced data.

$$\text{Accuracy} = \frac{TP+TN}{TP+TN+FP+FN} \quad 2.58$$

$$\text{Recall} = \frac{TP}{TP+FN} \quad 2.59$$

$$\text{Precise} = \frac{TP}{TP+FP}, \quad 2.60$$

$$\text{F1 score} = \frac{2}{\left(\frac{1}{\text{Recall}} + \frac{1}{\text{Precise}}\right)}, \quad 2.61$$

### 2.2.5 Role of AI on ionospheric forecasting models

The development of ionospheric forecasting models has become a significant topic in space research for decades. Forecasting model for the ESF events has been developed since 2003 by [15]. Some studies also continue development of the ESF forecasting model [65], [76], [64], [77], and [78]. These studies perform capabilities of the AI models and statistical methods to fuel the ESF forecasting model improvement. Hence, we notice that the state-of-the-art artificial intelligence (AI) is awarded to deep learning (DL). The DL is named due to the enhancement of the model's complexity. For the DL reviews, several aspects, and successes of the DL on prediction models are exhibited in study of [71]. One powerful method of the DL is called an artificial neural network (ANN). First invention of the ANN is inspired by the human brain functionality [79] and [80]. The fulfillments of this model are discussed in part above. In addition, the learnability of the ANN model is improved to have long recognition [72]. The neural structure is redesigned to handle vanishing and exploding gradient issues. It is well-known as Recurrent Neural Network (RNN) or Long Short-Term Memory (LSTM). The time series data is one of the unique scientific problems with time and seasonal dependences. This typical problem is related to weather variations, space weather variations and so on. Therefore, the LSTM model is more appropriate to this time series data. The advantages and robustness of the LSTM model with long-time step learning and advanced neuron functions. The LSTM model's learning is flexible with both shorth and long terms. Thus, this crucial point of the LSTM model is able to enhance the memorability by connecting the current state to previous states through functions of the hidden and cell states [73] and [72].

## Chapter 3 The designed and proposed methods

### 3.1 Study of the ESF characteristics at longitudinal stations

The ESF data is retrieved using the FMCW and CADI ionosonde systems at CPN and TIR stations, respectively. The specifications of these two ionosondes are given as shown in Table 1. These two stations are significantly located near the magnetic equator as shown in Figure 3.1. The location of these two stations is a unique station of four stations in the world, which is near the magnetic equator field. Therefore, the comparative study of the ESF characteristics can significantly contribute to more understandings in dimensions of locations and day-to-day variations.

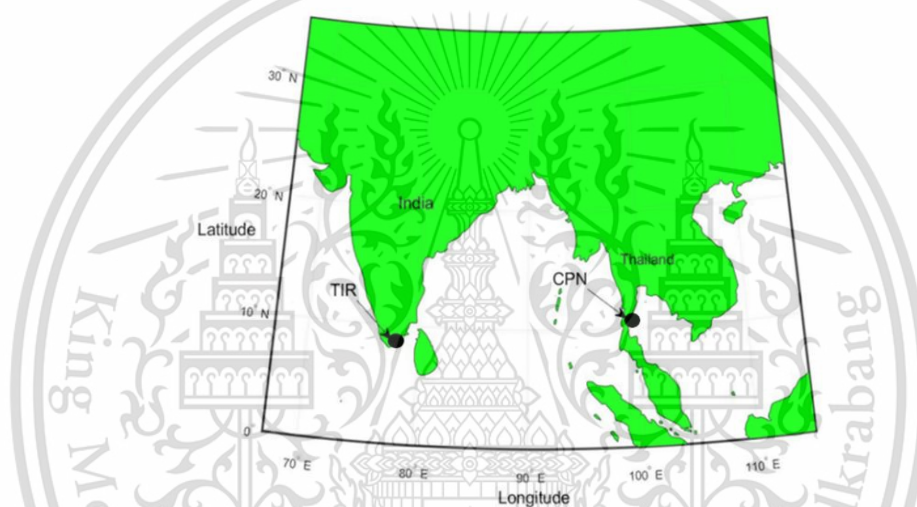


Figure 3.1: Geographical locations of CPN and TIR stations.

#### 3.1.1 Characterizing the ESF monthly occurrence rate

In this experiment, it is to compare characteristics of the ESF monthly occurrence rate between the CPN and TIR stations. The ESF data are obtained with two-time resolutions as 15 and 10 minutes in 2008 and 2014 for the TIR station. At the CPN station, the ESF data resolution is operated on 15 minutes for 2008 and 2014. These two stations are in different local time zones such as the CPN station with UT + 7.0 and the TIR station with UT + 5.5. The comparative results between these stations are based on the local time such as the local time at the CPN station is obtained by adding the UT with 7.0 and the TIR station with 5.5. One of the ESF characteristics has been widely presented as the monthly probability occurrence. It is represented by summing the ESF occurrence at each time in month and dividing it by total number of days in month. In general, the ESF events can usually be observed after sunset until early morning. Thus, the ESF monthly occurrence rate is only considered from 11:00 to 23:45 UT or 18:00 to 06:45 LT. It can be expressed as

This material is reserved for educational use only, not allowed for commercial use.

Forbidden to modify the content, and cite the document when use.

$$P_t = \sum_{i=1}^N \frac{ESF_{i,t}}{N} \times 100 \quad 3.1$$

where  $ESF_{i,t}$  represents either 0 and 1 as absence and presence of the ESF at time  $t^{th}$  ( $t = 11, 11.15, 11.30, 11.45, 12, \dots, 23.45$ ) on day  $i^{th}$  ( $i = 1, 2, \dots, 30/31$ ), and  $N$  is the total number of observation days in a month.

### 3.1.2 ESF onset and duration

In this part, our main purpose is to quantify and understand the attributes of the ESF's initial and developing generations between the CPN and TIR stations. The onset time and existing duration of the ESF occurrence are considered in this experiment. The ESF durations are determined as the continuous existence from the start to the end time. The study of the ESF durations is divided into the post-sunset period (18:00 LT to 23:45 LT) and the post-midnight period (00:00 LT to 06:45 LT). The ESF durations are expressed in hour and frequency for each duration. The comparison of the ESF onsets at both stations is demonstrated by the number of the onset ESF against with the local time. Furthermore, the ESF durations of at least 30 minutes are used for avoiding the outlier data.

On this part, we study estimation of the ESF onset at the CPN station by considering the ESF onset at the TIR station. The TIR station is located at the UT +5.5 while the CPN station at the UT +7.0. It is known that the ESF development usually moves from the east direction to the west direction. Thereby, it is possible to estimate the ESF occurrence at the CPN station where is in western part of the TIR station as shown in Figure 3.2. It is assumed that the ESF onset is observed earlier at TIR station than at the CPN station by remarkably representing as TIR+ and TIR- indicates the ESF onset is observed at the TIR station after at the CPN station. Therefore, the ESF onset statistics are used to estimate the ESF occurrence at the CPN station.

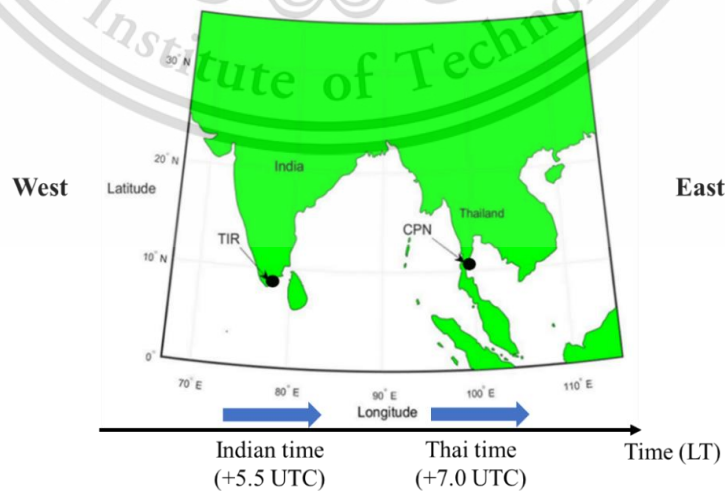


**Figure 3.2:** Geographical map of the TIR and CPN stations on assumption of estimating the ESF events.

This material is reserved for educational use only, not allowed for commercial use.

Forbidden to modify the content, and cite the document when use.

### 3.2 ESF forecasting models

As shown in Figure 3.3, the research experiments are implemented following the processes. The ionogram data is obtained from the ionosonde instrument at the CPN station. The global solar and magnetic data can be downloaded from OMNIWeb Data Explorer, NASA and World Data Center, Kyoto [81], [82]. The local ionospheric characteristics are derived from the ionogram image including the ESF, h'F, and foF2 parameters. The global input parameters are mainly considered as solar and magnetic indices. These ionospheric parameters are manually recorded using the special software. The entire data sets are cleaned, selected, and retrieved in procedures within the data preparation. In addition, some constructed atmospheric parameters are also processed such as the Vd and AGW indices. Before training the Deep Neural Networks, the input signals are adjusted using a min-max normalization method. Next, the DNNs are trained and tested for the model selection. Finally, the best model is obtained and assigned as the main model for the ESF forecasting model.

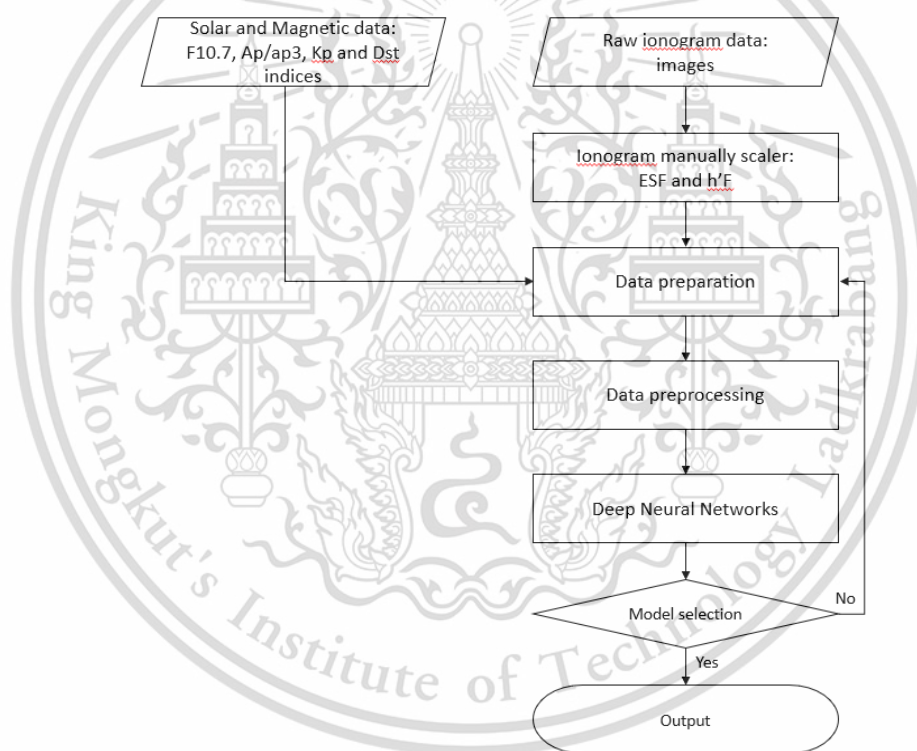


Figure 3.3: Flowchart of the research process.

#### 3.2.1 Data selection and preparation

The ESF value is obtained from the manual collection using the ionogram scaler software. In addition, we utilize the ESF probability from the IRI model for validation with the real data and proposed model. The ESF probability is one of the IRI model's parameters which is developed in study of [15]. Development of the ESF model in the IRI model only depends on the ESF data at two stations in Brazil. For the ESF data, the ESF events are represented by a binary 0 and 1 for absence and presence of the ESF events, respectively. The ESF presence is considered only when

the ESF duration is observed for at least an hour. If the ESF duration is shorter than an hour, it is defined as absence of the ESF events. The upward drift velocity is retrieved by differentiating the h'F with respect to the time under 15 minutes of the time window [27]. The power spectrum of the atmospheric gravity waves is derived using the Wavelet transformation (Morlet Wavelet) analyzing on the foF2 signal within 30 – 90 minutes of the Wavelet's periodicities [28] and [35]. The diurnal and seasonal indices are cyclically converted using the sine and cosine functions [65] and [60]. Moreover, the detected missing values are replaced using linear interpolation. All the input parameters are scaled using the standardization method. The predicted output of the ANN or LSTM model are obtained in floating numbers. Therefore, the predicted output is classified as either 0 or 1 using 0.5 as the threshold value.

The standardization method is used to scale the input signals before feeding them into the network in this work. The standard method works on subtraction and division of the original data ( $x$ ) by mean and standard deviation values, respectively. It can be expressed as the following.

$$x^* = \frac{x - \mu_x}{\sigma_x^2} \quad 3.2$$

where  $\mu_x$  and  $\sigma_x^2$  are mean and standard deviation, respectively. The new standardized data will have mean and variance values close to 1 and 0, respectively.

Missing data is handled using linear interpolation. This is only applied to the missing data in the h'F and foF2 parameters. In this work, one-dimensional linear interpolation for monotonically increasing sample points is applied based on the Numpy library (<https://numpy.org/doc/stable/reference/generated/numpy.interp.html>).

In general, the ESF variations can be characterized depending on seasonal and diurnal changes. The seasonal and diurnal indices are the significant parameters for the ESF forecasting model. These two parameters can benefit the ESF model recognition in terms of seasonal and diurnal variations. The seasonal and diurnal indices are represented by day (1 – 365/366) and hour (0 – 24) numbers, respectively. As seen in day and hour numbers, they have discrete connection between year to year and day to day. Thus, these parameters are generally converted using sine and cosine functions for the continuity. Some previous studies exhibit the utilization of these parameters in their models including foF2 model, M3000F2 model, TEC model, and hmF2 model [61], [60] and [62].

$$Ts = \sin\left(\frac{2\pi \times Hn}{24}\right) \quad 3.3$$

$$Tc = \cos\left(\frac{2\pi \times Hn}{24}\right) \quad 3.4$$

$$Ds = \sin\left(\frac{2\pi \times Dn}{365.25}\right) \quad 3.5$$

$$Dc = \cos\left(\frac{2\pi \times Dn}{365.25}\right) \quad 3.6$$

This material is reserved for educational use only, not allowed for commercial use.

Forbidden to modify the content, and cite the document when use.

where 24 is the total number of hours and 356.25 is used due to the included leap year in the data set, [60].

### 3.2.2 Input design for ESF forecasting models

The model input parameters are designed depending on both possible natural relationships with the ESF events. In the global scale, the solar and magnetic activities are the significant parameters in characterizing the ESF occurrence in seasonal variations. They are mainly used in the global ionospheric empirical model such as the IRI model. Thus, selection of the input parameters is considered through direct and indirect influencing parameters which are investigated in previous studies. Correlative measurements between input parameters against the ESF are mainly relied on reported information in previous studies.

Solarization is a major source that causes ionospheric plasma variations. Besides, the magnetic field also plays a role in the ionospheric variations. These two parameters are globally studied and applied in various global and local models. The important solar indices are widely used as the F10.7cm solar flux emission (F10.7cm) and sunspot number (SSN). The seasonal ESF characteristics can be quantified by the solar indices. In general, the enhancement of the ESF occurrence rate is related to increases in solar activity. On the other hand, the earth magnetosphere is one of the important indicators in describing the disturbance in ionospheric layer. For instance, some works have successfully used these two parameters in developing the ionospheric models such as foF2 model, hmF2 model, Dst model, MUF model, Spread-F model, TEC model, and others. Therefore, these important solar and magnetic parameters are used in the ESF forecasting model.

The input combinations are designed to investigate the significant input feature and case study of the new local parameters for improving the ESF model. The entire input features are included as hour number (Hn), day number (Dn), F10.7cm, SSN, ap3 and Ap, kp3 and Kp, h'F, upward drift velocity of F layer (Vd), and atmospheric gravity waves (AGW). The input-based parameter is first defined as input A for finding the best network structure and loopbacks. Later, the best network with input-based parameters is onward utilized to find the best input combination as the following.

**Table 2:** Designs of the input combinations for the ANN and LSTM models.

Input	Input feature
A	Ts, Tc, Ds, Dc, SSN, ap3
B	Ts, Tc, Ds, Dc, SSN, ap3, h'F
C	Ts, Tc, Ds, Dc, SSN, ap3, Vd
D	Ts, Tc, Ds, Dc, SSN, ap3, AGW
E	Ts, Tc, Ds, Dc, SSN, ap3, Vd, AGW

As designed input combinations in Table 2, input features are designed to express the important role of new local ionospheric parameters. These  $h'F$ ,  $Vd$ , and  $AGW$  indices are importantly investigated in indicating the ESF generations [77], [28], [7]. In addition, this study case is aimed to prove the significant role of those local ionospheric parameters on the ESF prediction model. The optimal network structure is derived by considering the confusion matrix factors. The prediction step of the ANN and LSTM models is made at 0.5 hours or 30-minute ahead.

### 3.2.3 Deployment of the ESF models

The ESF forecasting model is mainly designed using the ANN and LSTM networks depending on one step ahead prediction. That is, the models are trained to produce the one step ahead prediction. The ANN model learning is dependent on single step of the input and output target pairs. Successfulness of the ANN model on classification problems is widely seen in various application areas. However, the competition between the LSTM and ANN models on time series forecasting has shown that the LSTM model can outperform the ANN model in several dimensions. One of the LSTM model advantages is flexibility learning more than single step. In addition, the advanced LSTM neuron is also a significant key in achieving the long-short recognition in the time series data. Therefore, the ESF model development is considered and placed onto the most powerful machine learning techniques.

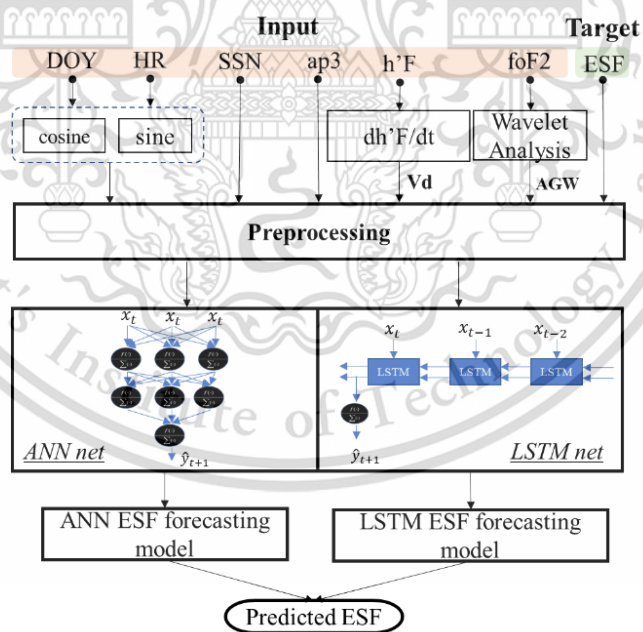


Figure 3.4: Diagram of the ESF model by the ANN and LSTM network.

## Chapter 4 Results and Discussions

In this part, the comparative results of the ESF statistics are presented between the TIR and CPN stations. Secondly, the results of the proposed LSTM model are compared to the real observed values, the ANN model, and the IRI model. We use the ESF data in equinoxes which cover the 24<sup>th</sup> solar cycle from 2008 to 2019 as shown in Figure 4.1. The data coverage over at least one solar cycle is necessary for quantifying and characterizing the ESF phenomena. The available ionogram data is demonstrated in Figure 4.2. The scanty and missing data are excluded from the study, i.e., 2017. As shown in Figure 4.3, we can see the high number of days with the available data in March, April, August, October, September, and February. In addition, the ESF data sample is mainly used to train and test the forecasting models as shown in Table 3. The ESF presence or class 1 has more than 77.9% and 87.1% for training and testing sets and otherwise, 22.1% and 12.9% of the ESF absence or class 0.

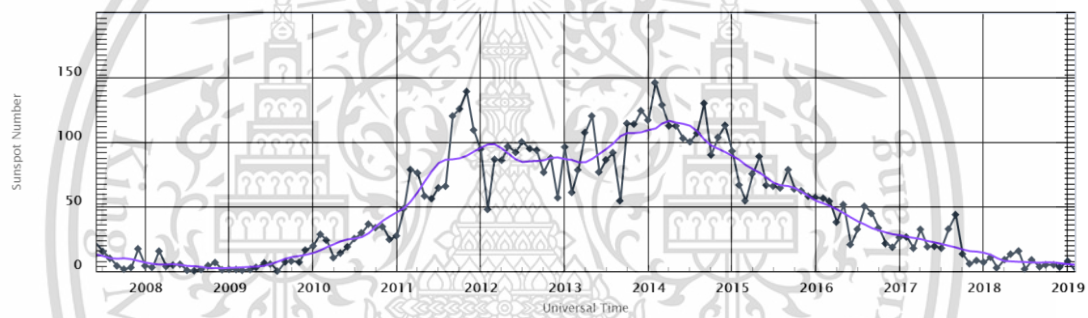


Figure 4.1: Sunspot number (SSN) of the 24<sup>th</sup> solar cycle [81].

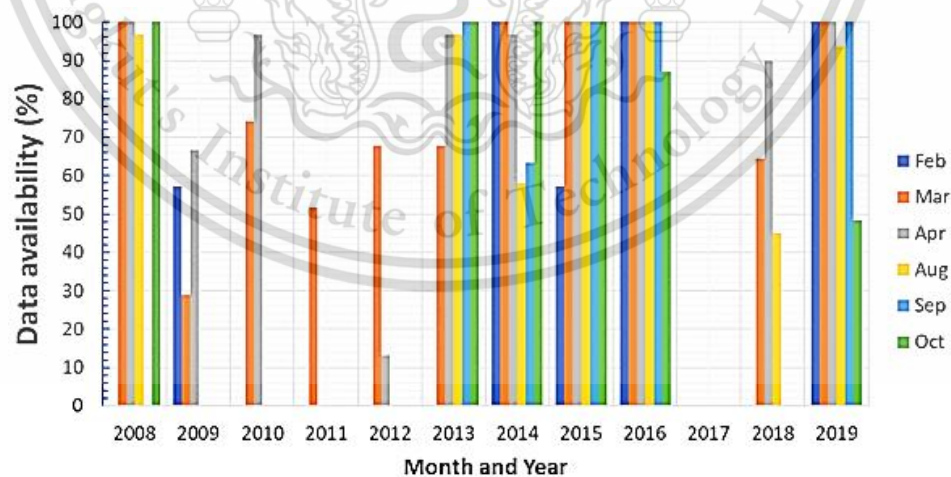


Figure 4.2: The availability of the ionogram data at CPN station.

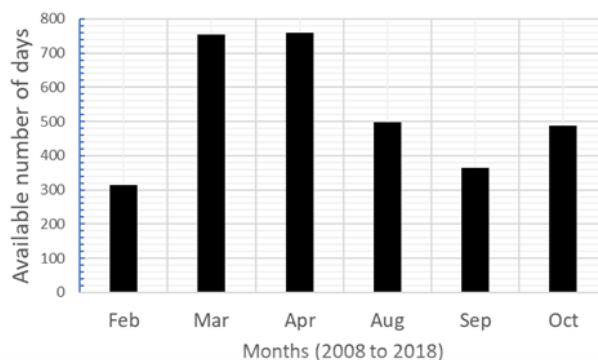


Figure 4.3: The amount of available data in each month from 2008 to 2019 at CPN station.

Table 3: Data portion of the training and testing sets.

	ESF-classes	
	ESF-1	ESF-0
Training set = 19,600	4,340 (22.1%)	15,260 (77.9%)
Testing set = 3,080	398 (12.9%)	2,682 (87.1%)

#### 4.1 Comparison of ESF characteristics at CPN and TIR stations

The statistics of the ESF events at CPN and TIR stations are analyzed in this section. The two different years in LSA (2008) and HAS (2014) are considered for showing the solar significant role on the variations of the ESF events. The statistical ESF events are analyzed in four equinoctial months such as February, March, April, August, September, and October. These months are well known with the high occurrence rate of the ESF events [42]. Thus, it is significantly focused on these months at both CPN and TIR stations. As shown in Table 2, the monthly mean values of magnetic Ap and F10.7 solar flux indices are demonstrated and utilized to illustrate behavioral changes of the solar and magnetic indices. It is noticed that the Ap values in March and April in 2008 are higher than in 2014 and in September and October in 2014 are higher than 2008. This clearly indicates the independent variations of the Ap value between LSA and HSA. For the solar index, the F10.7 values in HSA are higher than in LSA for each month.

Table 4: The averaged values of Ap and F10.7 indices in each month during 2008 (LSA) and 2014 (HSA).

	Mean values of the Ap index		Mean values of the F10.7 solar flux (s.f.u)	
	LSA	HSA	LSA	HSA
March	11.2	4.9	72.2	148.1
April	9.6	8.0	70.6	145.3
September	5.8	9.8	67.9	149.3
October	6.6	9.1	67.8	154.0

This material is reserved for educational use only, not allowed for commercial use.

Forbidden to modify the content, and cite the document when use.

#### 4.1.1 Day-to-day variability in the ESF occurrences

In this section, the day-to-day variability of the ESF occurrences in LSA and HSA years at CPN and TIR stations is demonstrated in Figure 4.4 and Figure 4.5. The top panel's y-axis respectively shows the daily Ap and F10.7 values by red graph with dot and blue graph with rectangle and x-axis represents day of year (DOY). The two bottom panels show the ESF events against local time (18:00 to 06:45) and DOY at CPN and TIR stations, respectively. The yellow means to the ESF presence and otherwise, ESF absence. In Figure 4.4, the most daily F10.7 values are below 72 s.f.u, except during DOY 84 to 95 the F10.7 values are higher. Also, when we look at the daily Ap values each month. It is noticed that the Ap index in March and April has fluctuations and higher values more than in September and October. The ESF generation is observed after 18:00 LT in each month at both stations. The day-to-day occurrence of the ESF has similar patterns between CPN and TIR stations. In addition, the different characteristics at these stations can be distinguished as the ESF durations at TIR station are almost longer than at CPN station, and the existence of the ESF occurrence appears after midnight until 05:30 LT (March and April) and 04:00 LT (September and October) at TIR station, while until 02:30 LT (March and April) and 05:00 LT in a few days (September and October) at CPN station. Post-midnight ESF occurrences are more frequent at TIR station than at CPN station. Significantly, the days with the Ap index above 18 cause the nonoccurrence of the ESF over both stations. Therefore, these are indicated that the day-to-day of the ESF characteristics at these stations have positive relationships due to the equatorial dependence and on the other hand, their ESF occurrence patterns have a unique characteristic based on the local conditions. The frequent ESF occurrence is observed with low F10.7 and Ap values at both stations in LSA.

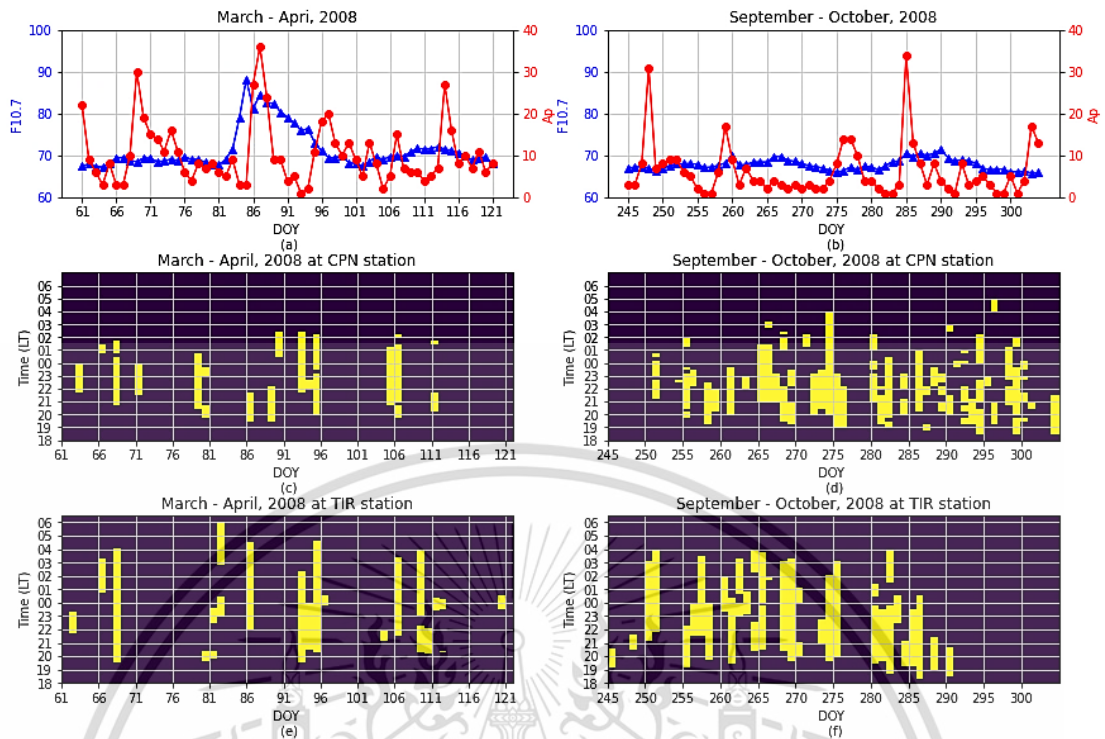


**Figure 4.4:** Day-to-day variability of the ESF occurrence in LSA at CPN and TIR stations.

In Figure 4.5, the day-to-day occurrence of the ESF at CPN and TIR stations is demonstrated during HSA. The data resolution has different interval times as 15 (CPN station) and 10 (TIR station) minutes, thereby, trends of the ESF are not affected in the analysis. The variations of the F10.7 and Ap indices have fluctuations in September and October more than March and April. The role of the high Ap index is seen with disappearance of the ESF at CPN station rather than at TIR station. The high F10.7 values seem to relate with reduction of the ESF events at both sites. We can also see the responses in monthly mean values of the Ap and F10.7 indices as summarized in Table 4. When we look at the ESF statistics in Figure 4.5(c) – (f), the quantity of the ESF in March and April is observed higher than in September and October over both CPN and TIR stations. This implies that the ESF occurs more often in months with small changes in solar and geomagnetic indices. The beginning time of the ESF starts around 19:00 LT and often lasts until the early morning at both sites, particularly in March and April. Furthermore, the longer durations of the ESF existence are clearly observed in 2014 at TIR station rather than at CPN station. This ESF feature is also seen in 2008 as shown in Figure 4.4(c) – (f). This might be dependent on the local conditions over longitudinal sites. It is clearly seen that the ESF events occur more frequently at TIR station than at CPN station, particularly, during March – April. Also, the post-midnight ESF events at both stations are consistent with their unique characteristics.

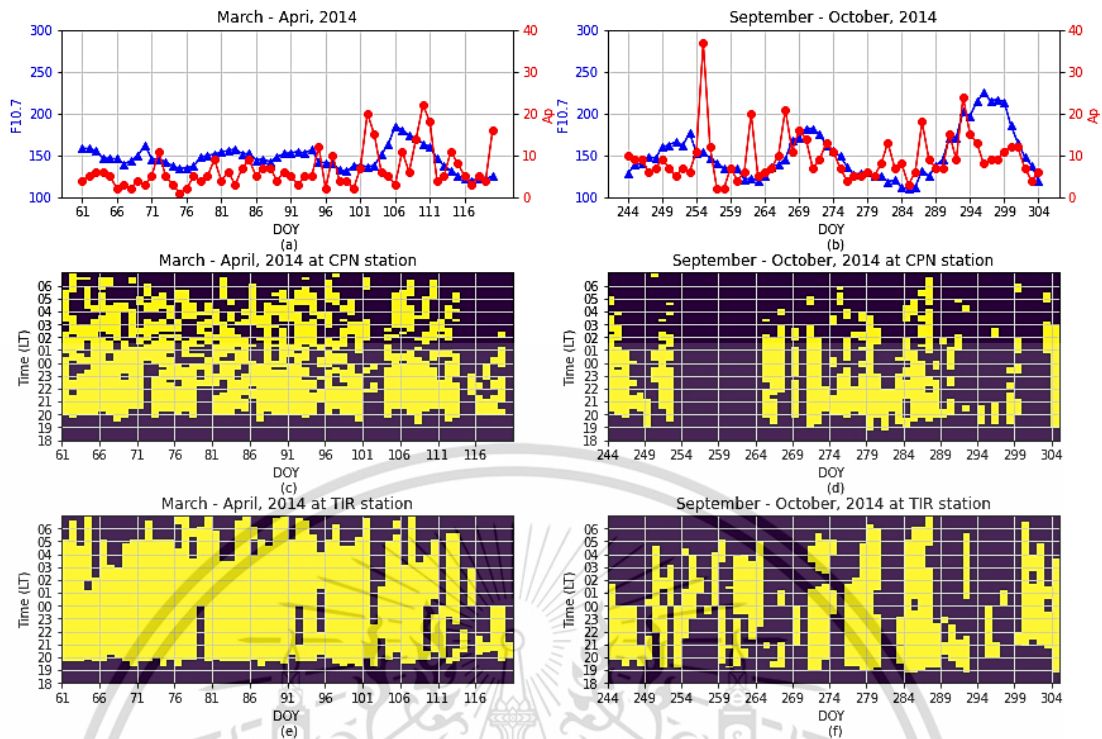


Figure 4.5: Same as above figure for HSA.

As the comparative analyses of the ESF characteristics in different years at CPN and TIR stations, even though these two stations are located nearby in the magnetic equator at  $3.0^{\circ}\text{N}$  for CPN station and  $0.32^{\circ}\text{N}$  for TIR station, the day-to-day variability of the ESF characteristics is different. Therefore, the possible causes are expected to depend on local features and conditions such as atmospheric gravity waves, perturbations of the F region, magnetic field changes, and plasma vertical drift velocity. These influencing factors can result in different generation of the ESF over these two stations. In addition, a clear dependence of the ESF occurrence on the F10.7 index is seen in this investigation for CPN and TIR stations. If we consider each day separately, the dependence of the ESF on the F10.7 index is hard to be concluded. In contrast, the high  $A_p$  indices are related to the reduction of the ESF occurrences. For instance, no or few ESF events are observed on the days with  $A_p$  value above 18. This implies that suppression of the ESF occurrences is caused by the geomagnetic storm [47], [48] and [83].

#### 4.1.2 Comparison of simultaneous ESF onsets at CPN station and TIR station

The ESF relationships between CPN and TIR stations are consistent as shown in their variation trends and forms. It is also well known that the ESF occurrences move eastward along longitudinal variations. This leads to estimating the ESF onsets at CPN station where is in the eastern part of the TIR station. The ESF onsets at CPN station can be possibly detected by observing the ESF onsets at TIR station. As shown in Figure 4.6(a) and (b), the statistics of the ESF onsets are demonstrated on given conditions as TIR- represents the observed ESF events at TIR station before This material is reserved for educational use only, not allowed for commercial use.

Forbidden to modify the content, and cite the document when use.

at CPN station and TIR+ means to the observed ESF events at TIR station after at CPN station. We observed about 40% to 75% of the observed ESF onsets at TIR station earlier than at CPN station in 2008 as shown in Figure 4.6(a). While the ESF onsets between 25% and 60% can be also detected at TIR station after at CPN station. On the other hand, the ESF onsets are observed at TIR station before at CPN station more than 72% in 2014 as shown in Figure 4.6(b). While the observed ESF onsets at TIR station after at CPN station are lower than 29%. Therefore, the results imply that estimation of the ESF onsets at CPN stations can rely on the observed ESF onsets at TIR station in HSA and LSA. It is noticed that the estimated ESF onsets in HSA achieve higher percentages than in LSA. This indicates that the high solar activity plays an important role in the estimation of the ESF onsets.

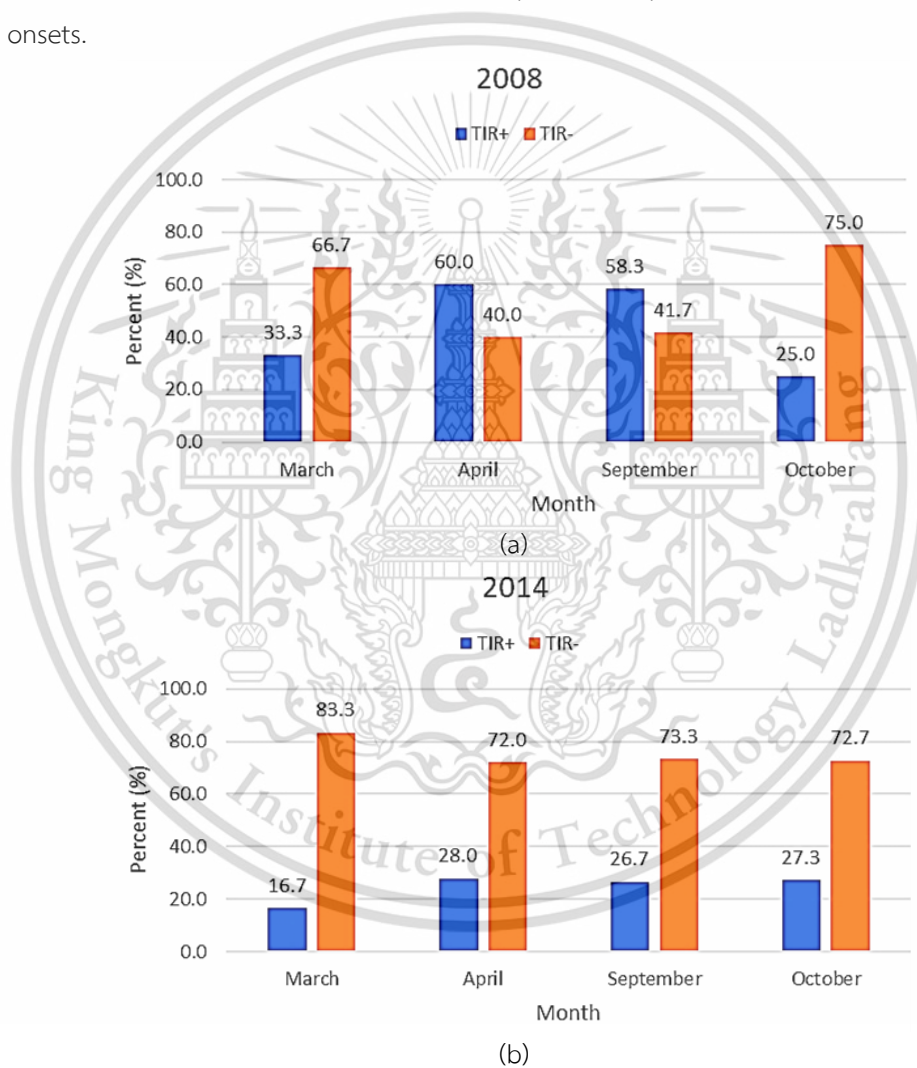


**Figure 4.6:** Statistics of the ESF onsets at CPN and TIR stations (TIR+ is meant that an ESF onset occurs at TIR station after at CPN station and TIR- represents otherwise). (a). 2008 and (b). 2014.

The prediction of the ESF onset is based on geometrical conditions of the ESF movements along the shifting path. This assumption can complete more than 40% and 72% accuracy in low and high solar activities, respectively. On the other hand, forecasting models are also presented in

This material is reserved for educational use only, not allowed for commercial use.

Forbidden to modify the content, and cite the document when use.

the next section using the deep learning networks at the CPN station for the ESF model. The designed models depend on depth of the input features and ESF relationships compared to the estimation technique in this section. Therefore, the robustness of the proposed model is presented in the next section.

### 4.1.3 Monthly occurrence rates and durations of the ESF events at CPN and TIR stations

As shown in Figure 4.7(a) and (b), the monthly occurrence rate and frequency of the ESF events in each month during LSA and HSA at CPN and TIR stations are demonstrated. The two top panels show the monthly percentage of the ESF occurrences against the local time (18:00 to 06:45) at CPN (blue rectangle) and TIR (red dot) stations. The two bottom panels represent the frequency of the ESF occurrence during post-sunset (18:00 to 23:45) and post-midnight (00:00 to 06:45) with respect to each ESF duration at CPN (orange dot) and TIR (black rectangle) stations. Note that the unit of “Frequency” means to the number of events in which ESF duration occurs.

See in Figure 4.7(a), the first top two panels demonstrate the monthly occurrence percentage of the ESF at CPN and TIR stations in each month in 2008. The variations of the ESF occurrence percentage have similar patterns at both stations as below 20% (30%) at CPN station (TIR station) in March and April, and high percentage in September and October (above 30%). Initialization of the ESF generation is also involved between these two stations as after 19:00 LT in March, April, and September, and after 18:30 LT in October. The post-sunset ESF occurrence rate rapidly increases in each month at both stations. This reveals that the post-sunset ESF generations are triggered under the same conditions such as the PRE, the  $E \times B$  drift velocity and the AGW [18], [84], [28], [29] and [85]. In addition, we distinguish those variations of the ESF occurrence after midnight gets gradual reduction at TIR station and sudden reduction at CPN station. Thereby, this might be caused by different local conditions as [7] and [86]. The post-midnight ESF occurrences are observed at TIR station longer than at CPN station in March and April, in contrast, the high ESF occurrence are seen at TIR station more than at CPN station in September and October. See the two bottom rows of panels in Figure 4.7(a), the frequencies of the ESF durations during post-sunset and post-midnight periods are demonstrated against the ESF durations in each month in LSA over both stations. During the post-sunset period, the observed ESF durations are around 0.25 - 3 hours (0.16 - 4.9 hours) in March and April at CPN station (TIR station), and 0.25 - 4.75 hours (0.5 - 5.5 hours) in September and October at CPN station (TIR station). We observe that the short durations of the ESF appear more frequently in September and October at CPN station than TIR station. Thus, the ESF developing process at CPN station is possibly disrupted by traveling ionospheric disturbance (TID) and medium scale ionospheric disturbance (MSID) leading to more frequencies of the short ESF existences [31] and [32]. During the post-midnight period, we observe 0.15 - 2.25 hours (0.15 - 4.75 hours) in March and April at CPN station (TIR station), and 0.25 - 3 hours (0.1 - 3 hours) at

This material is reserved for educational use only, not allowed for commercial use.

CPN station (TIR station). It is clearly seen that the longer ESF durations can be observed in each month at TIR station than at CPN station. The short ESF durations are more often seen at CPN station than at TIR station during post-sunset and post-midnight. Therefore, this different ESF characteristic is possibly caused by local conditions rather than global conditions. The observed ESF occurrences at CPN station are probably moved from the TIR station.

In Figure 4.7(b), it shows the similar results for HSA. For the monthly occurrence percentage of the ESF, The ESF occurrence percentage at TIR station is slightly higher than at CPN station. The highest percentage is observed 90% (98%) in March, 81% (88%) in April, 69% (71%) in October, and 43% (68%) in September over CPN station (TIR station). The ESF occurrence rate in March and April is higher than in September and October at two sites. The variations of the ESF occurrence rate at two stations follow the same pattern in each month. Also, the ESF occurrence period at CPN and TIR stations is equivalent. The rapid increase of the ESF occurrence rate is observed between 18:30 and 21:00 LT in each month at both stations. Later, the decreases of the ESF occurrence rate gradually vary until early morning. For the ESF durations, the distinct ESF durations between CPN and TIR stations are seen in each month, particularly during the post-midnight. The observed post-sunset ESF durations are about 0.25 – 4.75 hours (3.5 – 4.83 hours) in March, 0.25 – 4.75 hours (0.2 – 4.83 hours) in April, 0.25 – 5 hours (0.1 – 6 hours) in September, and 0.25 – 5.25 hours (0.2 – 6 hours) in October over CPN station (TIR station). The observed ESF durations during the post-midnight are approximately 0.25 – 4.75 hours (0.2 – 5.5 hours) in March, 0.25 – 2.75 hours (1.1 – 5.83 hours) in April, 0.25 – 2.75 hours (0.1 – 5.83 hours) in September, and 0.25 – 3 hours (1 – 5.83 hours) in October at CPN station (TIR station). The longest ESF durations are seen at TIR station more than CPN station, particularly during the post-midnight time. Therefore, the observed ESF at TIR station might shift to other regions, particularly at CPN station where is located along the shifting path.

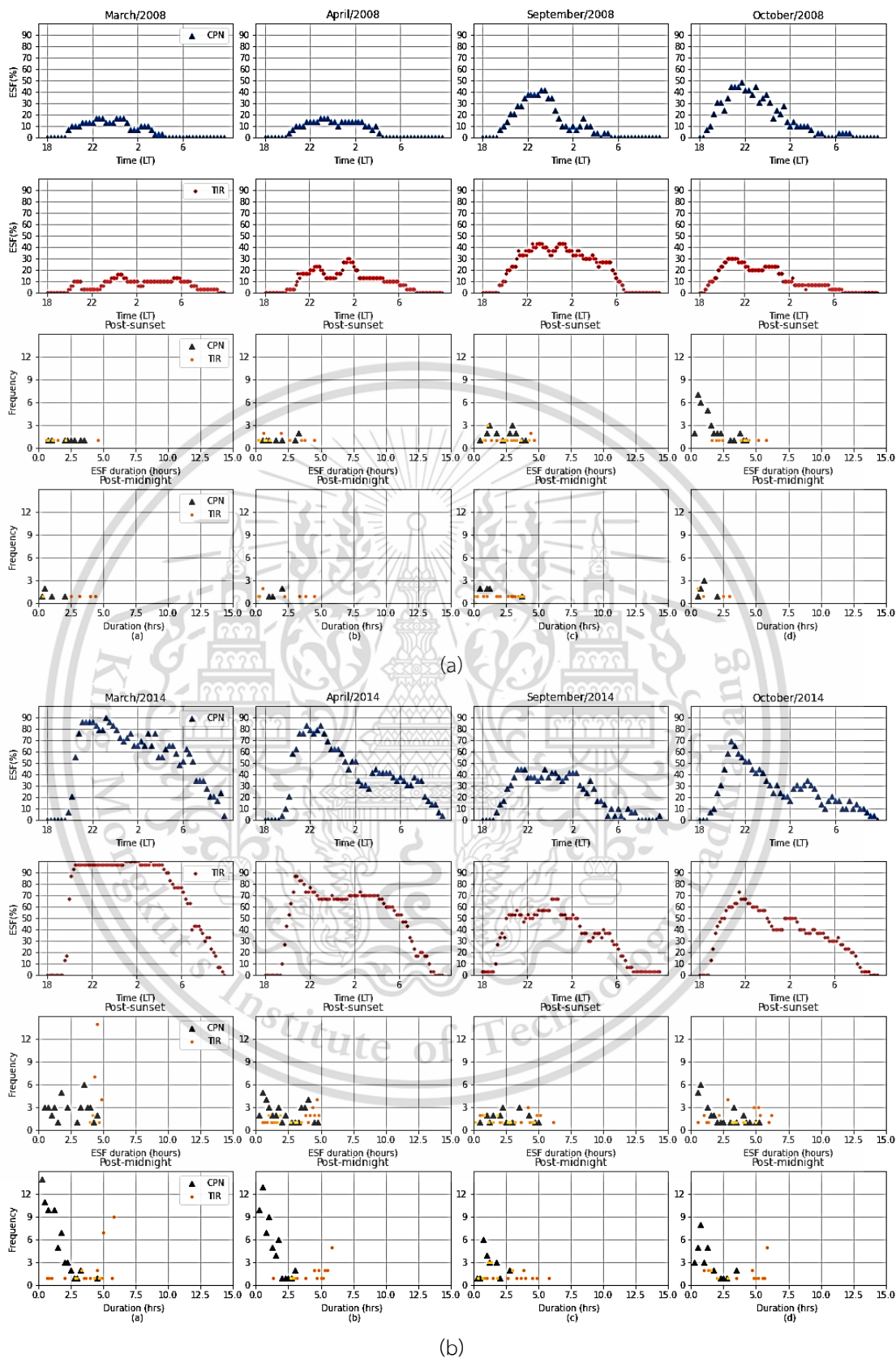


Figure 4.7: The monthly percent statistics and frequency of the ESF occurrences at CPN and TIR stations. (a) 2008 and (b) 2014.

This material is reserved for educational use only, not allowed for commercial use.

Forbidden to modify the content, and cite the document when use.

The comparative results between LSA and HSA exhibit that the characteristics of the ESF occurrence are dependent on solar activity in terms of the occurrence rate for both CPN and TIR stations. The highest ESF occurrence rate at both stations is observed in March and April for HSA and September and October for LSA. This implies that the seasonal variations of the ESF occurrence at both sites are likely influenced by solar activity. Additionally, this seasonal asymmetry of the ESF occurrence is likely controlled by magnetic change, local time, and solar wind. Some previous studies also investigated similar results [87], [45] and [88]. The significant characteristics of the ESF are distinguished as short durations with high frequency at CPN station and long durations with low frequency at TIR station. In some cases, we observed that the suppression of ESF events is likely caused by geomagnetic storm disturbance [47] and [48].

#### **4.1.4 Comparison of the ESF occurrence rate between observations and IRI 2016 model**

This part presents the comparative results of the ESF occurrence rate between observations and IRI 2016 model at CPN and TIR stations as shown in Figure 4.8(a) and (b). In Figure 4.8(a), the observed results are lower than the IRI 2016 model in each month for both CPN and TIR stations. The different percentage of the IRI 2016 against observations is about 34% (31%) in March, 15% (11%) in April, 18% (8%) in September, and 22% (27%) in October in 2008 (LSA) at CPN station (TIR station). The error of the IRI 2016 model is seen at CPN station higher than at TIR station, except in October. In HSA, the IRI 2016 model still provides high error of the ESF occurrence rate. Deviations of the IRI 2016 model with underestimation and overestimation are approximately 7% (25%) in March, 14% (24%) in April, 12% (3%) in September, and 11% (8%) in October at CPN station (TIR station). The overestimations by the IRI 2016 model are seen during LSA higher than HSA for both CPN and TIR stations, particularly in March and October. This error maybe due to the ESF characteristics rather than the fitting method used in developing the IRI 2016 from two ionosondes in Brazilian sector. The ESF characteristics are different over longitude sites as observed at CPN and TIR stations. Thus, the IRI 2016 model can be improved by adding these ESF datasets for both CPN and TIR stations.

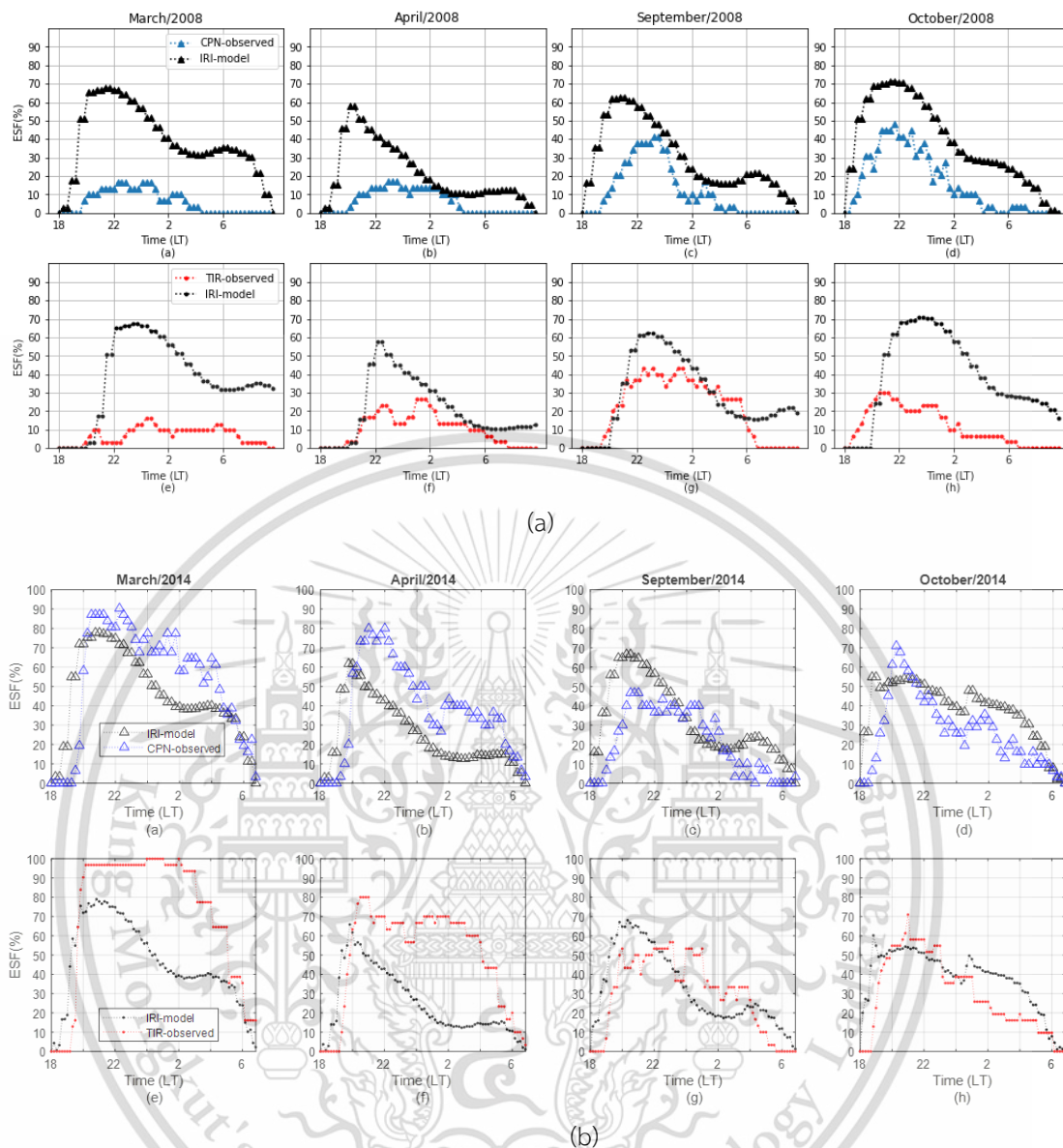


Figure 4.8: Comparative results of the ESF occurrence rate against with the IRI 2016 model at CPN and TIR stations. (a). 2008 and (b). 2014.

#### 4.2 The performance and results of the ESF forecasting models

In the previous section, the estimation of the ESF onset at CPN station is aided by observing the ESF onset at TIR station in the previous section. In this section, the estimation of the ESF is extensively developed using the deep learning networks. The performance of the ESF forecasting models is analyzed and exhibited for seeking the best ESF model. In experiments, it is noticed that the ANN models with three and four hidden layers have reductions in the performance. When we compare the ANN model with single and two hidden layers, found that two hidden layer ANN network provides sufficient and robust results against overfitting and underfitting while training. Thus, the ANN model with two hidden layers is only shown in this thesis. For the LSTM model, we

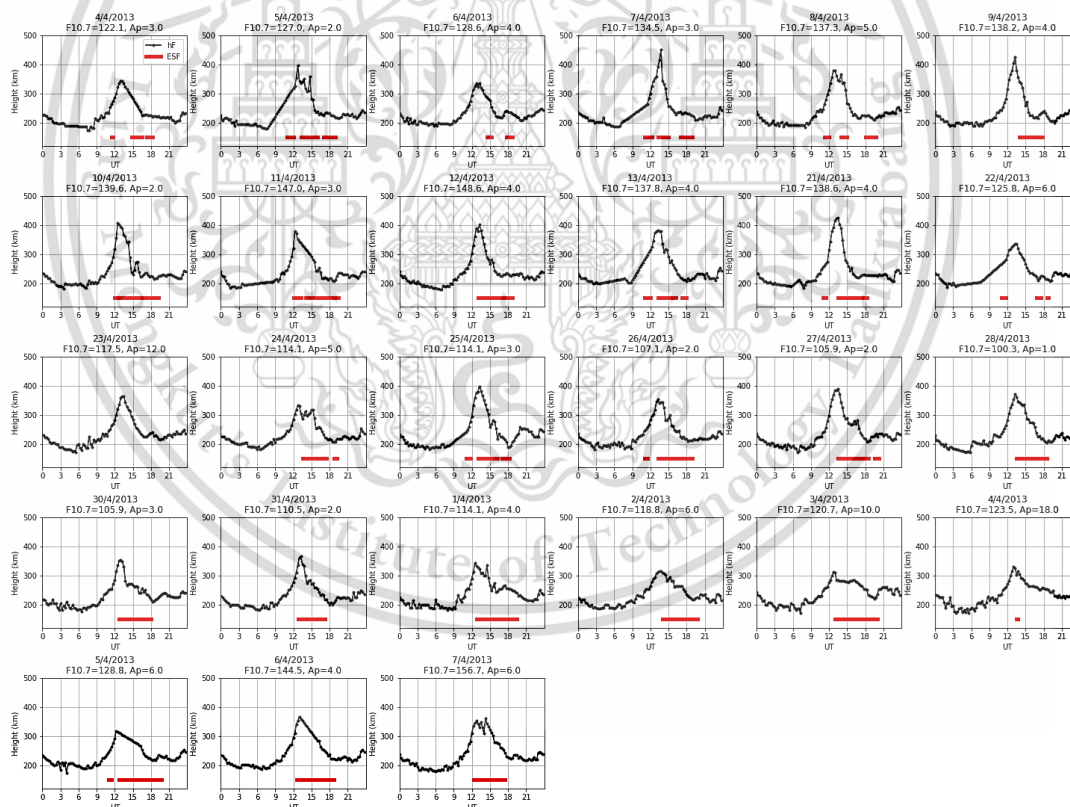
This material is reserved for educational use only, not allowed for commercial use.

Forbidden to modify the content, and cite the document when use.

only implement the experiment using a single hidden layer. As a result, the performance analysis and predicted results are respectively presented.

#### 4.2.1 Characteristics of the F layer height, vertical drift velocity, and ESF events

As shown in Figure 4.9(a) – (c), the h'F (black line with dots) and ESF (red graph) are plotted against the universal time (UT) in 2013, 2014, and 2016 at CPN station, respectively. The high solar activity years are seen in 2013 and 2014, and 2016 belongs to descending phase of the medium solar activity in the 24<sup>th</sup> solar cycle. The day-to-day variations in the h'F are in similar pattern for each year. The rapid increases and decreases in the h'F are observed every day after 09:00 UT. The peak h'F is seen around 12:00 to 15:00 UT in each day in 2013 and 2014. In 2016, we observed that the peak h'F is sometimes observed during post-sunset and post-midnight, which is different from those observations in 2013 and 2014. Overall, the ESF generations are clearly observed after the peak h'F in each day for all years. Therefore, the PRE in the h'F gives a necessary role for the ESF generation.



(a)

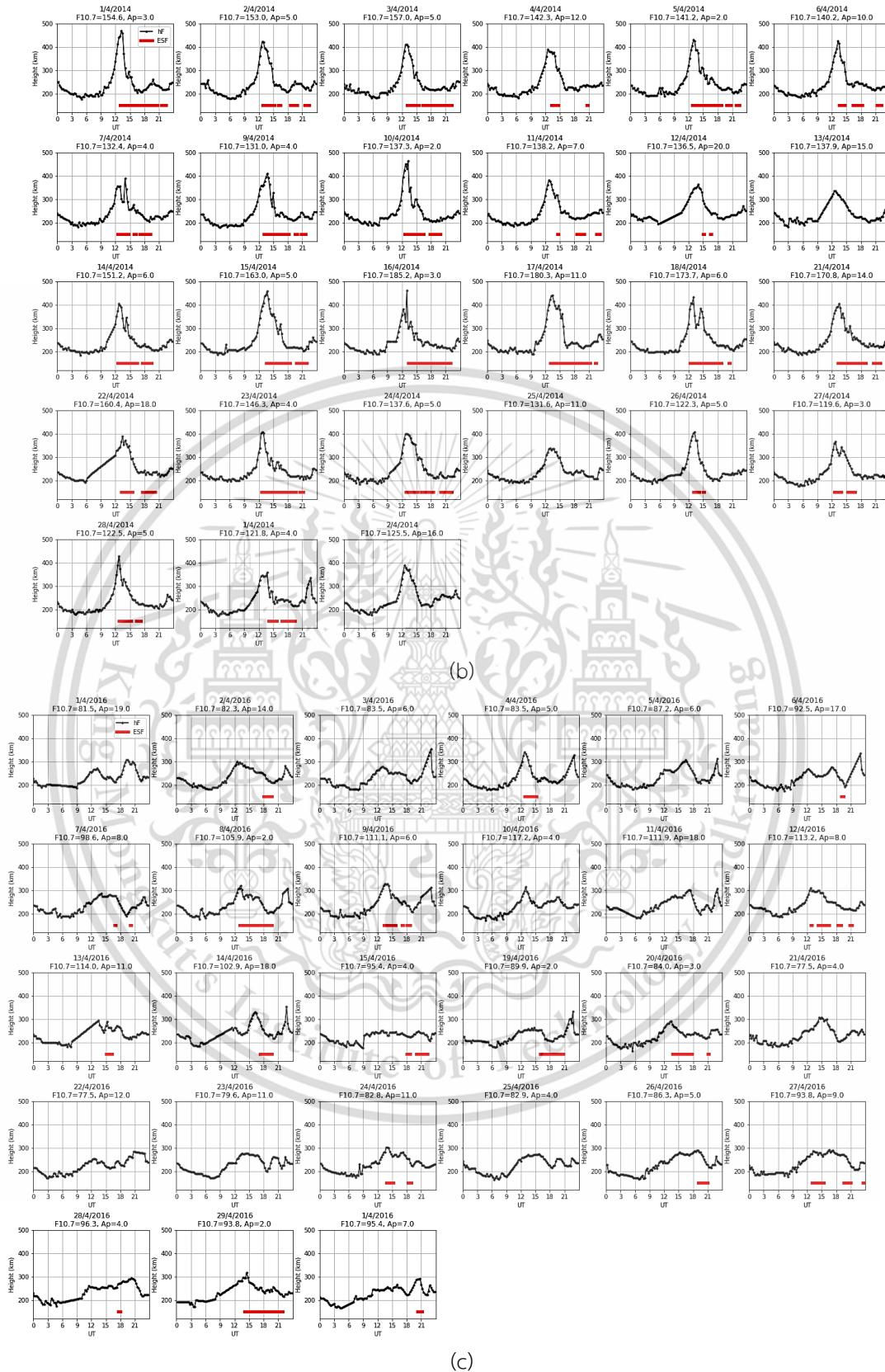
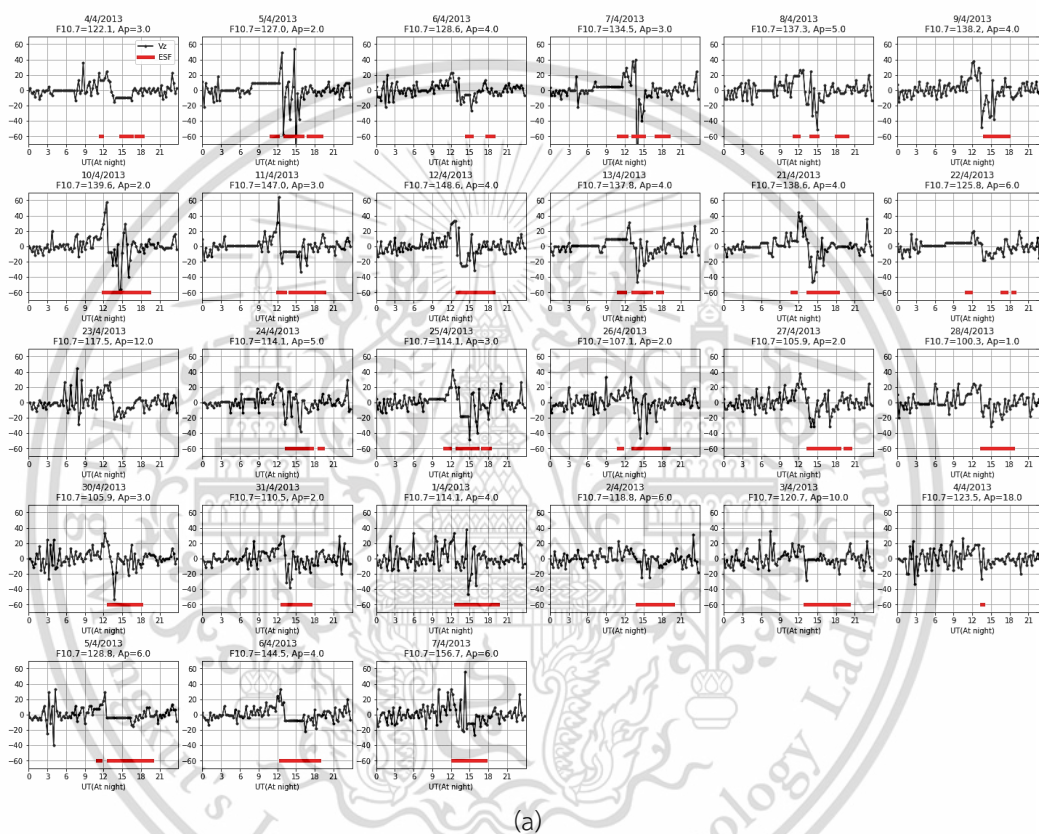


Figure 4.9: Day-to-day variability in the h'F and ESF occurrence in 2013, 2014, and 2016 at CPN station.

This material is reserved for educational use only, not allowed for commercial use.

Forbidden to modify the content, and cite the document when use.

As above, the changes of the h'F and the ESF occurrences are analyzed. In this part, the vertical drift velocity of the h'F and ESF are also shown against the time (UT) in 2013, 2014, and 2016 at CPN station as shown in Figure 4.10(a) – (c). Enhancements in the vertical drift velocity above 20 m/s during the post-sunset are clearly seen with the ESF generations in each day in 2013 and 2014, except in 2016 their characteristics are ambiguous and in different patterns. The peak values of the vertical drift velocity are observed during the post-sunset in 2013 and 2014, but in 2016, it does not follow the same patterns. Therefore, the generation of the ESF is likely to be triggered by other factors such as AGW, traveling ionospheric disturbance (TID), etc.



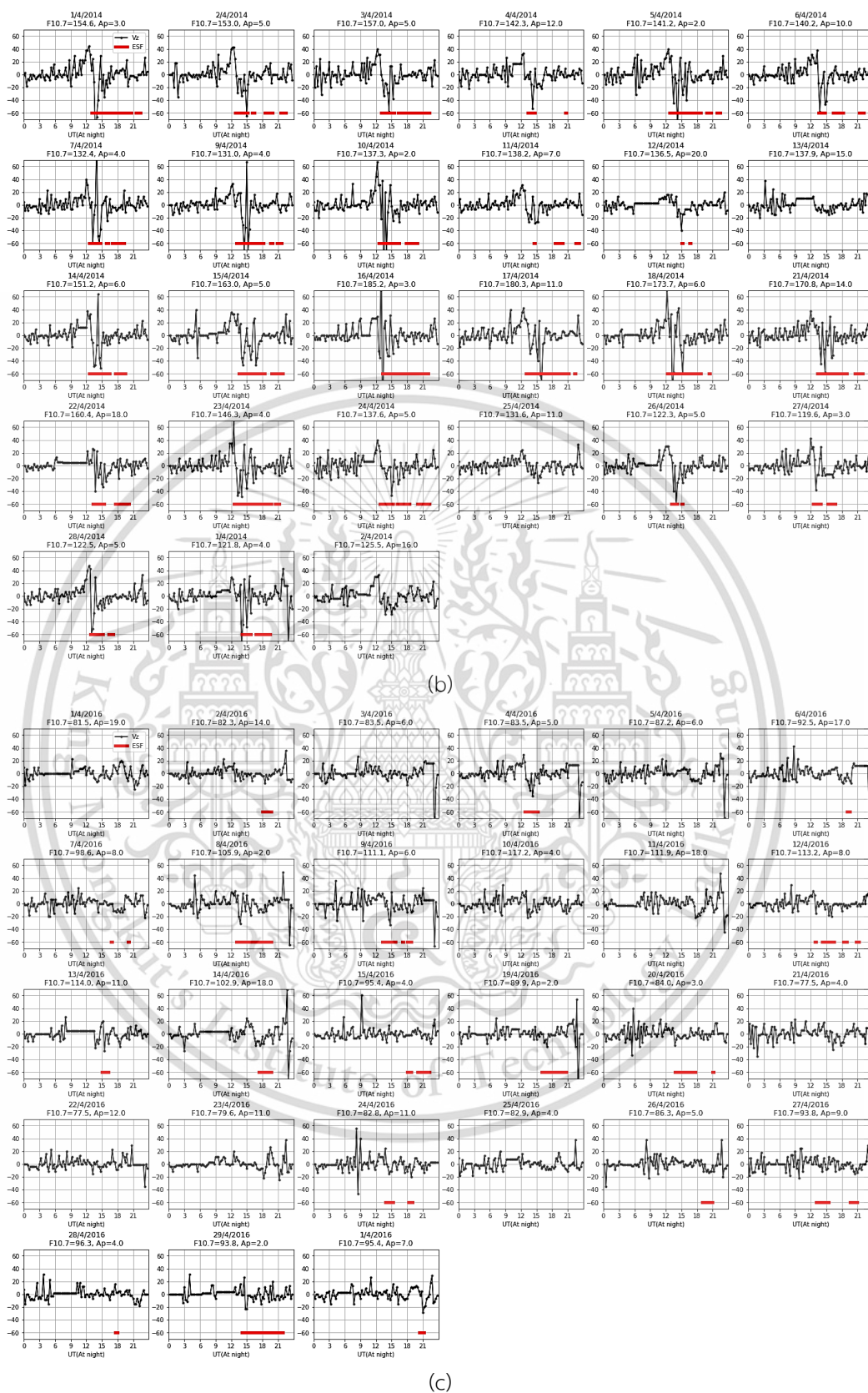


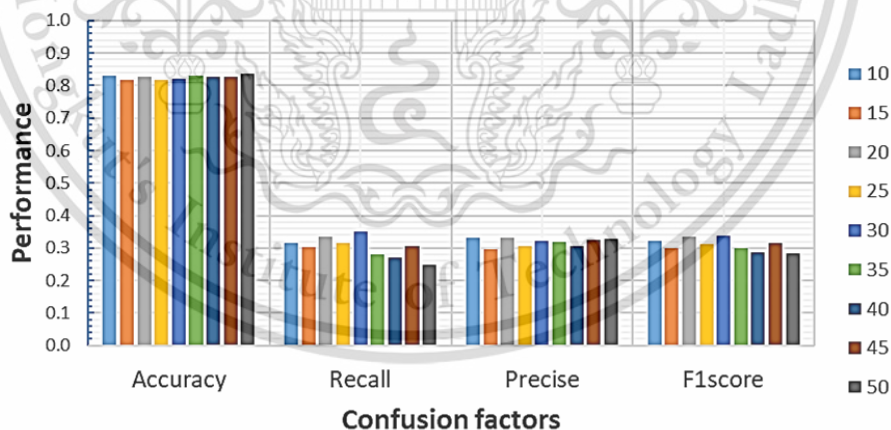
Figure 4.10: Day-to-day variability in the vertical drift velocity of the h'F and ESF occurrence in 2013, 2014, and 2016 at CPN station.

This material is reserved for educational use only, not allowed for commercial use.

Forbidden to modify the content, and cite the document when use.

#### 4.2.2 ESF model performance with different architecture designs

As shown in Figure 4.11(a) and (b), the indicators of confusion matrix are mainly used including accuracy, recall, precise and F1 score in interpreting the ESF models' performance. The input-based parameters are used including diurnal, seasonal, SSN, and ap3. for determining the network architecture. The values of those confusion parameters are gained by different neuron numbers from 10 to 50 for both the ANN and LSTM, respectively. The prediction accuracies are above 78% and slightly different with each neuron number for the ANN and LSTM models. The values of recall, precise, and F1 score are obtained below 39% for both ANN and LSTM models. Significantly, it is noticed that the ANN network with 30 neurons can achieve the acceptable performance and 35 neurons for the LSTM network. The LSTM network is obtained with higher performance than the ANN network. The enhanced neurons of the ANN network tend to meet with high false negative as seen in reduction of the recall. This also results in a reduction of the F1 score. In contrast, the reduction of the LSTM model performance is not significantly seen with orderly increased neurons. It is noticed that the LSTM model with 35 neurons receives a good performance in recall, precise, and F1 score. In addition, we find the loopback number for the LSTM model as shown in Figure 4.12. The enhancement of the loopbacks is observed with decreasing in the model's performance. This justifies the dependence of the ESF occurrence on short time, also implies that the LSTM learnability sufficiently depends on the prior information which is very close to the present time of the prediction. Thus, the optimal loopback is selected at 1 hour for the LSTM model.



(a)

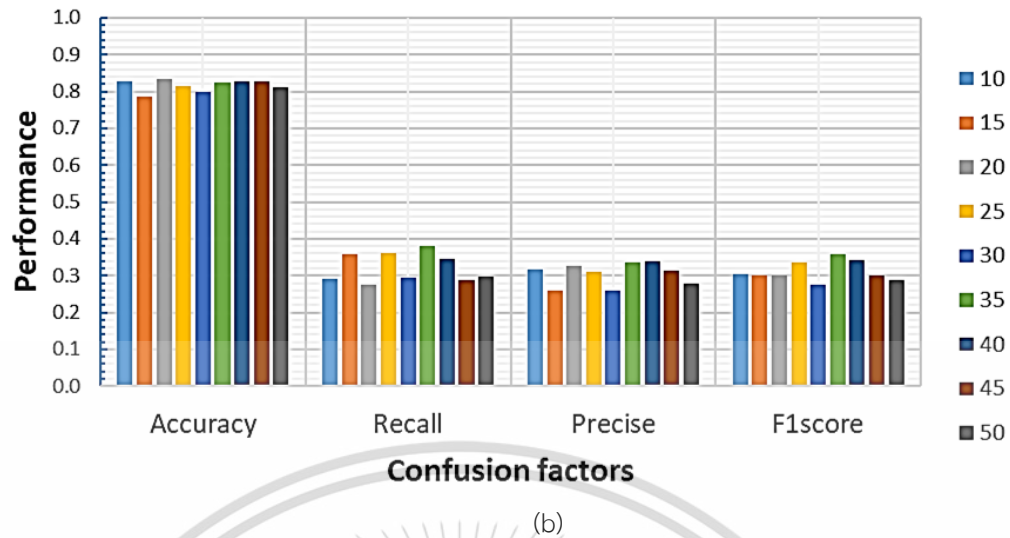


Figure 4.11: Results of determining the network architecture for (a) ANN and (b) LSTM.

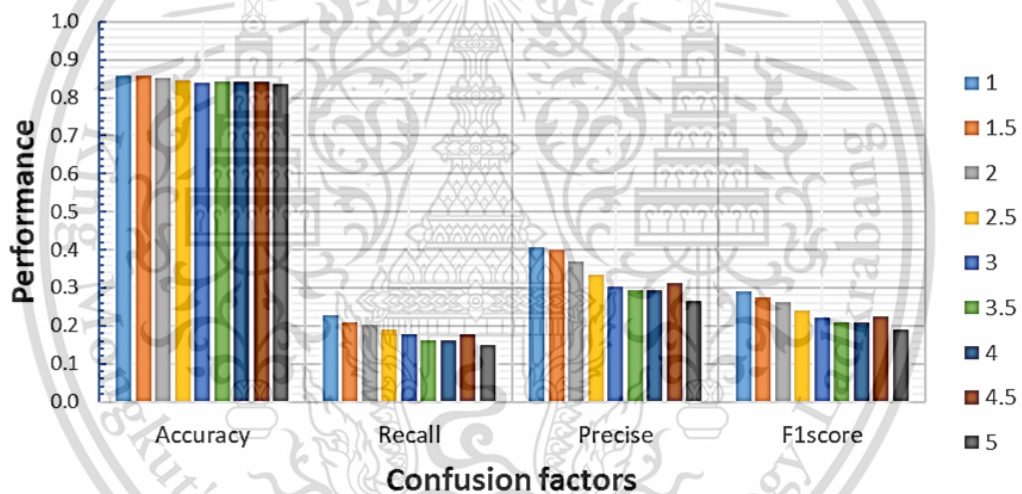


Figure 4.12: The performance of the LSTM with different loopbacks.

#### 4.2.3 ESF model performance with input combinations

This is one of the most significant parts of this work. First, investigation of the solar and magnetic indices is made as shown in Table 5 and Table 6. Selection of the solar and magnetic parameters is relied on confusion indicators. As a result, the ANN and LSTM models identically produce the best performance with SNN and ap3 indices as shown in the following tables. Use of these SSN and ap3 is seen to get the significant improvement in recall, precise, and F1 score. This implies that prediction of the ESF presence can be effectively continued using these indices. Anyway, if we look at the models' performance with other solar and magnetic indices, the performance is slightly lower and still acceptable. Therefore, the SSN and ap3 indices are mainly used to run the models in this work.

This material is reserved for educational use only, not allowed for commercial use.

Forbidden to modify the content, and cite the document when use.

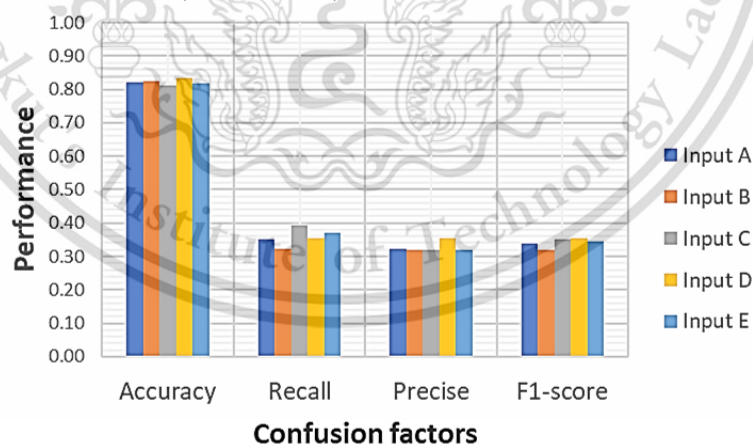
**Table 5:** Determination of the solar index as an input of the ESF model.

	Accuracy		Recall		Precise		F1 score	
	ANN	LSTM	ANN	LSTM	ANN	LSTM	ANN	LSTM
F10.7cm	0.82	0.83	0.13	0.22	0.20	0.29	0.16	0.25
SSN	0.81	0.83	0.30	0.24	0.29	0.32	0.30	0.28
F10.7 + SSN	0.84	0.83	0.10	0.20	0.25	0.28	0.15	0.23

**Table 6:** Determination of the Ap/ap3 and Kp/kp3 indices as an input of the ESF model.

	Accuracy		Recall		Precise		F1 score	
	ANN	LSTM	ANN	LSTM	ANN	LSTM	ANN	LSTM
ap3	0.83	0.84	0.32	0.29	0.33	0.34	0.32	0.31
kp3	0.84	0.83	0.22	0.26	0.33	0.30	0.26	0.28
Ap	0.84	0.83	0.23	0.26	0.34	0.31	0.28	0.28
Kp	0.84	0.83	0.23	0.26	0.34	0.31	0.28	0.28

As shown in Figure 4.13(a) and (b), the ANN and LSTM models' performance on each input combination is respectively demonstrated. The prediction accuracy is gained above 80% with each input combination for the ANN and LSTM models. The highest accuracy of the ANN and LSTM models is achieved with input D and E that comprise local Vd and AGW indices, respectively. As we can see in other confusion factors, utilization of the local parameters significantly produces reduction of the false ESF absence prediction with input C to E (input B to D) and increase of the ESF presence prediction with input C to E (input B to E) for the ANN model (LSTM model).



(a)

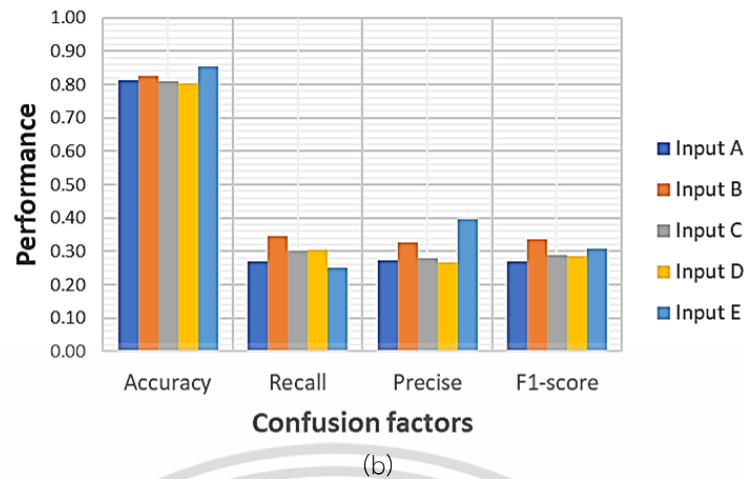


Figure 4.13: The ESF models' performance with each input combination for (a) ANN and (b) LSTM.

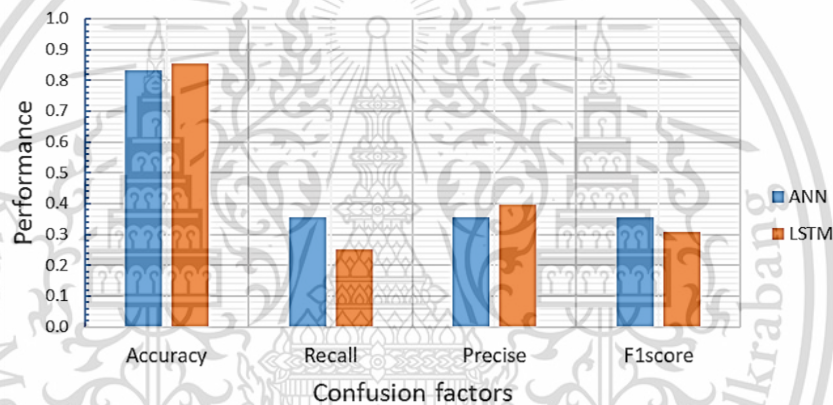


Figure 4.14: The best performance of the ANN and LSTM models with the input D and E, respectively.

#### 4.2.4 Comparison between observations against ANN, LSTM, and IRI 2016 models

Comparative results between observations against ANN, LSTM and IRI 2016 models in 2019 are demonstrated in Figure 4.15. The black line with asterisks represents the observed ESF values. The predicted values of the ANN, LSTM, and IRI 2016 models are respectively shown by the red line with circles, blue line with triangles, and green line with squares. The y-axis and x-axis represent the monthly probability of the ESF occurrence and local time (17:00 to 06:45 LT). The result of the LSTM model is obtained using the input E and the ANN model is derived using the input D. This result exhibits the ESF characteristics and validation of the ESF models in descending phase of the minimum solar activity. As a result, the monthly percentage of ESF occurrence is observed below 60%. The observed high occurrence rate is in February, March, August, April, September, and October, respectively. The deviation of the models' prediction is found in each month. More details are discussed as follows.

This material is reserved for educational use only, not allowed for commercial use.

Forbidden to modify the content, and cite the document when use.

As the three models' prediction, the ANN model overestimates the monthly probability of the ESF occurrence in March, April, and October, otherwise, underestimates the monthly probability in February, August, and September as shown in Figure 4.15. The ANN model produces high overestimation between 20:00 LT and 03:00 LT in March, April, September, and October. Also, the underestimated ESF probability of the ANN model is seen between 18:00 LT and 19:30 LT in all months. The ANN model produces underestimated values during 18:00 LT to 06:45 LT in February and August more than in September and October. The deviation of the ANN model varies around 10% and 40% in terms of the RMSE as shown in Figure 4.16. For the LSTM model, the case of the underestimates is observed more than the overestimates, i.e., the underestimated values are in February, August, and September, while overestimating is in April and October. The RMSE of the LSTM model is in the range between 10% and 21% as shown in Figure 4.16. In the IRI 2016 model, the predicted results tend to be overestimated in all months. The overestimated values of the IRI 2016 model are seen from 18:30 LT to 06:30 LT in all months. The difference of the IRI 2016 model is around 19% and 37% in terms of the RMSE.

Therefore, evaluation of these three models shows that the LSTM model provides lower deviation percentage than the ANN and IRI 2016 models for forecasting the ESF monthly probability. This clearly exhibits the capability of the LSTM model in handling complex input features against the ESF occurrence. As shown in Figure 4.9 and Figure 4.10, the variations of the h<sup>2</sup>F and its drift velocity are not directly related with the developing and developed ESF occurrences. Therefore, the multiple learning loopbacks and neural design of the LSTM model work sufficiently on this issue, while the ANN model depends on a single component in learning time step and non-linear function of the neuron. In terms of the IRI 2016 model, it is dependent on B-spline method using the ESF data from two stations in Brazilian sector, thus, deployment of the IRI 2016 model at CPN station is insufficient due to the independent characteristics of the ESF occurrence and the inflexibility of the B-spline method. For example, the study of the ESF characteristics over longitudinally separated stations at CPN and TIR stations where are close together, which also reveals that variations of the ESF occurrences are not the same. This implies that the ESF event is a unique and locally dependent phenomenon.

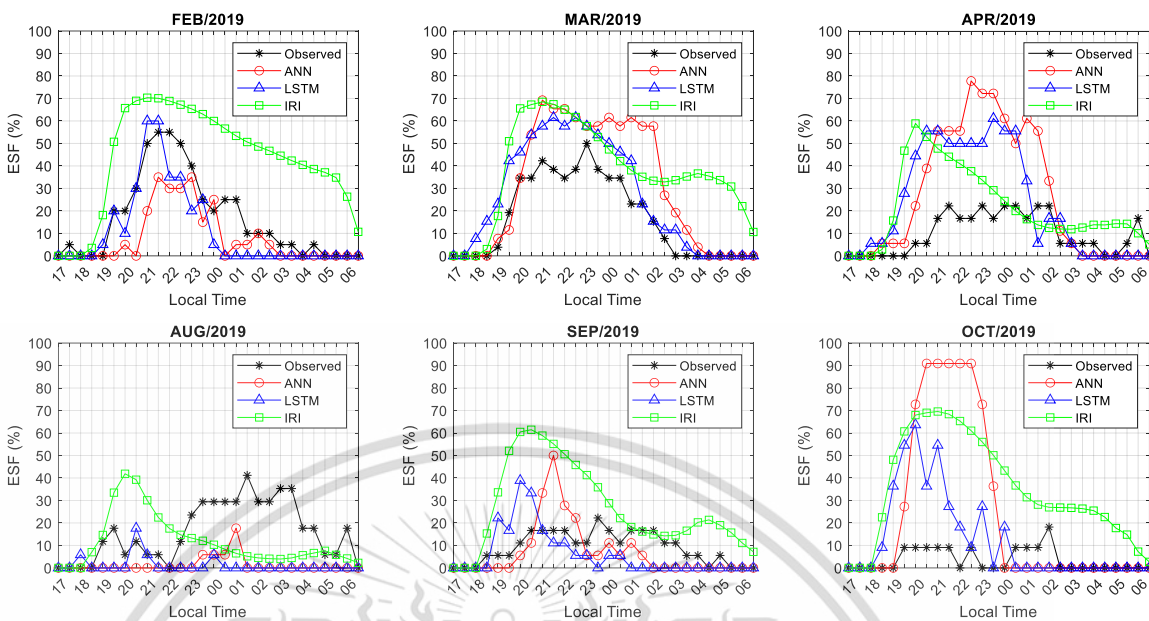


Figure 4.15: Comparison of the ESF occurrence percentage between observations, ANN, LSTM, and IRI 2016 model at CPN station.

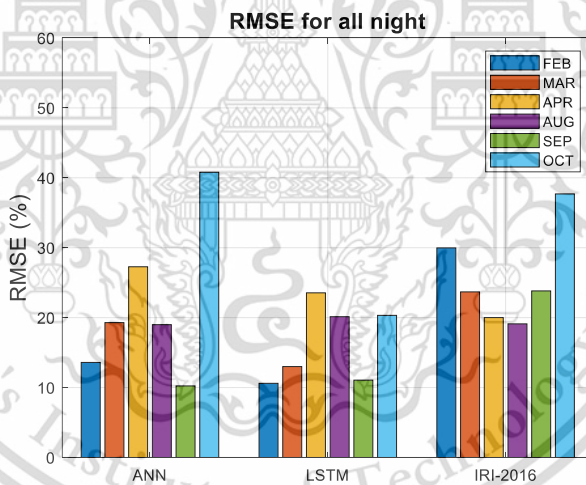


Figure 4.16: Comparison of each model against the observed ESF values.

As shown in Table 7, the results of the ESF model are separately analyzed for three predictive aspects such as post-sunset, post-midnight, and all night. Also, the RMSE of the proposed ESF model trained with and without the AGW parameter for reflecting the beneficial utilization of the local parameters. As a result, utilization of the AGW parameter can improve the ESF model in the post-midnight for March, April, August, September, and October. This result justifies the good relationship between the AGW parameter and post-midnight irregularities [7]. In addition, the LSTM model can get significant improvements in September for all cases, that is, the AGW parameter gives significant information to the ESF model in September. On the other hand, the ESF model cannot be optimized with the AGW parameter during the post-sunset. Furthermore, the ESF model

This material is reserved for educational use only, not allowed for commercial use.

without the GW index works effectively for both all nights and post-sunset predictions. The utilization of the GW index gives the significant improvement on the post-midnight prediction.

**Table 7:** The LSTM model's performance with and without the AGW index.

	<b>All nights</b>		<b>Post-sunset</b>		<b>Post-midnight</b>	
	<b>GW</b>	<b>No GW</b>	<b>GW</b>	<b>No GW</b>	<b>GW</b>	<b>No GW</b>
<b>Feb</b>	15.9	10.6	19.0	9.6	12.0	11.5
<b>Mar</b>	14.3	13.0	19.4	16.5	5.7	8.0
<b>Apr</b>	32.8	23.5	44.5	29.5	12.9	15.4
<b>Aug</b>	20.4	20.1	14.0	12.4	25.2	25.6
<b>Sep</b>	7.4	11.1	6.5	12.2	8.3	9.7
<b>Oct</b>	27.2	20.3	37.7	27.6	7.3	8.1

#### 4.2.5 Prediction results of the ESF daily occurrence rate

Prediction results of the daily ESF percentage and occurrence are demonstrated in this part as shown in Figure 4.17 and Figure 4.18. The daily ESF percentage is computed by summing up the ESF presences from 17:00 LT to 06:45 LT and dividing by the total number of the ESF presence and absence. The y-axis represents residual errors between the observed values and the ESF model. The x-axis represents the day number in March and September equinoxes with 110 available days as February (1 - 20), March (21 - 46), April (47 - 64), August (65 - 81), September (82 - 99), and October (100 - 110). The errors of the ANN and LSTM models are slightly different with each day. The total error of the ANN model is 23.19. In contrast, the LSTM model gains 21.38 of the RMSE. The error of both models is seen above 20% on days from March to August (35 - 77). The ANN model provides higher errors than the LSTM model in October. Therefore, the LSTM model outperforms the ANN with 1.81 of the RMSE. This achievement might be caused by the advantages of new local input features and the LSTM neural design. Moreover, it is realized that the daily prediction of the ESF phenomenon is still difficult because of the complexities of the ESF characteristic variations against input features and imbalanced data classes. It is further justified that the significant role of local input features and the advanced LSTM model are suitable for the ESF forecasting development.

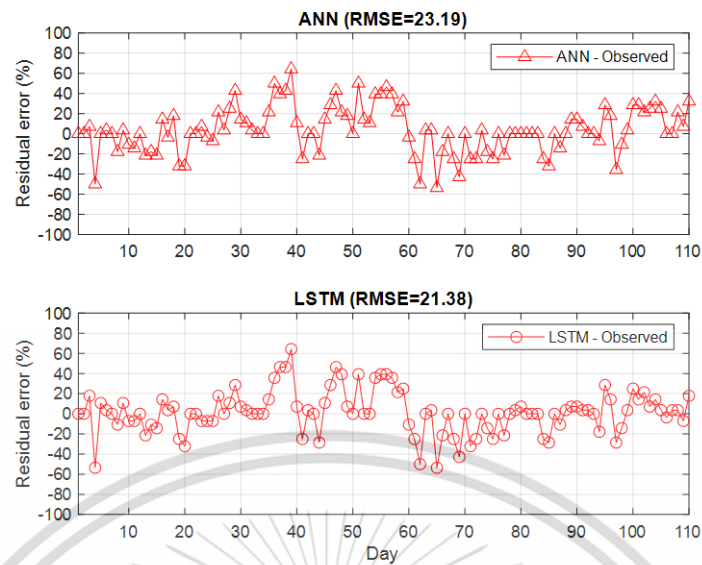


Figure 4.17: The residual errors between the observations and the ESF models for the daily ESF percentage.

ANN				LSTM					
		ESF-0	ESF-1	Total			ESF-0	ESF-1	Total
Observed	ESF-0	27	10	37	Observed	ESF-0	35	15	50
	ESF-1	36	37	73		ESF-1	28	32	60
	Total	63	47	64		Total	63	47	67

(a) (b)

Figure 4.18: The performance of the ANN and LSTM models for the ESF daily prediction.

As shown in Figure 4.18(a) and (b), the prediction results of the daily ESF occurrence from the ANN and LSTM models are exhibited using the confusion matrix. The ESF day (ESF-1) is defined when ESF is observed or daily ESF percentage is greater than zero and otherwise, it is defined as non ESF day (ESF-0). As a result, the accuracy of the ANN and LSTM models is about 57% (64) and 61% (67), respectively. The correct prediction of the ESF day of the ANN and LSTM models is obtained about 53% (47) and 68% (47). It is noticed that the ANN model works effectively for this case. This causes the overestimation of the ESF occurrence in monthly probability analysis. In case of correct prediction of non ESF day, the ANN model gets 60% (63) and the LSTM model gets 56% (63). In overall, the performance of the ANN and LSTM models can achieve more than 50% accuracy for the daily ESF prediction.

#### 4.2.6 Prediction of the short-time occurrences of the ESF events

In this section, the prediction results of the ANN and LSTM models with one step prediction ahead are analyzed as shown in Figure 4.19(a) and (b), respectively. The accurate prediction of the ANN and LSTM models can achieve about 83.3% (2566) and 85.4% (2627). In terms of correct prediction, the class ESF-0 gains higher number than the class ESF-1 as seen in the green box. This

This material is reserved for educational use only, not allowed for commercial use.

Forbidden to modify the content, and cite the document when use.

is caused by the data sample in the class ESF-0 is more than the class ESF-1 as shown in Table 3. This imbalanced data portion can cause the ANN and LSTM models' training in adjusting the networks' hyperparameters for the class ESF-0 more than the class ESF-1. Thus, the ANN and LSTM models yield a high prediction score to the ESF-0 class rather than the ESF-1 class. However, imbalanced data is a normal case on realistic problems. For this case, the balancing techniques are not appropriate for this issue due to the diurnal and seasonal dependencies of the ESF data. The ANN and LSTM model can respectively provide 90.4% (2682) and 89.5% (2825) of the correct prediction of the ESF-0. The ANN model is more effective with the ESF-0 prediction. This leads to reduction of the ANN model capability for the ESF-1 prediction. For the ESF-1 prediction, they achieve 35.5% (397) and 39.7% (252). It is noticed that the LSTM model works sufficiently on the prediction of the ESF-1 compared to the ANN model. In addition, we observe that the LSTM model can reduce the false positive or false prediction of the ESF-1. The difficulties and complexities in predicting the ESF-1 are still seen for the short-time ESF prediction. The major causes behind these challenging problems are likely relied on several local factors and dimensions such as indescribable relationships between the ESF occurrence and input parameters are unclear for short-term variability [55], loss of the significant information due to restriction of the available data, disadvantages of the global parameters against physical mechanisms of the ESF characteristic variations, and the recognizability of the models is affected by the data portion. In this thesis, we can find that the local F layer parameters play an important role on the ESF forecasting models and, the advanced LSTM model is one of the effective methods to this issue.

		ANN					LSTM		
		ESF-0	ESF-1	Total			ESF-0	ESF-1	Total
Observed	ESF-0	2425	256	2681	Observed	ESF-0	2527	152	2679
	ESF-1	257	141	398		ESF-1	298	100	398
	Total	2682	397	2566		Total	2825	252	2627

(a) (b)

Figure 4.19: The performance of the ANN and LSTM models on the ESF short-time prediction.

#### 4.2.7 Performance of the ESF model on ahead predictability analysis

This part is an extensive analysis of the LSTM model's performance based on one-hour loopback learning for the multiple prediction steps ahead as shown in Figure 4.20. The performance of the LSTM model is exhibited using accuracy, recall, precise, and F1 score of the confusion matrix. The LSTM model is tested to make ahead prediction from 1 – 24 hours, respectively. As a result, the LSTM model can give more than 78% accuracy for all prediction steps. The performance of predicting the ESF-1 is gained above 31% with 1 hour up to 12 hours prediction steps ahead as seen in F1 score. The LSTM model performance is reduced with increased prediction steps above 13 hours. Also, we notice the enhancement of both false positive and false negative as seen in

This material is reserved for educational use only, not allowed for commercial use.

recall and precise scores. Consequently, enhancement of the prediction step of the LSTM model is limited by the relationship between the inputs and ESF variations. To enhance and improve the prediction steps ahead of the ESF model, the input design must be further considered in the time lag dependence.

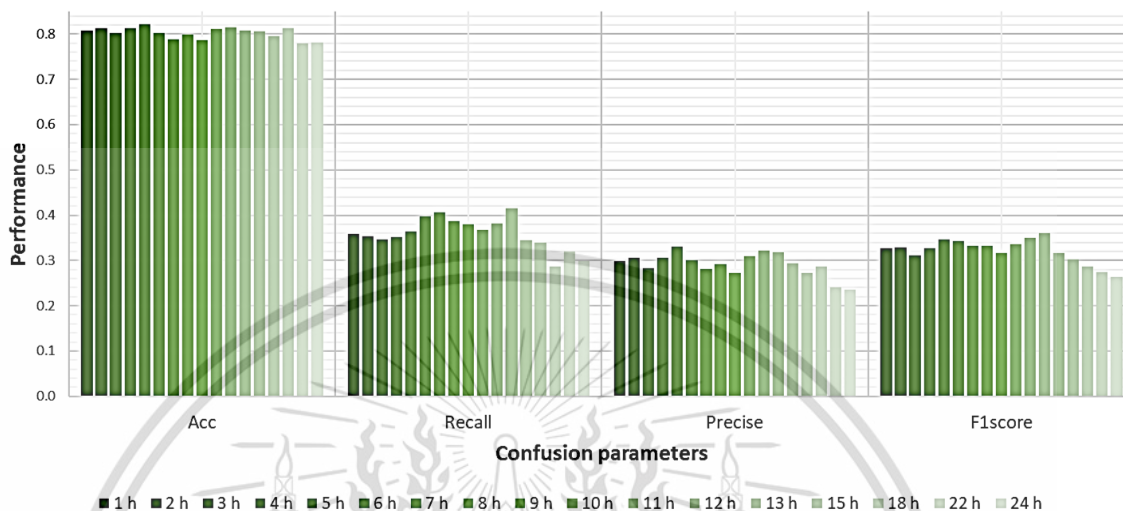


**Figure 4.20:** The performance of the LSTM model on 1h to 24h prediction ahead.

The ESF predictive model is a crucial warning system for communication systems. This accomplishment can indicate that the prediction of the ESF in three scenarios such as short time, daily, and monthly predictions. For the daily prediction, the proposed LSTM model can fulfil less than 61% accuracy. The daily prediction of the ESF events is difficult due to the characteristics of the inputs and the ESF over time series are grouped to represent the daily event instead. Thus, this can increase the complicated features of the input and output relationships. For example, it might be possible to represent the ESF events using a single value of the F-layer height. As we can see, the generation and development of the ESF events are dependent on different heights. In addition, this is one of the unsolved problems of the ESF in day-to-day variability. The predictive model is highly possible to get the insufficiency on its prediction. For short time predictions, the proposed LSTM model can accomplish ~85% accuracy. This derived accuracy is consistent with inputs and ESF relationships. Based on a variety of previous studies the generation and development of the ESF events can be characterized against F-layer height and its drift velocity, and other sources as a function of time. This can lead to the enhancement of the predictive model capability. For monthly predictions of the ESF, this is extensive analysis of the short time predictive model. It is proven depending on the ESF variations which can be characterized as well as diurnal variations. Therefore, the proposed model can produce the best fits of the ESF monthly percentage. The utilization of the proposed model on these three scenarios can achieve more than 50% accuracy.

Furthermore, it is realized that the proposed model is suitable for the short time and monthly predictions rather than the daily predictions in applications. While using the proposed model, it would be suggested that the new local input parameters are crucial to the predictability of the model. We can notice in results of the input analyses that the local vertical drift velocity and gravity waves enhance the proposed model's performance. In particular, the proposed model attains low deviation during post-midnight when it is trained with the GW index. Consequently, consideration of these local indicators is very useful together with the model's predictability and reliability because they are represented as triggering and influencing proxies of the ESF generation and development.



## Chapter 5 Conclusions

In this thesis, we have completed two major studies of the ESF which are summarized as follows. The comparison of the ESF occurrence at CPN and TIR stations has successfully completed in this thesis. It is found that the patterns of the ESF variations at both CPN and TIR stations are similar. Furthermore, the ESF occurrences at both stations depend on the solar activity as the occurrence rate of ESF in HSA is higher than LSA. The high percentage of the ESF occurrences is asymmetric between LSA and HSA. The high ESF occurrence is seen in September and October in LSA and March and April in HSA. In addition, the occurrence rate, and durations of the ESF at both stations are different even though their latitudinal locations are close. The high percentage and long duration of the ESF occurrence are seen during post-midnight at TIR station more than CPN station. It is also clearly seen that the ESF characteristics at CPN station have short durations with frequent numbers. This implies that the different characteristics of the ESF events over CPN and TIR stations in 2008 (LSA) and 2014 (HSA) likely depend on the local conditions. For estimation of the ESF event at CPN station, the estimation performance can achieve above 70% success of estimating the ESF onset at CPN station by observing the ESF onsets at TIR station for HSA, in contrast, it is obtained above 40% in LSA. Comparison of the observations with the IRI 2016 model exhibits high errors at both CPN and TIR stations. The IRI 2016 model provides the overestimates of the ESF occurrence percentage at both sites in LSA. The high overestimation of the IRI 2016 model is also observed in March and April in HSA over two stations. Therefore, the result analysis can unveil that the estimation of the IRI 2016 model could not effectively cover widespread areas. These results and datasets are useful and crucial to the IRI 2016 model improvement. Lastly, understanding of the ESF day-to-day variability is still a significant mystery for both global and local scales.

Development of the ESF forecasting models has been completed using the ANN and LSTM models at CPN station. The LSTM model can perform with 85.4% accuracy, while the ANN model gains 83.3% accuracy for the short-term ESF prediction. The optimal model is gained for the ESF forecasting model by using the LSTM network trained with the Vd and AGW parameters. Investigations of the input parameters can reveal that the global solar and magnetic indices are crucial for developing the ESF forecasting model. Utilization of the local F layer parameters together with the global indices can contribute to the improvement of the ESF model. For instance, the ESF model can gain improvements during the post-midnight rather than during the post-sunset when the Vd and the AGW are used. For prediction of the ESF monthly percentage, the LSTM model can outperform the ANN and IRI 2016 models for months. In the analysis of the ESF daily occurrence prediction, the ANN and LSTM models can complete about 55% accuracy. The LSTM model produces lower overestimation than the ANN model. When comparing three models with observed

This material is reserved for educational use only, not allowed for commercial use.

Forbidden to modify the content, and cite the document when use.

ESF monthly percentages, we notice that the LSTM model yields the RMSE below 20%, while the IRI 2016 model produces more than 20% of the RMSE for each month. As analysis of three aspects of the results, prediction of the ESF presence is still a difficult task as well as daily ESF occurrence. As demonstrated in recall, precise, and F1 score factors, scores of these factors are gained around 0.3 or 30% indicating the difficulties of predicting the ESF presence. The main issues can be judged depending on several factors such as complexities of the ESF day-to-day variability against the input parameters are still unclear and fully understood, weak points of the global solar and magnetic indices in explaining the physical mechanisms of the ESF events, and imbalanced data classes can partially cause the ESF model's overlearning. Therefore, some solutions to this issue are possibly to investigate the new global and local input features and apply the hybrid-techniques in the AI. A large dataset is still needed to train the LSTM model for enhancing the ESF model's reliability and validity. Furthermore, uncovering the mystery of the ESF events is a significant key to achieving the accurate ESF forecasting model.

The deployment of this ESF model can distribute the alert signal of the ESF events in the next 1 to 13 hours in advance to the users. Thus, this alert signal or message is useful to avoid or reduce the effects of the ESF events on the users' communication systems and tools. The users can furthermore obtain the monthly percentage of the ESF events from the model for planning the sufficient communication systems. The application of the ESF model is acceptable in our local region. The global applications of this ESF model should be concerned with the training dataset obtained from the CPN station, which is not able to give the precise results for other regions. The training dataset covers all equinoctial months from 2008 to 2018 of the 24<sup>th</sup> solar cycle. The boundary of utilizing the proposed ESF model is suited and suggested on operating on the solar activity related to the solar 24<sup>th</sup> cycle. Therefore, the utilization of the ESF model should be considered and deployed in equivalent range of the solar levels based on this 24<sup>th</sup> solar cycle for obtaining the sufficient performance. However, the users must be aware of remaining gaps in using this ESF model. As mentioned above, the understanding of local F-layer features is still important together with the ESF model's prediction. These two factors can give reliability and sufficient application to the users.

## REFERENCES

- [1] R. Woodman and C. La Hoz, "Radar observations of F region equatorial irregularities," *Journal of Geophysical Research*, vol. 81, no. 31, pp. 5447-5466, 1976.
- [2] H. Booker and H. Wells, "Scattering of radio waves by the F-region of the ionosphere," *Terrestrial Magnetism and Atmospheric Electricity*, vol. 43, no. 3, pp. 249-256, 1938.
- [3] P. Sultan, "Linear theory and modeling of the Rayleigh-Taylor instability leading to the occurrence of equatorial spread F," *Journal of Geophysical Research*, vol. 101, no. A12, pp. 26875-26891, 1996.
- [4] R. Woodman, "Spread F - an old equatorial aeronomy problem finally resolved?," *Annales Geophysicae*, vol. 27, no. 5, pp. 1915-1934, 2009.
- [5] I. Zakharenkova, E. Astafyeva and I. Cherniak, "GPS and In-Situ Swarm Observations of the Equatorial Plasma Density Irregularities in the Top Side Ionosphere," *Earth, Planets and Space*, vol. 120, no. 68, 2016.
- [6] M. Nishioka, A. Saito and T. Tsugawa, "Occurrence Characteristics of Plasma Bubble Derived from Global-Based Receiver Networks," *Journal of Geophysical Research*, vol. 113, no. A5, 2008.
- [7] Y. Otsuka, "Review of the Generation Mechanisms of Post-Midnight Irregularities in the Equatorial and Low-Latitude Ionosphere," *Progress in Earth and Planetary Science*, 2018.
- [8] C. Ko and H. Yeh, "COSMIC/FORMOSAT-3 observations of equatorial F region irregularities in the SAA longitude sector," *Journal of Geophysical Research*, vol. 115, no. A11, 2010.
- [9] A. Sharma, D. Nade, S. Nikte, P. Patil, R. Chodpage, R. Vhatkar, M. Rokade and S. Gurubaran, "Occurrence of equatorial plasma bubbles over Kolhapur," *Advances in Space Research*, vol. 54, no. 3, pp. 435-442, 2014.
- [10] J. Aarons, "Equatorial Scintillation: A Review," *IEEE Transactions on Antennas and Propagation*, vol. 25, no. 5, pp. 729-736, 1977.
- [11] M. Kelly, J. Comberiate, E. Miller and L. Paxton, "Progress toward forecasting of space weather effects on UHF SATCOM after Operation Anaconda," *Space Weather*, vol. 12, no. 10, pp. 601-611, 2014.

- [12] L. Spogli, C. Cesaoni, D. Di Mauro, M. Pezzopane, L. Alfonsi, E. Musico, G. Povero, M. Pini, F. DAVIS, R. Romero, N. Linty, P. Abadi, F. Nuraeni, A. Husin, M. Le Huy, T. Thi Lan, T. Vinh La, V. Gil Pillat and N. Flourey, "Formation of Ionospheric Irregularities over Southeast Asia during the 2015 St. Patrick's Day Storm," *Journal of Geophysical Research*, vol. 121, no. 12, pp. 12211-12233, 2016.
- [13] J. Shi, G. Wang, Reinisch, S. Shang, X. Wang, G. Zherebotsov and A. Potekhin, "Relation between Strong Range Spread F and Ionospheric Scintillations Observed in Hainan from 2003 to 2007," *Journal of Geophysical Research*, vol. 116, no. A8, 2011.
- [14] M. C. Kelly, *The Earth's Ionosphere: plasma physics and electrodynamics*, vol. 96, International geophysics series, 2009.
- [15] M. Abdu, J. Souza, I. Batista and J. Sobral, "Empirical Spread F Statistics and Empirical Representation for IRI: A Regional Model for the Brazilian Longitude Sector," *Advances in Space Research*, vol. 31, no. 3, pp. 703-716, 2003.
- [16] I. Model, "International Reference Ionosphere," 2023. [Online]. Available: <http://irimodel.org/>. [Accessed 24 06 2022].
- [17] D. Farley, B. Balsey, R. Woodman and J. McClure, "Equatorial spread F: Implications of VHF radar observations," *Journal of Geophysical Research*, vol. 75, no. 34, pp. 7199-7216, 1970.
- [18] M. Abdu, J. Sobral and I. Batista, "Equatorial spread F statistics in the American longitudes: Some problems relevant to ESF description in the IRI scheme," *Advances in Space Research*, vol. 25, no. 1, pp. 113-124, 2000.
- [19] V. Sreeja, C. Vineeth, T. Pant, S. Ravidran and R. Sridharan, "Role of gravity wavelike seed perturbations on the triggering of ESF – a case study from unique dayglow observations," *Annales Geophysicae*, vol. 27, no. 1, pp. 313-318, 2009.
- [20] M. Abdu, E. Kherani, I. Batista and J. Sobral, "Equatorial evening prereversal vertical drift and spread F suppression by disturbance penetration electric fields," *Geophysical Research Letters*, vol. 36, no. 19, October 2009.
- [21] J. Uemoto, T. Maruyama, T. Saito, M. Ishii and R. Yoshimura, "Relationships between pre-sunset electrojet strength, pre-reversal enhancement and equatorial spread-F onset," *Annales Geophysicae*, vol. 28, no. 2, pp. 449-454, 2010.
- [22] T. Yokoyama, H. Jin and H. Shinagawa, "West wall structuring of equatorial plasma bubbles simulated by three-dimensional HIRB model," *Journal of Geophysical Research*, vol. 120, no. 10, pp. 8810-8816, 2015.

- [23] T. Yokoyama, "A review on the numerical simulation of equatorial plasma bubbles toward scintillation evolution and forecasting," *Progress in Earth and Planetary Science*, vol. 37, no. 4, 2017.
- [24] Kenro Nozaki, "FMCW Ionosonde for the SEALION Project," *Journal of the National Institute of Information and Communication Technology*, vol. 56, pp. 287-298, 2009.
- [25] N. Wakai, H. Ohya and T. Koizumi, Manual of Ionogram Scaling (Third version), Radio Research Laboratory, Ministry of Posts and Telecommunications, 1987.
- [26] W. Piggot and R. Rawer, "U.R.S.I handbook of ionogram interpretation and reduction," *World Data Center A for Solar-Terrestrial Physics*, 1978.
- [27] P. Abadi, Y. Otsuka and T. Tsugawa, "Effects of pre-reversal enhancement of E x B drift on the latitudinal extension of plasma bubble in Southeast Asia," *Earth, Planets and Space*, vol. 74, no. 67, pp. 1-7, 2015.
- [28] G. Manju, M. Madhav Haridas and R. Aswathy, "Role of gravity wave seed perturbation in ESF day-to-day variability: A quantitative approach," *Advances in Space Research*, vol. 57, no. 4, pp. 1021-1028, 2016.
- [29] C. Huang, "Effects of the postsunset vertical plasma drift on the generation of equatorial spread F," *Progress in Earth and Planetary Science*, vol. 5, no. 3, 2018.
- [30] O. Oladipo, J. Adeniyi, I. Adimula, A. Olawepo, A. Olowookere, F. Salifu, S. Radicella and B. Reinisch, "The role of the F-region vertical drift on the onset time of the equatorial spread-F over Ilorin, Nigeria," *J. Earth Syst. Sci.*, 2019.
- [31] M. Abdu, "Equatorial spread F development and quiet time variability under solar minimum conditions," *Indian Journal of Radio and Space Physics*, vol. 41, pp. 168-183, 2012.
- [32] M. Abdu, J. de Souza, E. Kherani, I. Batista, J. MacDougall and J. Sobral, "Wave structure and polarization electric field development in the bottomside F layer leading to postsunset equatorial spread F," *Journal of Geophysical Research*, vol. 120, no. 8, pp. 6930-6940, 2015.
- [33] R. Tsunoda and B. White, "On the generation and growth of equatorial backscatter plumes: 1. Wave structure in the bottomside F layer," *J. Geophys. Res.*, vol. A5, no. 86, pp. 3610-3616, 1981.
- [34] G. Manju, M. Madhav Haridas, G. Ramkumar, T. K. Pant, R. Sridharan and P. Sreelatha, "Gravity wave signatures in the dip equatorial ionosphere-thermosphere system during the annular solar eclipse of 15 January 2010," *J. Geophys. Res. Space Physics*, vol. 119, no. 6, p. 4929-4937, 2014.

This material is reserved for educational use only, not allowed for commercial use.

Forbidden to modify the content, and cite the document when use.

- [35] C. Torrence and G. Compo, "A Practical Guide to Wavelet Analysis," *Bulletin of the American Meteorological Society*, vol. 79, no. 1, pp. 61-78, 1998.
- [36] S. Meyers, B. Kelly and J. O'Brien, "An Introduction to Wavelet Analysis in Oceanography and Meteorology: With Application to the Dispersion of Yanai Waves," *Weather Review*, vol. 121, pp. 2858-2866, 1993.
- [37] S. Baliunas, P. Frick, D. Sokoloff and W. Soon, "Time scales and trends in the central England temperature data (1659-1990): A wavelet analysis," *Geophysical Research Letters*, vol. 24, no. 11, pp. 1351-1354, 1997.
- [38] I. Daubechies, "The wavelet transform, time-frequency localization and signal analysis," *IEEE Transactions on Information Theory*, vol. 36, no. 5, pp. 961-1005, 1990.
- [39] G. Kaiser, "A Friendly Guide to Wavelets," *Birkhäuser*, 1994.
- [40] M. Farge, "Wavelet transforms and their applications to turbulence," *Annu. Rev. Fluid Mech*, vol. 24, pp. 395-457, 1992.
- [41] M. Abdu, "Outstanding problems in the equatorial ionosphere-thermosphere electrodynamics relevant to spread F," *Journal of Atmospheric and Solar-Terrestrial Physics*, pp. 869-884, 2001.
- [42] S. Klinngam, P. Supnithi, S. Rungraengwajjake, T. Tsugawa, M. Ishii and T. Maruyama, "The Occurrence of Equatorial Spread-F at Conjugate Stations in Southeast Asia," *Advances in Space Research*, vol. 55, no. 8, pp. 2139-2147, 2015.
- [43] G. Wang, J. Shi, X. Wang, S. Shang, G. Zherebtsov and O. Pirog, "The statistical properties of spread F observed at Hainan station during the declining period of the 23rd solar cycle," *Annales Geophysicae*, vol. 28, no. 6, pp. 1263-1271, 2010.
- [44] T. Lan, C. Jiang, G. Yang, Y. Zhang, J. Liu and Z. Zhao, "Statistical analysis of low-latitude spread F observed over Puer, China, during 2015-2016," *Earth, Planets and Space*, vol. 138, no. 71, 2019.
- [45] A. Upadhayaya and S. Gupta, "A statistical analysis of occurrence characteristics of Spread-F irregularities over Indian region," *Journal of Atmospheric and Solar-Terrestrial Physics*, vol. 112, pp. 1-9, 2014.
- [46] S.-Y. Su, C. Chao, C. Liu and H. Ho, "Meridional wind effect on anti-solar activity correlation of equatorial density irregularity distribution," *Journal of Geophysical Research*, vol. 112, no. A10, 2007.
- [47] M. Palmroth, H. Laakso, B. Fejer and R. Pfaff, "DE 2 observations of morningside and eveningside plasma density depletions in the equatorial ionosphere," *Journal of Geophysical Research*, vol. 105, no. A8, pp. 18429-18442, 2000.

- [48] G. Li, B. Ning, L. Liu, W. Wan and J. Liu, "Effect of magnetic activity on plasma bubbles over equatorial and low-latitude regions in East Asia," *Annales Geophysicae*, vol. 27, no. 1, pp. 303-312, 2009.
- [49] F. Becker-Guedes, Y. Sahai, P. Fagundes, W. Lima, V. Pillat and J. Abalde, "Geomagnetic storm and equatorial spread-F," *Annales Geophysicae*, vol. 22, no. 9, pp. 3231-3239, 2004.
- [50] M. Abdu, J. Sobral, I. Batista, V. Rios and C. Medina, "Equatorial spread-F occurrence statistics in the American longitudes: Diurnal, seasonal and solar cycle variations," *Advances in Space Research*, vol. 22, no. 6, pp. 851-854, 1998.
- [51] M. Pezzopane, E. Zuccheretti, A. de Abreu, R. de Jesus, P. Fagundes, P. Supnithi, S. Rungraengwajiake, T. Nagatsuma, T. Tsugawa, M. Cabrera and R. Ezquer, "Low-latitude equinoctial spread-F occurrence at different longitude sectors under low solar activity," *Annales Geophysicae*, vol. 31, no. 2, pp. 153-162, 2013.
- [52] M. Pietrella, M. Pezzopane, P. Fagundes, R. de Jesus, P. Supnithi, S. Klinngam, R. Ezquer and M. Cabrera, "Equinoctial spread-F occurrence at low latitudes in different longitude sectors under moderate and high solar activity," *Journal of Atmospheric and Solar-Terrestrial Physics*, vol. 164, pp. 149-164, 2017.
- [53] T. Hoang, M. Abdu, J. MacDougall and I. Batista, "Longitudinal differences in the equatorial spread F characteristics between Vietnam and Brazil," *Advances in Space Research*, vol. 45, no. 3, pp. 351-360, 2010.
- [54] S. Rungraengwajiake, P. Supnithi, T. Tsugawa, T. Maruyama and T. Nagatsuma, "The Variation of Equatorial Spread-F Occurrences Observed by Ionosonde at Thailand Latitude Sector," *Advances in Space Research*, vol. 52, no. 10, pp. 1809-1819, 2013.
- [55] G. Li, B. Ning, Y. Otsuka, M. Abdu, P. Abadi, Z. Liu, L. Spogli and W. Wan, "Challenges to Equatorial Plasma Bubble and Ionospheric Scintillation Short-Term Forecasting and Future Aspects in East and Southeast Asia," *Surveys in Geophysics*, pp. 201-238, 2021.
- [56] Y. LeCun, Y. Bengio and G. Hinton, "Deep Learning," *Nature*, vol. 521, 2015.
- [57] D. Silver, A. Huang, C. Maddison, A. Guez, L. Sifre, G. van den Driessche, J. Schrittwieser, I. Antonoglou, V. Panneershelvam, M. Lanctot, S. Dieleman, D. Grewe, J. Nham, N. Kalchbrenner, I. Sutskever, T. Lillicrap, M. Leach, K. Kavukcuoglu and et. al., "Mastering the game of Go with deep neural networks and tree search," *Nature*, pp. 484-489, 2016.

- [58] A. Vaswani, N. Shazeer, N. Parmar, J. Uszkoreit, L. Jones, A. Gomez, L. Kaiser and I. Polosukhin, "Attention Is All You Need," *31st Conference on Neural Information Processing Systems*, 2014.
- [59] M. Lewis, Y. Liu, N. Goyal, M. Ghazvininejad, A. Mohamed, O. Levy, V. Stoyanov and L. Zettlemoyer, "BART: Denoising Sequence-to-Sequence Pre-training for Natural Language Generation, Translation, and Comprehension," *Machine Learning*, 2019.
- [60] W. Kornyanat, P. Supnithi, S. Lerkvaranyu, Tsugawa, T, T. Nagatsuma and T. Maruyama, "TEC prediction with neural network for equatorial latitude station in Thailand," *Earth, Planets and Space*, vol. 64, no. 6, pp. 473-483, 2012.
- [61] L. McKinnell and A. Poole, "The development of a neural network based short term foF2 forecast program," *Physics and Chemistry of the Earth, Part C: Solar, Terrestrial and Planetary Science*, vol. 25, no. 4, pp. 287-290, 2000.
- [62] J. Kim, Y. Kwak, Y. Kim, S. Moon, S. Jeong and J. Yun, "Regional Ionospheric Parameter Estimation by Assimilating the LSTM Trained Results Into the SAMI2 Model," *Space Weather*, vol. 18, no. 10, 2020.
- [63] Y. Tan, Q. Hu, Z. Wang and Q. Zhong, "Geomagnetic Index Kp Forecasting With LSTM," *Space Weather*, vol. 16, no. 4, 2018.
- [64] P. Thammavongsy, P. Supnithi, W. Phakphisut, W. Hozumi and T. Tsugawa, "Spread-F Prediction Model for the Equatorial Chumphon Station, Thailand," *Advances in Space Research*, vol. 65, no. 1, pp. 152-162, 2020.
- [65] L. McKinnell, M. Paradza, P. Cilliers, M. Abdu and J. de Souza, "Predicting the Probability of Occurrence of Spread-F over Brazilian using Neural Networks," *Advances in Space Research*, vol. 46, no. 8, pp. 1047-1054, 2010.
- [66] A. Collado-Villaverde, P. Munoz and C. Cid, "Deep Neural Networks With Convolutional and LSTM Layers for SYM-H and ASY-H Forecasting," *Space Weather*, vol. 19, no. 6, 2021.
- [67] E. Oyeyemi, L. McKinnell and A. Poole, "Neural network-based prediction techniques for global modeling of M(3000)F2 ionospheric parameter," *Advances in Space Research*, vol. 35, no. 9, pp. 643-650, 2007.
- [68] S. Watanabe, E. Sagawa, K. Ohtaka and H. Shimazu, "Prediction of the Dst index from solar wind parameters by a neural network method," *Earth, Planets and Space*, vol. 54, p. e1263-e1275, 2002.
- [69] S. Shidler and F. Rodrigues, "Modeling equatorial ionospheric vertical plasma drifts using machine learning," *Earth, Planets and Space*, vol. 102, no. 72, 2020.

- [70] A. Atabati, M. Alizadeh, H. Schuh and L. Tsai, "Ionospheric Scintillation Prediction on S4 and ROTI Parameters Using Artificial Neural Network and Genetic Algorithm," *Remote Sensing*, vol. 13, no. 11, 2021.
- [71] F. Emmert-Streib, Z. Yang, H. Feng, S. Tripathi and M. Dehmer, "An Introductory Review of Deep Learning for Prediction Models with Big Data," *Frontiers in Artificial Intelligence*, vol. 3, 2020.
- [72] S. Hochreiter and J. Schmidhuber, "Long Short-Term Memory," *Neural Computation*, pp. 1735-1780, 1997.
- [73] A. Graves, "Supervised Sequence Labelling with Recurrent Neural Networks," *Studies in Computational Intelligence*, vol. 385, pp. 38-45, 2012.
- [74] T. Fawcett, "An Introduction to ROC Analysis," *Pattern Recognition Letters*, vol. 27, no. 8, pp. 861-874, 2006.
- [75] M. Sokolova and G. Lapalme, "A systematic analysis of performance measures for classification tasks," *Information Processing and Management*, vol. 45, no. 4, pp. 427-437, 2009.
- [76] D. Anderson and R. Redmon, "Forecasting Scintillation Activity and Equatorial Spread F," *Space Weather*, vol. 15, pp. 495-502, 2017.
- [77] P. Abadi, U. Ahmad, Y. Otsuka, P. Jamjareegulgarn, D. Martiningrum, A. Faturahman, S. Perwitasari, R. Saputra and R. Septiawan, "Modeling Post-Sunset Equatorial Spread-F Occurrence as a Function of Evening Upward Plasma Drift Using Logistic Regression, Deduced from Ionosondes in Southeast Asia," *Remote Sensing*, vol. 14, no. 8, 2022.
- [78] P. Thammavongsy, P. Supnithi, L. Myint, K. Hozumi and D. Lakanchanh, "Equatorial spread-F forecasting model with local factors using the long short-term memory network," *Earth Planets Space*, vol. 118, no. 75, 2023.
- [79] W. McCulloch and W. Pitts, "A logical calculus of the ideas immanent in nervous activity," *The bulletin of mathematical biophysics*, pp. 115-133, 1943.
- [80] F. Rosenblatt, "The perceptron: A probabilistic model for information storage and organization in the brain," *Psychological Review*, vol. 65, no. 6, pp. 386-408, 1958.
- [81] O. D. Explorer, "OMNIWeb Goddard Space Flight Center," 2022. [Online]. Available: <https://omniweb.gsfc.nasa.gov/form/dx1.html>. [Accessed 04 June 2022].
- [82] W. Kyoto, "World Data Center for Geomagnetism, Kyoto," 2022. [Online]. Available: <https://wdc.kugi.kyoto-u.ac.jp/>. [Accessed 04 09 2022].
- [83] L. Wei, C. Jiang, Y. Hu, E. Aa, W. Huang, J. Liu, G. Yang and Z. Zhao, "Ionosonde Observations of Spread F and Spread Es at Low and Middle Latitudes during the

Recovery Phase of the 7–9 September 2017 Geomagnetic Storm," *Remote Sensors*, vol. 13, no. 5, 2021.

- [84] C. Huang and M. Hairston, "The postsunset vertical plasma drift and its effects on the generation of equatorial plasma bubbles observed by the C/NOFS satellite," *Journal of Geophysical Research*, vol. 120, no. 3, pp. 2263-2275, 2015.
- [85] R. Aswathy and G. Manju, "The post sunset equatorial F- region zonal drift variability and its linkage with equatorial spread F onset and duration over Indian longitudes," *Advances in Space Research*, vol. 67, no. 4, pp. 1254-1260, 2021.
- [86] K. Ajith, S. Ram, G. Li, ., M. Yamamoto, K. Hozumi, G. Yatini and P. Supnithi, "On the solar activity dependence of midnight equatorial plasma bubbles during June solstice periods," *Earth and Planetary Physics*, vol. 5, no. 5, pp. 378-386, 2021.
- [87] R. Singh and S. Sripathi, "A Statistical Study on the Local Time Dependence of Equatorial Spread F Irregularities and their Relation to Low Latitude Es layers under Geomagnetic Storms," *Journal of Geophysical Research*, vol. 125, no. 1, 2019.
- [88] E. Agyei-Yeboah, I. Paolino, A. Medeiros, R. Buriti, A. Paulino, P. Essien, S. Lomotey, H. Takahashi and C. Wrasse, "Seasonal variation of plasma bubbles during solar cycle 23–24 over the Brazilian equatorial region," *Advances in Space Research*, vol. 64, no. 7, pp. 1365-1374, 2019.
- [89] A. W. James, "Dependence of equatorial bubbles and bottomside spread F on season, magnetic activity, and  $E \times B$  drift velocity during solar maximum," *Journal of Geophysical Research*, vol. 107, no. A2, 2002.
- [90] C. Stolle, H. Luhr, M. Rother and G. Balasis, "Magnetic signatures of equatorial spread F as observed by the CHAMP satellite," *Journal of Geophysical Research*, vol. 111, no. A02304, 2006.
- [91] P. Amaechi, E. Oyeyemi, A. Akala and C. Amory-Mazaudier, "Geomagnetic activity control of irregularities occurrences over the crest of the African EIA," *Earth and Space Science*, 2020.
- [92] C. Huang and M. Hairston, "The postsunset vertical plasma drift and its effects on the generation of equatorial plasma bubbles observed by the N/NOFS satellite," *Journal of Geophysical Research: Space Physics*, pp. 2263-2275, 2015.
- [93] N. Balan, T. Maruyama, A. Patra and V. Narayanan, "A minimum in the latitude variation of spread-F at March equinox," *Progress in Earth and Planetary Science*, 2018.
- [94] M. Mahav Harida, G. Manju and T. Arunanmani, "Solar activity variations of Equatorial Spread-F occurrence and sustenance during different seasons over

- Indian longitudes: Empirical model and causative mechanisms," *Advances in Space Research*, vol. 61, no. 10, pp. 2585-2592, 2018.
- [95] E. Beshir, M. Nigussie and M. Moldwin, "Characteristics of equatorial nighttime spread F - An analysis on season-longitude, solar activity and triggering causes," *Advances in Space Research*, vol. 65, no. 1, pp. 95-106, 2020.
- [96] E. Mohino and M. Herraiz, "Application of wavelet analysis to quasi-2-day oscillation occurrence in the time variations of foF2," *International Journal of Geomagnetism and Aeronomy*, vol. 4, no. 3, pp. 215-220, 2003.
- [97] R. Thoppilan, D. De Freitas, J. Hall, N. Shazeer, A. Kulshreshtha, H. Cheng, A. Jin, T. Bos, L. Baker, Y. Du, Y. Li, H. Lee and et. al., "LaMDA: Language Models for Dialog Applications," *Artificial Intelligence*, 2022.
- [98] K. Nozaki, "FMCW Ionosonde for the SEALION Project," *Journal of the National Institute of Information and Communications Technology*, vol. 56, pp. 287-298, 2009.
- [99] P. Thammavongsy, P. Supnithi, L. Myint, K. Hozumi and D. Lakanchanh, "Comparison of observed equatorial spread-F statistics between two longitudinally separated magnetic equatorial stations and the IRI-2016 model during low and high solar activities," *Advances in Space Research*, vol. 69, no. 6, pp. 2501-2511, 2022.
- [100] M. Abdu, E. Kherani, I. Batista and J. Sobral, "Equatorial evening prereversal vertical drift and spread F suppression by disturbance penetration electric fields," *Geophysical Research Letters*, vol. 36, no. 19, October 2009.

## AUTHOR BIOGRAPHY

Name and surname	Mr. Phimmasone Thammavongsy
Date of birth	04 September 1991
Address	Yone village, Peak district, Xiengkhouang province, Lao P.D.R.
Education background	2013, Bachelor degree of Telecommunication Engineering, Faculty of Engineering, National University of Laos 2018, Master degree of Computing in Engineering Systems, International College, King Mongkut's Institute of Technology Ladkrabang
Professional skills	1) Machine learning 2) Equatorial ionospheric irregularity and its forecasting model 3) Time series forecasting model and designs 4) Big data and data mining
Working experiences and publications	
2020	P. Thammavongsy, P. Supnithi, W. Phakphisut, W. Hozumi and T. Tsugawa, "Spread-F Prediction Model for the Equatorial Chumphon Station, Thailand," <i>Advances in Space Research</i> , vol. 65, no. 1, pp. 152-162, 2020.
2022	P. Thammavongsy, P. Supnithi, L. Myint, K. Hozumi and D. Lakanchanh, "Comparison of observed equatorial spread-F statistics between two longitudinally separated magnetic equatorial stations and the IRI-2016 model during low and high solar activities," <i>Advances in Space Research</i> , vol. 69, no. 6, pp. 2501-2511, 2022.
2023	P. Thammavongsy, P. Supnithi, L. Myint, K. Hozumi and D. Lakanchanh, "Equatorial spread-F forecasting model with local factors using the long short-term memory network," <i>Earth Planets Space</i> , vol. 118, no. 75, 2023.